Effects of Advection on Non-Equilibrium Systems

Conrad Barrett-Freeman

Doctor of Philosophy
The University of Edinburgh
August 2011

Abstract

We study a number of non-equilibrium models of interest to both active matter and biological physicists. Using microscopic agent-based simulation as well as numerical integration of stochastic PDEs, we uncover the non-trivial behaviour exhibited when active transport, or an advection field, is added to out of equilibrium systems. When gravity is included in the celebrated Fisher-Kolmogoroff Petrovsky Piscounoff (F-KPP) equation, to model sedimentation of active bacteria in a container, we observe a discontinuous phase transition between a 'sedimentation' and a 'growth' phase, which should in principle be observable in real systems. With the addition of multiplicative noise, the resulting model contains, as its limits, both the bacterial sedimentation previously described and the fluctuating hydrodynamic description of Directed Percolation (DP), an important and well-studied non-equilibrium system whose physics incorporate many universal features which are typical of systems with absorbing states. We map out the phase diagram describing all the systems in between these two limiting cases, finding that adding an advection term, however small, immediately lifts the resulting system out of the DP universality class. Furthermore, we find two distinct low-density phases separated by a dynamical phase transition reminiscent of a spinodal transition. Finally, we attempt to improve the current diffusion-limited model for the growth of filopodia, which are intriguing networks of actin fibres used by moving cells to sense their environment. By the addition of directed transport of actin monomers to the fibre tip complex by myosin molecular motors, we show that, under appropriate conditions, the resulting dynamics may be more efficient that transport by diffusion alone, which would result in filopodial lengths better corresponding to experimental observation.

Declaration

I do hereby declare that this thesis was composed by myself and that the work described within is my own, except where explicitly stated otherwise.

C. Barrett-Freeman
August 9th 2011

Acknowledgements

Thanks to my supervisors Martin Evans and Davide Marenduzzo for continual support and patience. Thank you as well to my unofficial supervisor Julien Tailleur for teaching me the 'tricks of the trade' and working closely with me towards the second paper: much of the work in this thesis has benefited from your thoroughness and precision. Thank you Jen for your love and support, and to the Hung Ga, my alternative family, for keeping me strong in body and spirit: "*The fist art from the past makes a great impact*"!

Contents

Chapter 1

Introduction

Gravity is only the bark of wisdom's tree, but it preserves it.

Confucius

Statistical Physics is vital in the journey towards providing accurate models of real systems, or those with any degree of complexity. Its tools allow us to characterise systems with very large numbers of particles, which would be impossible to describe deterministically. This holds for a variety of systems, whether mechanical, thermodynamic or biological. Even so, it is usually systems in thermodynamic equilibrium that are described in this way, where many physical variables are essentially constant across the system, and the physics is pretty well understood. Unfortunately, these represent an idealisation very rarely seen in nature, if at all, and the goal of finding a complete description for non-equilibrium systems is very much of current interest. In this thesis, I add to this growing volume of work on the physics of various non-equilibrium models in the hope that it may take us a small step closer to this achievement.

In this thesis, I take several important models from various fields and probe their behaviour under the addition of an advection term, whose meaning and significance are introduced briefly in this chapter. The different systems in question are Fisher waves, where advection represents a gravitational pull, and the resulting system can be used to model the sedimentation of multiplying bacteria. This is followed b a study of Directed Percolation, a famous class of absorbing-state phase transitions that is central to studies of non-equilibrium phase transitions. Finally, we attempt to improve the current diffusion- limited model for filopodial protrusion by using advection to simulate the action of

chemical motors, which is a very current topic of interest. All three of these models are introduced below, as well as any other underlying ideas. This chapter will then conclude with a brief summary of the rest of the chapters.

Equilibrium Physics: Phase Transitions and Universality

Systems in thermodynamic equilibrium can be characterised via a free energy, which they tend to minimise. For example, the Canonical ensemble, which exists in thermal equilibrium with its surroundings, is in a state such that the Helmholtz free energy, given by $F = U - TS$ where U is the internal energy, T the temperature and S the entropy, is minimised. It is F and the ability to derive all of the thermodynamic macroscopic variables from it that has made equilibrium statistical mechanics so successful over the last century and a half. Furthermore, a full probability distribution can usually be written down, such as the Boltzmann distribution for canonical ensembles, from which all of the relevant variables can also be obtained. Unfortunately, hardly any real systems in nature are in thermodynamic equilibrium, mostly they are in a state that changes over time or able to be pushed into one by some local fluctuation. Systems that are out of equilibrium are much harder to describe and no complete theory akin to the Boltzmann distribution exists. There is no universal free energy that can be minimised, although some candidates have been proposed (see [Tailleur 08] for an example), and work on the many diverse systems that are relaxing towards equilibrium, or that are in a non-equilibrium steady state, is ongoing.

In this thesis, we will be interested in several systems that exhibit phase transitions. A phase transition occurs when a parameter, such as temperature, is varied slightly to go through a critical point. Past the critical point, the system changes dramatically into a new phase, characterised by different functional forms for the macroscopic variables. An important quantity in phase transitions is the ‘order parameter‘, which is usually zero in one phase and non-zero in the other. The order parameter is often a measure of order in the system, and is typically given by appropriate derivatives of a function of the relevant free energy. This leads to the terminology ‘first’ or ‘second’ order transition depending on which derivative diverges at the critical point, and these are linked to the ‘discontinuous’ and ‘continuous’ transitions discussed below. We use the latter terminology generally as it can also apply to non-equilibrium phase transitions,

where no free energy is available. The Ising model [Pelissetto 02] is the usual example given, where the order parameter is the net magnetization, representing the degree of alignment of spins in the system. If the system is disordered, the net magnetization will be zero; if, however, the spins are all aligned, forming the ordered state, the order parameter will be $\pm m$. This model is a very important system, as the ferromagnetic transition described above exhibits universal critical exponents that are shared by many diverse systems at criticality. With non-equilibrium systems, much work has been put into finding similar universality classes that could help to group together the numerous observed phase transitions but this has been met with limited success. Arguably the most successful, at least in the field of absorbing state phase transitions, is the Directed Percolation universality class [Henkel 08, Hinrichsen 00] introduced below.

In equilibrium, phase transitions are usually separated into continuous and discontinuous types, depending on how the order parameter behaves at criticality. As the critical point is approached from the phase which has the non-zero order parameter, the order parameter will either go to zero continuously, as in the ferromagnetic transition, or make a discontinuous 'jump' at the critical point (in the thermodynamic limit). In finite systems, the discontinuity in the order parameter does not appear however as it approaches the critical point, and we must then use finite-size scaling to identify the type of transition we are observing. Such methods which we will use will be introduced in Chapter 5. Another feature of discontinuous transitions is phase coexistence, these types of transitions are characterised by the existence at criticality of two local free energy minima corresponding to the phases on either side of the transition. A 'latent heat' is therefore necessary to move the system from one phase to the other, with a portion of the system inhabiting one of the free energy minima and the rest in the other, hence ice and water can both exist at the critical temperature (zero degrees Celsius).

Continuous phase transitions can be characterised by a set of critical exponents that describe how the system will behave near criticality. It is these dimensionless numbers that are universal to the class of transitions: a transition is said to belong to a particular universality class if it shares critical exponents even though the microscopic behaviour might be very different. The critical exponents typically describe power law behaviour of some physical quantity, expressed by its distance to the critical point, for example, the heat capacity

will be given by:

$$c \propto |T - T_c|^{-\alpha} \tag{1.1}$$

where T is the Temperature, with T_c the critical point. α is the exponent and is a property of the transition, such as $\alpha \sim 0.11$ for the Ising transition in three dimensions [Pelissetto 02]. Five other static exponents are commonly seen $(\beta, \gamma, \delta, \nu, \eta)$ as well as the dynamic exponent z, usually used to describe the behaviour of the relaxation time, τ. Measuring these numbers either analytically or experimentally is an important task, as they will pin down the details of the various universality classes. Conversely, measuring the exponents in a given transition can help to find its universality class and therefore predict the behaviour of many of its characteristics near criticality.

Absorbing States

Coming back to non-equilibrium systems, a particularly interesting group of phase transitions is absorbing-state phase transitions. Absorbing states are configurations that can be reached by the dynamics of the system but not escaped from. Systems involving discrete particles that can multiply, $A \to 2A$, and annihilate, $2A \to \emptyset$, often have a non-zero probability of reaching a state which is devoid of particles. As the creation of new particles depends on there being particles already in the system, the dynamics is now effectively 'stuck' and will no longer evolve with time. Such systems are in strong violation of detailed balance, an alternative condition for equilibrium, and are therefore considered to be far from equilibrium. It is not unusual for finite systems to reach such a state with probability 1, given an infinite time has elapsed, and the dynamics to the absorbing state can exhibit interesting behaviour. First passage processes are introduced briefly in Chapter 2 and more details can be found in [Redner 01]. Directed Percolation [Broadbent 57], often described as the Ising model of non-equilibrium phase transitions, inherits its name from a lattice model for percolation of water through a porous medium. The water can only percolate in one direction and each site is connected to two 'previous' sites by interstices that can be open to allow the water through, with probability p, or closed with probability $1 - p$. A 'seed' exists at a single site and at a given time later, the lattice can have many 'wet' sites, or none. The existence of this absorbing state depends on the value of the percolation probability and as p goes past a critical value, p_c, the phase transition observed will be an absorbing-

state phase transition. This system will be described in more detail in Chapter 4.

Advection

Directed motion, or advection, is a relevant issue in many non-equilibrium systems. A well-known example of this is the Asymmetric Simple Exclusion Process (ASEP) [Derrida 93] compared with the Symmetric Simple Exclusion Process (SSEP) [Derrida 07b]. Both of these comprise of a one-dimensional lattice of sites that can be occupied by one particle only (exclusion). The particles can 'hop' to the left, with probability γ, or to the right, with probability δ, and the SSEP is the case where $\gamma = \delta$ (symmetric), whereas the TASEP (Totally ASEP) occurs when $\delta = 1$ and $\gamma = 0$. Unlike most equilibrium models, these systems exhibit phase transitions in one dimension [Evans 00] and have very rich phase behaviour considering their apparent simplicity. In addition to this, the dynamical exponent in the SSEP with open boundaries is $z = 2$, indicating that the phase transition is in the Edwards-Wilkinson universality class [Edwards 82]; introducing an asymmetry by allowing $p \neq q$, effectively adding a directed transport term, changes the transition completely. Now the transition will have $z = 3/2$ and belong to the Kardar-Parisi-Zhang (KPZ) [Kardar 86] group of transitions [Derrida 97]. Whereas in equilibrium phenomena, an advection field might be trivially transformed away by, for example, a Galilean transformation, the addition of the one-dimensional flow generally changes the behaviour of non-equilibrium processes quite dramatically. In Chapter 3, we alter the celebrated Fisher-Kolmogoroff Petrovsky Piscounoff equation that models diffusing and multiplying particles [Murray 02]:

$$\frac{\partial \rho(\underline{x}, t)}{\partial t} = D\nabla^2 \rho(\underline{x}, t) + \alpha\rho(1 - \rho). \tag{1.2}$$

We find that the inclusion of an advection field ($v\nabla\rho$) yields an intriguing result, specifically the creation of a new non-equilibrium phase transition.

Biological Systems

Biological systems are almost always away from, and often far from equilibrium, as a cell in equilibrium would be a dead cell. This is reflected by recent growing interest among physicists in biological systems. For example, as we are beginning to be able to map out the individual proteins involved in minute

biological processes more accurately, it becomes an interesting physical problem to model and explain the collective behaviour of these diverse players in the various macroscopic effects. This represents a huge field of problems to be solved. Furthermore, many of the biological systems are self-propelled so-called 'active materials', far from equilibrium and thus exhibiting interesting physics. Bacteria are a good example and are very interesting for many reasons: as they exist in a low Reynolds number environment, they have no use for a streamlined shape and use ingenious methods to propel themselves, such as rotating flagella [Bray 01]. In the bulk, bacteria exhibit 'run and tumble' behaviour [Berg 83], resulting largely in diffusive motion, but still constitute an active material if growth and decay are also considered. We will discuss bacteria in more detail in Chapter 3, where we use both microscopic and coarse-grained descriptions to model active particles sedimenting in a container.

We also pursue another model which is of current interest to physicists and biologists alike: filopodial protrusion. A filopodium consists of a self-assembled network of actin filaments, that push out from animal cell bodies in order to probe the environment and aid cell motility. Filopodia are another example of active matter as they also exhibit growth and decay. After developing a detailed agent-based simulation to test the current mean-field theory, we attempt to improve the model by adding the effect of directed transport by myosin motors. We expect advection to have the potential to play havoc, as myosin motors may carry actin to the tip which would otherwise have to diffuse to get there. The results of this are presented in Chapter 6.

Chapter Summary

In Chapter 2, I discuss the background theory and simulation methods with the relevant technical details, after which the main body of the thesis is laid out in the following way. In Chapter 3, we will uncover a non-equilibrium phase transition induced by the addition of advection and boundary conditions to the Fisher equation, in order to model bacterial sedimentation. We will discuss the nature of the transition and some interesting finite size effects, where the two non-equilibrium steady states can co-exist. We then attempt to improve the model by adding an explicit noise term and we perceive that this new equation contains two interesting limits. The first, where the noise is taken to zero, recovers bacterial sedimentation, and the other, obtained by taking the

advection strength to zero, is Directed percolation. We describe the underlying theory in Chapter 4, and the results of our study in Chapter 5. We also discuss the implications of changing the form of the noise to a different type, and see how dramatically this changes the phase behaviour mapped out at the start of the chapter. Finally, we probe the role of myosin X motors in assisting the growth of filopodia. The current diffusion-limited model appears to predict steady state lengths that are too short. Diffusion and advection lead to massively different transport behaviour in a test tube, so we may legitimately ask, what about in a growing filopodium? This will be covered in Chapter 6.

Chapter 2

Tools

In this chapter, I introduce the analytic methods and basic simulation techniques used throughout this thesis. Non-equilibrium systems are often described using one of three formulations: master, Langevin or Fokker-Planck equations. The first is used for discrete space problems and the other two are relevant for continuous space models; all three are discussed below. As we use reaction-diffusion problems throughout this thesis, I use the example of a random walk with all of the results in this chapter, being the simplest microscopic model that leads to macroscopic diffusion. I first discuss briefly the master equation description as it serves well to explain the concept of detailed balance. I will then obtain the probability distribution of the one-dimensional random walk and show that the walker's path can be written in the Langevin form — equations of this type will be of most interest in Chapter 5. I will explain the Ito-Stratonovich dilemma and explain why the Ito interpretation of Langevin equations is used exclusively in this thesis. I introduce the Ito formula used to change variables in Ito-interpreted Langevin equations and then use it to provide a derivation of the Fokker-Planck equation starting from the Langevin equation. Finally, I use the Fokker-Planck formulation to introduce First Passage Time problems and show applications to systems with absorbing states.

In the second part of this chapter, I give a quick overview of simulation techniques involved in the simulation of diffusion problems both when considering an agent-based model and when integrating the associated partial differential equation directly. Methods that are more specific to the problem being considered will be introduced in their relevant chapters. I shall summarise the salient

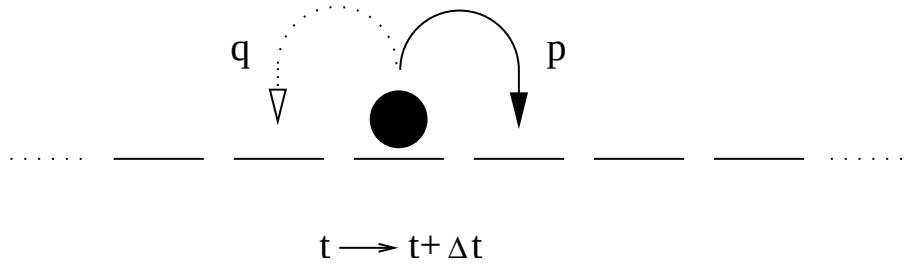

Figure 2.1: A one-dimensional random walker on a lattice. In time $t \to t + \Delta t$, the particle moves to the site immediately to its left or right with probability q and p respectively.

points and refer the reader to rigorous proofs in the literature; more thorough treatments of stochastic methods, the Fokker-Planck equation and first passage problems can be found in [Gardiner 83], [Risken 96] and [Redner 01] respectively.

2.1 Introduction: Random Walk

In most of this chapter we will be using the one-dimensional random walk as an example. This consists of a particle that is at a position x_0 on a one-dimensional line at time t_0. Every Δt, the particle 'hops' a distance Δx to the right with probability p, or to the left with probability q. An unbiased random walk is one where $p = q = \frac{1}{2}$. As we will see below, an unbiased random walker will not go anywhere on average and its mean-square displacement is proportional to the square-root of the time taken.

2.2 Introduction: Master Equation

Of the three descriptions commonly used for stochastic Markovian systems, the master equation is possibly the most general. In particular, for discrete state-space systems, a master equation can always be written down even if it cannot be solved explicitly. It is a set of first-order differential equations that give the rate of change of probabilities $P_i(t)$ for the system to be in a state i. It expresses conservation of probability, describing the time rate of change of $P_i(t)$ as the difference between the possible ways the system can enter this state and the ways that it can be exited:

$$\frac{\mathrm{d}P_i}{\mathrm{d}t} = \sum_{j \neq i} R(j \to i) P_j - \sum_{j \neq i} R(i \to j) P_i \tag{2.1}$$

where $R(i \to j)$ is the rate at which the system undergoes the transition $i \to j$. The first term is the gain term, representing the flow of probability into state i, and the second is the loss term, denoting the flow out of this state. Note that this is a continuous time master equation and that a discrete time version is also possible, in fact, we will begin with the discrete time case when discussing the random walk in section 2.2.2 below.

2.2.1 Detailed Balance

If a steady state of Eq. (2.1) above exists, it can be found by setting $\frac{\mathrm{d}P_i}{\mathrm{d}t} = 0$; i.e. we require the gain term to equal the loss term:

$$\sum_{j \neq i} R(j \to i) P_j = \sum_{j \neq i} R(i \to j) P_i. \tag{2.2}$$

The simplest way to satisfy this is to have the flow of probability out of each state equal the flow in, this is the *detailed balance* condition:

$$R(j \to i) P_j = R(i \to j) P_i \qquad \forall i, j. \tag{2.3}$$

This is a much stronger condition than the steady state condition in Eq. (2.2) and is one way of expressing that the system is in equilibrium. Another consequence of detailed balance is reversibility: if the condition holds there is no net probability current between states, therefore no apparent time direction and the system is reversible. Systems that exhibit a state i that is absorbing, a state which can be entered into, $R(j \to i) \neq 0$, but not escaped from, $R(i \to j) = 0 \ \forall j$, cannot possibly satisfy Eq. (2.3) and therefore reach a detailed balance condition; they are therefore considered to be strongly out of equilibrium.

2.2.2 Example: Master Equation for a random walk

Considering first the discrete time case, a random walk is a stochastic process whereby, as time increases by one time-step $t \to t + 1$, the particle could move to the left, move to the right, or do nothing at all. This is characterised by the following master equation for the probability $P_{t+1}(x|x_0)$ that the walker is at

position x at time $t+1$ having started in position x_0 at time t_0:

$$P_{t+1}(x|x_0) = qP_t(x+\Delta x|x_0) + pP_t(x-\Delta x|x_0) + (1-p-q)P_t(x|x_0). \quad (2.4)$$

If we define a unit of time $\mathrm{d}t$, such that $p = \lambda_R \mathrm{d}t$ and $q = \lambda_L \mathrm{d}t$ and $\lambda_{(L,R)}$ are hopping rates between the states, we obtain:

$$\begin{aligned} P_{t+\mathrm{d}t}(x|x_0) &= \lambda_L \mathrm{d}t P_t(x+\Delta x|x_0) \\ &+ \lambda_R \mathrm{d}t P_t(x-\Delta x|x_0) \\ &+ (1/\mathrm{d}t - \lambda_R - \lambda_L)\mathrm{d}t P_t(x|x_0) \end{aligned} \quad (2.5)$$

and therefore taking the continuous time limit $\mathrm{d}t \to 0$:

$$\frac{\mathrm{d}P_t}{\mathrm{d}t}(x|x_0) = \lim_{\mathrm{d}t\to 0} \frac{P_{t+\mathrm{d}t}(x|x_0) - P_t(x|x_0)}{\mathrm{d}t} \quad (2.6)$$

$$= \lambda_L P_t(x+\Delta x|x_0) + \lambda_R P_t(x-\Delta x|x_0) - (\lambda_R+\lambda_L)P_t(x|x_0). \quad (2.7)$$

This equation, unlike many master equations, is actually straightforward to solve by a simple Fourier transform method.

2.3 Analytic Methods

Having discussed the general ideas above, we now turn to the methods and equations I intend to use in this work. We begin with a more detailed look at the one-dimensional random walk.

2.3.1 Random Walk

We now solve for the probability distribution of the one-dimensional random walk. We start with the master equation given in Eq. (2.4) and expand to first order in time and to second order in space, obtaining upon rearranging:

$$\frac{\partial P_t(x)}{\partial t} = -(p-q)\frac{\Delta x}{\Delta t}\frac{\partial P_t(x)}{\partial x} + \left(\frac{p+q}{2}\right)\frac{\Delta x^2}{\Delta t}\frac{\partial^2 P_t(x)}{\partial x^2}. \quad (2.8)$$

If we consider first $p = q = \frac{1}{2}$, and define the diffusion constant, D:

$$D = \lim_{\substack{\Delta x\to 0 \\ \Delta t\to 0}} \frac{\Delta x^2}{2\Delta t} \neq 0 \quad (2.9)$$

where the limits are taken simultaneously such that D is finite and non-zero. We recover normal Fickian diffusion:

$$\frac{\partial P(x,t)}{\partial t} = D\frac{\partial^2 P}{\partial x^2} \tag{2.10}$$

i.e. a particle undergoing a random walk is equivalent to diffusion on a line: if we start with the particle at the origin, the probability of finding it at position x at time t diffuses out from the origin. Note that if a weak bias is retained, $p \neq q$ such that $p - q \approx \Delta x$, we have an advection term that will result in a 'drift' of particles in the direction of the bias. The diffusion equation above is straightforward to solve via Fourier transform: transforming Eq. (2.10) gives the ordinary differential equation $\partial_t \tilde{\rho} = -k^2 D\tilde{\rho}(k,t)$. This solves to give $\tilde{\rho}(k,t) = A\exp(-k^2 Dt)$, where A is a constant of integration to be found. Inverting the Fourier transform gives the result below: a Gaussian probability distribution for the unbiased random walk, $A = 1$ is fixed via the initial condition that the walker starts at the origin ($P(x,0) = \delta(x)$):

$$P(x,t) = \sqrt{\frac{1}{4\pi Dt}}e^{-x^2/(4Dt)}. \tag{2.11}$$

The distribution is centred at the origin and has variance $2Dt$, hence confirming the statement in 2.1 that the mean-square displacement of the random walker scales with $\sqrt{t}$ and that the mean displacement is zero.

2.3.2 The Langevin Equation

If we wish to model the path the above random walker takes $x(t)$, we can do this using the following stochastic equation:

$$\mathrm{d}x(t) = \sqrt{2D}\eta(t)\mathrm{d}t \tag{2.12}$$

where $\eta(t)$ is chosen to be a Gaussian random variable with mean 0 and variance $1/\mathrm{d}t$ so that $x(t)$ will have the same mean and variance as above. This stochastic differential equation is an example of a Langevin equation. More generally, this equation can be written as:

$$\mathrm{d}x = f(x,t)\mathrm{d}t + g(x,t)\mathrm{d}W(t) \tag{2.13}$$

with

$$\mathrm{d}W(t)/\mathrm{d}t = \eta(t). \tag{2.14}$$

Note that $\eta(t) \sim 1/\sqrt{\mathrm{d}t}$ and thus:

$$\mathrm{d}W(t) \sim \sqrt{\mathrm{d}t}. \tag{2.15}$$

Formally, this can always be solved:

$$x(t) - x(0) = \int_0^t f(x(t'), t')\mathrm{d}t' + \int_0^t g(x(t'), t')\mathrm{d}W(t'). \tag{2.16}$$

Note that if $f = 0$ and $g = \sqrt{2D}$ as in Eq. (2.12) then we obtain:

$$x(t) - x(0) = \sqrt{2D}W(t) \tag{2.17}$$

where $W(t)$ is a random walk, known as a *Wiener process*. Note also that the 2$^{\text{nd}}$ integral in Eq. (2.16) has some peculiar properties, leading to the Ito-Stratonovich dilemma discussed below.

2.3.3 The Ito-Stratonovich dilemma

Consider breaking up the integral over the random variable $\mathrm{d}W$ in Eq. (2.16) into a succession of time-steps $0 = t_0 < t_1 < ... < t_{N-1} < t_N = T$:

$$\int_0^T g(x(t))\mathrm{d}W(t) \equiv \lim_{N\to\infty} \sum_{i=0}^{N-1} g(x(\tau_i))(W(t_{i+1}) - W(t_i)) \tag{2.18}$$

where we have written $g = g(\tau_i)$ to illustrate the ambiguity in the time at which g is evaluated in each term of the sum. If we define:

$$\tau_i \equiv (1-\alpha)t_i + \alpha t_{i+1} \qquad\qquad 0 \leq \alpha \leq 1 \tag{2.19}$$

then α tunes the proportion of $g(t)$ that is evaluated at the beginning of the time step, t_i, and at the end, t_{i+1}. In particular, we will consider two common conventions: $\alpha = 0$ gives a Ito form of the Langevin equation, considering the value of g at the beginning of the step only, and $\alpha = \frac{1}{2}$ gives the Stratonovich form, considering an equal mixture of the beginning and the end. If $\mathrm{d}W$ is a differential from a standard Riemann integral, the value of α is irrelevant in

evaluating the sum: if we define Eq. (2.18) as $I[\alpha]$ and consider:

$$I[0] - I[1] = \lim_{N\to\infty} \sum_{i=0}^{N-1} \left[g(x(t_i)) - g(x(t_{i+1}))\right] \left(W(t_{i+1}) - W(t_i)\right) \tag{2.20}$$

$$\simeq \lim_{N\to\infty} \sum_{i=0}^{N-1} -g'(x(t_i)) \left[x(t_{i+1}) - x(t_i)\right] \left(W(t_{i+1}) - W(t_i)\right) \tag{2.21}$$

$$= \lim_{N\to\infty} \sum_{i=0}^{N-1} -g'(x(t_i))g(x(\tau_i)) \left(W(t_{i+1}) - W(t_i)\right)^2 \tag{2.22}$$

where, in order to obtain Eq. (2.21), we Taylor-expanded $g(x(t_{i+1}))$ and the dash denotes differentiation. To find Eq. (2.22), we used the definition of the Langevin process Eq. (2.13) after time-discretisation and neglecting the force term (i.e. $x(t_{i+1}) - x(t_i) = g(x(\tau_i))(W_{i+1} - W_i)$. Now, if $W(t)$ is a normal differentiable function, then:

$$W(t_{i+1}) - W(t_i) \simeq W' \mathrm{d}t \sim \mathcal{O}(\mathrm{d}t). \tag{2.23}$$

We see that $I[0] - I[1] \sim \mathrm{d}t$ (as $N \sim \frac{1}{\mathrm{d}t}$), which therefore tends to zero as $\mathrm{d}t \to 0$. If, on the other hand, $\mathrm{d}W(t)$ is a Wiener process, we know from Eq. (2.15) that it is of order $\sqrt{\mathrm{d}t}$ and hence $I[0] - I[1] \to 1$: the difference matters. Indeed, consider the average of a Wiener process:

$$\left\langle \int_0^T W(t)\mathrm{d}W(t) \right\rangle = \left\langle \sum_i W(t_i)(W(t_{i+1}) - W(t_i)) + \alpha(W(t_{i+1}) - W(t_i))^2 \right\rangle \tag{2.24}$$

$$= 0 + \alpha T \tag{2.25}$$

where we have written $W(\tau_i) = W(t_i) + \alpha(W(t_{i+1}) - W(t_i))$ as the random walk is only resolved at t_i and t_{i+1}, and hence the most reasonable way to define it at τ_i is to use a straight line approximation between these two points. The first term gives zero as the step length is not correlated with the last drawn random number, the second term gives αT because $\langle(\mathrm{d}W(t))^2\rangle = \mathrm{d}t$. The explicit dependence of the result on α means that the average indeed changes based on at which point in time we choose to evaluate our function. The Ito prescription gives zero and means that the function is independent of the following increment

of the random walk, it implies that $\langle W(t)\mathrm{d}W(t)\rangle = 0$. Stratonovich implies however that $W(t)\mathrm{d}W(t) = \mathrm{d}(W^2(t))/2$. Finally, if we look in more detail at the integral in the average above, we find

$$\begin{aligned}\int_0^T W(t)\mathrm{d}W(t) &= \sum_i W(\tau_i)(W(t_{i+1}) - W(t_i)) \\ &= \sum_i \left[W(t_i) + \alpha(W(t_{i+1}) - W(t_i))\right](W(t_{i+1}) - W(t_i)) \\ &= \sum_i \alpha W^2(t_{i+1}) - (1-\alpha)W^2(t_i) + (1-2\alpha)W(t_{i+1})W(t_i).\end{aligned} \tag{2.26}$$

We see here that using the Stratonovich prescription, we obtain:

$$\int_0^T W(t)\mathrm{d}W(t) = \sum_i \frac{1}{2}W^2(t_{i+1}) - \frac{1}{2}W^2(t_i) = \frac{1}{2}W^2(T) - \frac{1}{2}W^2(0) \tag{2.27}$$

i.e. the normal rules of calculus apply. In the second step, we have cancelled all of the terms in the sum with each successive term leaving only the end points. If, however, the Ito prescription is used, the integral gives a very different result from what would usually be expected, namely:

$$\int_0^T W(t)\mathrm{d}W(t) = \sum_i W(t_{i+1})W(t_i) - W^2(t_i). \tag{2.28}$$

Although this means that in some cases, especially when performing analytic calculations, it might be simpler to use Stratonovich, in this thesis we will solely be considering Langevin equations of the Ito form. This is because we are frequently interested in systems exhibiting an absorbing state. Consider for example zero-dimensional (i.e. single site) Directed Percolation[1] (DP), this system admits a continuous phase transition into an absorbing state and can be described by the following Langevin equation:

$$\frac{\partial\rho(t)}{\partial t} = \alpha\rho(1-\rho) + \Gamma_0\sqrt{\rho}\eta(t). \tag{2.29}$$

[1]Directed Percolation is introduced in more detail in Chapter 4

In [Gardiner 83], the author derives the connection between Ito and Stratonovich interpreted stochastic differential equations. In particular, it can be shown that a Stratonovich equation of the form Eq. (2.13) is equivalent to an Ito Langevin equation:

$$\mathrm{d}x = \left(f(x,t) + \frac{1}{2} g(x,t) \frac{\partial g}{\partial x} \right) \mathrm{d}t + g(x,t) \mathrm{d}W(t). \tag{2.30}$$

Returning to DP above, this means that if we interpreted Eq. (2.29) in the Stratonovich sense, this would be equivalent to the Ito Langevin equation:

$$\frac{\partial \rho(t)}{\partial t} = \alpha \rho (1-\rho) + \frac{\mathbf{\Gamma_0}}{\mathbf{4}} + \Gamma_0 \sqrt{\rho} \eta(t). \tag{2.31}$$

The extra term will produce a constant source and $\rho = 0$ will no longer be absorbing, hence we will always interpret Eq. (2.29) and all other Langevin equations using the Ito prescription.

2.3.4 Ito Formula

We must be careful when changing variables in a stochastic differential equation interpreted in the Ito sense. For this we use the 1-dimensional Ito Formula [Oksendal 98]. We define an Ito process as a stochastic process obeying the Langevin Equation 2.13, where $\mathrm{d}W(t)$ obeys the rules of the Ito stochastic calculus:

$$(\mathrm{dW(t)})^2 = \mathrm{dt} \tag{2.32}$$

and we disregard terms of higher order in $\mathrm{d}t$. If we want to change variables $x(t) \rightarrow y(t)$, and we have a twice-differentiable function $h(x(t),t)$ such that $y(t) = h(x(t),t)$, then we can use a Taylor expansion to find $\mathrm{d}y(t)$:

$$\mathrm{dy(t)} = \frac{\partial \mathrm{h}}{\partial \mathrm{t}} \mathrm{dt} + \frac{\partial \mathrm{h}}{\partial \mathrm{x}} \mathrm{dx(t)} + \frac{1}{2} \frac{\partial^2 \mathrm{h}}{\partial \mathrm{x}^2} (\mathrm{dx(t)})^2 \tag{2.33}$$

where $(\mathrm{d}x(t))^2 = \mathrm{d}x(t).\mathrm{d}x(t)$ is evaluated using Eq. (2.32). The proof of the above can be found in [Gardiner 83] and [Oksendal 98]. If we substitute Eq. (2.13) into Eq. (2.33), we can cast the Ito formula into a more useful form:

$$\mathrm{dy(t)} = \left(\frac{\partial \mathrm{h}}{\partial \mathrm{t}} + \mathrm{f(x,t)} \frac{\partial \mathrm{h}}{\partial \mathrm{x}} + \frac{\mathrm{g(x,t)}^2}{2} \frac{\partial^2 \mathrm{h}}{\partial \mathrm{x}^2} \right) \mathrm{dt} + \mathrm{g(x,t)} \frac{\partial \mathrm{h}}{\partial \mathrm{x}} \mathrm{dW_t}. \tag{2.34}$$

This form also shows immediately that $y(t)$ is itself also an Ito process, as it is in the form Eq. (2.13).

Example: Random Walk with Multiplicative Noise

Consider the following Ito process

$$\mathrm{d}x = \mu x \mathrm{d}t + \nu x \mathrm{d}W(t). \tag{2.35}$$

This example is sometimes used in the context of quantitative finance, where x is the price of a stock, μ is the coefficient of drift and ν is the price volatility. We can recast this into a Langevin equation with additive noise by setting $y = \ln x$, this gives:

$$\mathrm{d}y = (\mu - \nu^2/2)\mathrm{d}t + \nu \mathrm{d}W(t) \tag{2.36}$$

i.e. the stock price, x, is log-normally distributed with expectation $x_0 \mathrm{e}^{\mu t}$ and variance $x_0 \mathrm{e}^{2\mu t}(\mathrm{e}^{\nu^2 t} - 1)$.

2.3.5 From Langevin to Fokker-Planck Equations

We now show that a Fokker-Planck Equation can be derived directly from a Langevin equation, thus highlighting the equivalence of these two descriptions. We begin by considering the following Langevin Equation:

$$\frac{\mathrm{d}x(t)}{\mathrm{d}t} = f(x(t), t) + g(x(t), t)\eta(t) \tag{2.37}$$

where $\eta(t)$ is, as usual, Gaussian white noise with unit variance:

$$\langle \eta(t) \rangle = 0, \tag{2.38}$$

$$\langle \eta(t)\eta(t') \rangle = \delta(t - t'). \tag{2.39}$$

Taking a generic function $\phi(x(t))$, we seek to compute its time-derivative, and use Ito's formula above Eq. (2.34):

$$\frac{\mathrm{d}\phi(x(t))}{\mathrm{d}t} = f[x(t)]\partial_x \phi + \frac{1}{2} g^2[x(t)]\partial_x^2 \phi + g[x(t)](\partial_x \phi)\eta(t) \tag{2.40}$$

where ∂_x indicates partial differentiation with respect to x. We take the average of the above over all realisations of the noise. As we are using the Ito prescription, the last term can be factorised because $g[x(t)]\partial_x \phi$ will depend only on the

value of η at time t. Hence the last term drops out because $\langle \eta(t) \rangle = 0$ and we are left with:

$$\langle \frac{\mathrm{d}\phi(x(t))}{\mathrm{d}t} \rangle = \langle f[x(t)]\partial_x \phi + \frac{1}{2} g^2[x(t)]\partial_x^2 \phi \rangle. \tag{2.41}$$

We introduce a probability distribution, $P(x, t|x_0, t_0)$, that the system is in state x at time t conditioned on its being in state x_0 at time t_0, and define the average of any function $F(x(t))$ over realisations of the noise to be:

$$\langle F(x(t)) \rangle = \int \mathrm{d}z P(z, t) F(z). \tag{2.42}$$

Using this definition and Eq. (2.41), we obtain:

$$\left\langle \frac{\mathrm{d}\phi(x(t))}{\mathrm{d}t} \right\rangle = \int \mathrm{d}z \phi(z) \frac{\partial}{\partial t} P(z, t|x_0, t_0) \tag{2.43}$$

$$= \int \mathrm{d}z \left(f(z, t)\partial_z \phi + \frac{1}{2} g^2(z, t)\partial_z^2 \phi \right) P(z, t|x_0, t_0). \tag{2.44}$$

We integrate by parts discarding the surface terms ($P(x, t|x_0, t_0)$ must vanish at the boundaries):

$$\int \mathrm{d}z \phi(z) \frac{\partial}{\partial t} P(z, t|x_0, t_0) = \int \mathrm{d}z \phi(z) \left(-\frac{\partial f(z, t)P}{\partial z} + \frac{1}{2} \frac{\partial^2 g^2(z, t)P}{\partial z^2} \right). \tag{2.45}$$

As ϕ is arbitrary, we can equate the integrands, or equivalently by setting $\phi(z) = \delta(z - x)$ and evaluating, we obtain:

$$\frac{\partial}{\partial t} P(x, t) = -\frac{\partial}{\partial x}[f(x)P(x, t)] + \frac{\partial^2}{\partial x^2} \left[\frac{g^2(x)P(x, t)}{2} \right]. \tag{2.46}$$

Example: Random Walk and Diffusion

If we consider again the random walk given by Eq. (2.12), we have $f = 0$ and $g = \sqrt{2D}$. Using Eq. (2.46) above, this gives

$$\frac{\partial P(x, t)}{\partial t} = D \frac{\partial^2 P}{\partial x^2} \tag{2.47}$$

which shows once again the equivalence of the random walk and diffusion. It also alerts us to the fact that the Fokker-Planck equation is none other than the continuous version of a lattice master equation as we derived one from the

other in section 2.3.1.

2.3.6 First-Passage Time

From the Fokker-Planck equation, it is common to calculate steady-state probability distributions, i.e. by setting $\frac{\partial P}{\partial t} = 0$. However, in the context of absorbing-state phase transitions, the steady-state distribution will almost always be zero everywhere in the long time limit and time-dependent solutions become more relevant to study. An important question is "*How long does the system survive before being absorbed?*" and this is a good example of a first-passage problem. In order to answer this we need to think about the mean first-passage time of a stochastic process. This is the average time taken by the system to reach a given value *for the first time*. In the context of absorbing-state transitions, the mean first-passage time to the absorbing boundary can be interpreted as the mean survival time of the system.

We begin by deriving the Backward Fokker-Planck equation (BFPE), unlike the forward equation (FFPE) derived above, Eq. (2.46), this gives the evolution of the probability with respect to the initial time, t_0, as a function of derivatives with respect to the initial position, x_0. We consider the probability distribution $P(x, t|x_0, t_0)$ for an Ito stochastic process and decompose it into a combined probability including an intermediate step, $t' = t_0 + \mathrm{d}t$:

$$P(x, t|x_0, t_0) = \int P(x, t|x', t_0 + \mathrm{d}t)P(x', t_0 + \mathrm{d}t|x_0, t_0)\mathrm{d}x'. \tag{2.48}$$

We re-write the second probability:

$$P(x', t_0 + \mathrm{d}t|x_0, t_0) = \int \delta(y - x')P(y, t_0 + \mathrm{d}t|x_0, t_0)\mathrm{d}y \tag{2.49}$$

and use the following formal expansion of the delta-function (where the derivatives of the delta-function are also defined under an integral):

$$\delta(y - x') = \delta(x_0 - x' + y - x_0) \tag{2.50}$$

$$= \sum_{n=0}^{\infty} \frac{(y - x_0)^n}{n!} \left(\frac{\partial}{\partial x_0}\right)^n \delta(x_0 - x'). \tag{2.51}$$

Substituting this expansion into Eq. (2.49), and evaluating the integral over y,

gives:

$$P(x', t_0 + \mathrm{d}t|x_0, t_0) = \delta(x_0 - x') + \langle \mathrm{d}x_0 \rangle \frac{\partial}{\partial x_0}\delta(x_0 - x') \tag{2.52}$$

$$+ \frac{\langle (\mathrm{d}x_0)^2 \rangle}{2}\frac{\partial^2}{\partial x_0^2}\delta(x_0 - x') + \mathcal{O}((\mathrm{d}x_0)^3) \tag{2.53}$$

and then substituting this back into Eq. (2.48), and this time integrating over x', we find:

$$P(x, t|x_0.t_0) - P(x, t|x_0, t_0 + \mathrm{d}t) = \langle \mathrm{d}x_0 \rangle \frac{\partial}{\partial x_0}P(x, t|x_0, t_0 + \mathrm{d}t) \tag{2.54}$$

$$+ \frac{\langle (\mathrm{d}x_0)^2 \rangle}{2}\frac{\partial^2}{\partial x_0^2}P(x, t|x_0, t_0 + \mathrm{d}t). \tag{2.55}$$

Finally, using the Langevin equation Eq. (2.13), and evaluating the averages $\langle \mathrm{d}x_0 \rangle = f(x_0)\mathrm{d}t$ and $\frac{\langle (\mathrm{d}x_0)^2 \rangle}{2} = \frac{g^2(x_0)}{2}\mathrm{d}t$, and upon inserting these, re-arranging, and taking the $\mathrm{d}t \to 0$ limit, we obtain the BFPE:

$$\frac{\partial}{\partial t_0}P(x, t|x_0, t_0) = -f(x_0)\frac{\partial}{\partial x_0}P(x, t|x_0, t_0) - \frac{g^2(x_0)}{2}\frac{\partial^2}{\partial x_0^2}P(x, t|x_0, t_0). \tag{2.56}$$

A more useful equation for our purposes will give the forward time-evolution of the probability distribution with respect to the initial position. We assume that $P(x, t|x_0, t_0) = P(x, x_0, t - t_0)$ and can therefore write $\frac{\partial}{\partial t} = -\frac{\partial}{\partial t_0}$. Using this, Eq. (2.56) becomes:

$$\frac{\partial}{\partial t}P(x, t|x_0, t_0) = f(x_0)\frac{\partial}{\partial x_0}P(x, t|x_0, t_0) + \frac{g^2(x_0)}{2}\frac{\partial^2}{\partial x_0^2}P(x, t|x_0, t_0). \tag{2.57}$$

If there is a region Σ within which particles survive, the survival probability at any time t will be given by $S(x_0, t) = \int_\Sigma P(x, t|x_0)\mathrm{d}x$ and $Q(x_0, t) = -\frac{\partial}{\partial t}S(x_o, t)$ will be the probability that particles reach the absorbing boundary, i.e. the probability distribution of the first passage time, $T(x)$. In the case of one particle, this is the extinction probability. It is trivial to show that if $P(x, t|x_0)$ obeys the FFPE then $Q(x_0, t)$ will do so as well.

The m$^{\text{th}}$ moment of $Q(x, t)$ is defined as:

$$T_m = \int_0^\infty t^m Q(x, t)\mathrm{d}t. \tag{2.58}$$

We will be interested in the mean time to extinction, $\tau = T_1$, which is therefore found by setting $m = 1$ in the above equation. If we have not got a solution for the probability distribution but the Forwards Fokker-Planck Equation is known, we can use Eq. (2.57) to write down the equivalent Backward Fokker-Planck Equation. We can then substitute Eq. (2.58) into the BFPE to generate a recurrence relation for the moments T_m [Arecchi 82]. For the case where $m = 1$, this is straightforward to solve and we will pursue this in more detail in Chapter 5.

Example: Random Walk with an Absorbing Boundary

As a final application of the random walk example, we illustrate the above ideas by considering an unbiased random walk with an absorbing boundary at point $x_a > 0$.

If $P(x,t)$ is known then we can, in principle, calculate $Q(x,t)$. Although we could follow the method above, in this case more information can be gained using a simpler method from [Bazant 05]. We define $q(x,t)$ as the probability distribution that the random walker reaches point x for the first time at time t having started at the origin[2]. Clearly:

$$\int_{-\infty}^{t} q(x,t')\mathrm{d}t' = \mathrm{Prob}(T(x) < t). \tag{2.59}$$

The probability of going from $0 \to x$ at time t is the number of ways of reaching x at $t' < t$ and then returning after $t - t'$:

$$p(x,t) = \int_{0}^{t} q(x,t')p(0,t-t')\mathrm{d}t' \tag{2.60}$$

which is just the convolution of $q(x,t)$ and $p(0,t)$. If we therefore take the Laplace transform of the above equation ($L[q(t)] = \tilde{q}(s) = \int_0^\infty e^{-st}q(t)\mathrm{d}t$), we can solve for $\tilde{q}(x,s)$:

$$\tilde{q}(x,s) = \frac{\tilde{p}(x,s)}{\tilde{p}(0,s)} \tag{2.61}$$

[2]Note this is simply $Q(0,t)$ where the integral over $p(x,t)$ is evaluated in the interval $[-\infty, x]$

which can be inverted to give:

$$q(x,t) = \frac{1}{2\pi i}\int_{c-i\infty}^{c+i\infty} e^{st}\frac{\tilde{p}(x,s)}{\tilde{p}(0,s)}\mathrm{ds} \tag{2.62}$$

where c is taken so that the contour is to the right of any singularities. If we are only interested in the moments of $q(x,t)$, we will not need to invert the Laplace transform as they can easily be obtained from $\tilde{q}(x,s)$:

$$(-1)^n\frac{\partial^n\tilde{q}}{\partial s^n}\bigg|_{s=0} = \int_0^\infty t^n q(x,t)\mathrm{d}t = \langle T_n\rangle \tag{2.63}$$

Returning now to the random walk in one dimension, we give the $p(x,t)$ as the inverse Fourier transform of the Fourier transform of Eq. (2.11):

$$p(x,t) = \frac{1}{2\pi}\int_{-\infty}^{\infty} e^{ikx}\hat{p}(k,t)\mathrm{dk} \tag{2.64}$$

where $\hat{p}(k,t) = e^{-k^2Dt}$. We now calculate the Laplace transform:

$$\begin{aligned}\tilde{p}(x,s) &= \frac{1}{2\pi}\int_{-\infty}^{\infty} e^{ikx}\left[\int_0^\infty e^{-st}e^{-k^2Dt}\mathrm{d}t\right]\mathrm{dk}\\ &= \frac{1}{2\pi}\int_{-\infty}^{\infty}\frac{e^{ikx}}{s+k^2D}\mathrm{dk}\\ &= \frac{1}{2\sqrt{sD}}e^{-|x|\sqrt{s/D}}.\end{aligned} \tag{2.65}$$

The $|x|$ after the complex integration comes from the fact the integrand has poles at $k = \pm i\sqrt{s/D}$: if x is positive, the contour is closed using a semi-circle in the upper half plane, enclosing the positive pole. If x is negative, the lower half plane is used encircling the negative pole. Inserting the result into Eq. (2.61) we obtain:

$$\tilde{q}(x,s) = e^{-|x|\sqrt{s/D}}. \tag{2.66}$$

If we consider the probability that the walker will reach the absorbing state at x over all time:

$$\tilde{q}(x,0) = \int_0^\infty q(x,t)\mathrm{d}t = 1 \tag{2.67}$$

we see that it is a certainty, the walker will *always* be absorbed. Interestingly,

if we now ask how long we must wait for this to happen, the mean first passage time to absorption:

$$-\frac{\partial}{\partial s}e^{-|x|\sqrt{s/D}}\bigg|_{s=0} \to \infty \tag{2.68}$$

i.e. the expected time that it will take turns out to be infinite.

2.4 Simulation Techniques

In the final part of this Chapter, I introduce briefly the basic simulation techniques that will be used in most, if not all, simulations in this thesis. As I will mainly be studying reaction-diffusion processes, I carry on with the random walk theme and discuss how to simulate diffusion in both the agent-based and numerical cases. Specific algorithms relating to particular systems will be discussed as they are implemented, i.e. in their relevant chapters.

2.4.1 Agent-based simulations

Agent-based simulations are used to simulate the microscopic dynamics of a system directly. For example, particles diffusing and undergoing chemical reactions can be modelled via an agent-based simulation; each particle's position would be recorded in memory and updated at each time-step according to the rules of the model. They can therefore often be used to test if a macroscopic, e.g. mean-field equation, faithfully reproduces the behaviour of the underlying microscopic model. They tend to be easier to program than solving PDEs as there are usually fewer subtleties, such as stability criteria, to consider. The main issue with agent-based programs is to ensure that the time-step, Δt, is small enough that the dynamics accurately reflect the model. For example, if we are attempting to model particles that diffuse and interact if they collide, we will 'miss' many collisions if the time-step is too large. This is because the time-step is related to the diffusion length scale, which is in practice the average distance each particle will 'jump' during one step, as we will see below. If this length is larger than the interaction radius of the particles, we can see that particles could very easily jump over each other without interacting, which would be unphysical.

This requirement, that Δt is small, coupled with the fact that each particle is simulated individually, means that agent-based simulations can be quite slow as well as computationally expensive. As the details of each particle must be

recorded, they can also take up a great deal of computer memory. Another disadvantage is that stochasticity is now inherent in the system, and is impossible to vary without affecting the other parameters. If we are interested in the effect of the noise itself, as we will be in Chapter 5, the PDE description is more effective as the noise will be represented by a noise term, whose parameter can be varied independently.

Simulating Diffusion

We have a d-dimensional array of particle positions and, at each time-step, we select each particle, i, in turn and draw, for each dimension, a random number $a_r = [0, 1]$, the current position is then updated using:

$$x_{i,j}(t + \mathrm{d}t) = x_{i,j}(t) + (1 - 2a_r)\delta l \qquad j = 1 \ldots d \tag{2.69}$$

$\mathrm{d}t$ and δl are here given in simulation units (usually equal to 1), I relate simulation units to real units via Δt and Δx for time and space respectively, i.e. the maximum distance in real units a particle will hop in one time-step will be $\delta l \Delta x$. In order to find Δt, we need simply to know the 'real' value of the Diffusion constant, D_{real}. We know from the probability distribution Eq. (2.11) that

$$\left\langle x^2 \right\rangle = 2Dt. \tag{2.70}$$

In the simulation, in one time-step, a random walker moves a random distance in the range $[-\delta l, \delta l]$. The probability is flat and hence equal to $1/2\delta l$ over the region:

$$\left\langle x^2 \right\rangle = \frac{1}{2\delta l} \int_{-\delta l}^{\delta l} x^2 \mathrm{d}x = \frac{\delta l^2}{3} \tag{2.71}$$

and therefore (setting $t = 1$ in simulation units):

$$D_{sim} = \frac{\delta l^2}{6} \tag{2.72}$$

and this result applies to higher dimensional random walks as well. In order to restore the dimensions, D_{sim} can be related to D_{real} by $D_{real} = \frac{\Delta x^2}{\Delta t} D_{sim}$. Hence, the value of a time-step Δt can be worked out once the step length δl is fixed and related to a real distance via Δx.

No-Flux Boundary Conditions

In most of the problems this thesis will be concerned with, the particles will be confined to a specified region and cannot escape via diffusion. Analytically this can be represented by no-flux boundary conditions, and is very simple to implement into an agent-based simulation: moves that will take the particle out of the system are simply rejected, the particle doesn't move in the given time-step. This can be justified if we consider it to be a Metropolis-Hastings algorithm [Press 92] where the potential is infinite.

2.4.2 Euler Integration

When we have a mean-field model describing the dynamics of the system, we can opt to simulate this equation directly and bypass the microscopic dynamics entirely. For the random walk case, we have the diffusion equation Eq. (2.10) and solving this amounts to an initial value problem: we seek to take an initial condition and evolve it in time using the equation of interest in order to observe its behaviour.

To do this, we must again discretise time and space, $t_n = t_0 + n\mathrm{d}t$ and $x_j = x_0 + j\mathrm{d}x$, and write $u(x_j, t_n) = u_j^n$. We use the convention called *Forward Time Centred Space* (FTCS) [Press 92], whereby the time-derivative is discretised using *Forward Euler Differencing*:

$$\left.\frac{\partial u}{\partial t}\right|_{j,n} = \frac{u_j^{n+1} - u_j^n}{\mathrm{d}t} + \mathcal{O}(\mathrm{d}t) \tag{2.73}$$

which is accurate to first-order in time, to obtain second-order accuracy would involve using values from the previous time-step, a complication which is unnecessary for our purposes. We use *Centred Space Finite Differencing* for the space derivative:

$$\left.\frac{\partial u}{\partial x}\right|_{j,n} = \frac{u_{j+1}^n - u_{j-1}^n}{2\mathrm{d}x} + \mathcal{O}(\mathrm{d}x^2). \tag{2.74}$$

FTCS is an *explicit* scheme, meaning that all values for the following time-step can be calculated from the values at the current time-step only. In order to analyse the stability of such a method, we use *von Neumann Stability Analysis*, we set:

$$u_j^n = \xi^n e^{ikj\mathrm{d}x} \tag{2.75}$$

where k is a wave number. The equations are unstable if the amplification factor $\xi(k)$ for a given k exceeds 1.

For diffusion, we obtain a centred space discretisation of the second derivative by averaging the left and right differences:

$$\left.\frac{\partial^2 u}{\partial x^2}\right|_{j,n} = \frac{u_{j+1}^n - 2u_j^n + u_{j-1}^n}{\mathrm{d}x^2}. \tag{2.76}$$

Taking Eq. (2.73) and Eq. (2.76) gives for the diffusion equation:

$$\left.\frac{\partial u}{\partial t}\right|_{j,n} = \frac{u_j^{n+1} - u_j^n}{\mathrm{d}t} = D\frac{u_{j+1}^n - 2u_j^n + u_{j-1}^n}{\mathrm{d}x^2}. \tag{2.77}$$

If we insert Eq. (2.75) into the above, we obtain

$$\xi = 1 - \frac{4D\mathrm{d}t}{\mathrm{d}x^2}\sin^2(\frac{k\mathrm{d}x}{2}) \tag{2.78}$$

and requiring that $|\xi(k)| < 1$ yields the following stability criterion:

$$\frac{2D\mathrm{d}t}{\mathrm{d}x^2} \leq 1. \tag{2.79}$$

We see that here, as well as for the agent-based model, our choice of the lattice width $\mathrm{d}x$ constrains the choice of time-step $\mathrm{d}t$. It should be noted that simulating an advection term produces another stability criterion, known as the *Courant condition* [Press 92]:

$$\frac{|v|\mathrm{d}t}{\mathrm{d}x} \leq 1. \tag{2.80}$$

The use of stochastic PDEs with field theories will be described in Chapter 4.

Chapter 3

Bacterial Sedimentation: Fisher Wave with Drift

We seek to analyse the effect of advection on a system of sedimenting and reproducing particles. We will discuss how particles that diffuse and multiply can be described by the Fisher-Kolmogoroff Petrovsky Piscounoff (F-KPP) equation, a non-linear partial differential equation that is prototypical for reaction-diffusion systems. The behaviour of this equation is well-known and I will present some of the background theory that accompanies it in Section 3.1. The main feature of F-KPP is that it admits travelling wave-front solutions, called Fisher waves, and it is striking that the propagation speed of these wave-fronts, the Fisher velocity, can be simply obtained from the linearised version of the equation. This forms the basis of the selection principle, whose derivation is reproduced in Section 3.1.2.

In order to introduce gravity, we consider in Section 3.1.3 particles obeying the F-KPP equation modified by an advection term, which seeks to push particles back towards $x = 0$. This form of the equation is less well known, and with the addition of boundary conditions to represent the container within which the particles are sedimenting, yields a non-equilibrium phase transition between a 'sedimentation' regime with an exponential profile, and another regime showing essentially constant density in the bulk of the suspension. Using both agent-based simulations and numerical integration of the resulting equations, we probe the nature and dynamics of the transition. We will see that it is controlled by the strength of the advection, v, and in particular its relation with the Fisher

velocity, v_f.

This study was inspired by experiments in The University of Edinburgh on the sedimentation of *Escherichia coli* bacteria under gravity and we believe the results can impact upon observations of real systems. At the end of the chapter, I present three similar models where, although each differing from ours in one or more fundamental ways, this analysis could also be of some use: branching-annihilating random walk in the presence of an absorbing wall [Derrida 07], population persistence in rivers and estuaries [Speirs 01], and life and death near a windy oasis [Dahmen 00].

3.1 Background

The field of reaction-diffusion problems has been of interest to chemists, physicists, mathematicians and biologists for some time [Saarloos 03]. Such processes are characterised by the following non-linear differential equation:

$$\frac{\partial \rho(\underline{x},t)}{\partial t} = D\nabla^2\rho(\underline{x},t) + f(\rho(\underline{x},t)) \tag{3.1}$$

where $\rho(\underline{x},t)$ can represent a concentration, the first term is the diffusion portion, with D the diffusion coefficient. $f(\rho)$ quantifies the reaction kinetics, which are usually non-linear. These problems cover a wide range of phenomena, occurring in diverse fields such as biology, population dynamics, plasma physics and fluid dynamics. This is because, with appropriate initial conditions, they can admit travelling wave-front solutions, waves that retain their basic shape as they translate, and these are ubiquitous in nature [Murray 02]. The simplest and prototypical form for $f(\rho)$ was studied and presented by two independent groups in 1937; both R.A. Fisher and a group comprising of mathematicians Kolmogoroff, Petrovsky and Piscounoff studied what is now called the Fisher-Kolmogoroff Petrovsky Piscounoff (F-KPP) equation whilst considering problems in population dynamics [Saarloos 03]:

$$\frac{\partial \rho(\underline{x},t)}{\partial t} = D\nabla^2\rho(\underline{x},t) + \alpha\rho(1-\rho) \tag{3.2}$$

where $\alpha\rho(1-\rho)$ is the growth term controlled by the parameter α.

As mentioned above, the work in this chapter was initially motivated by an in-house experiment studying the density profiles of sedimenting bacteria.

Flagellated bacteria, such as the common *E. coli*, are believed to move by rotating their flagella in one of two directions [Berg 83]: a counter-clockwise motion forms a synchronous bundle of flagella and propels them forward, called a 'run'; a clockwise direction, on the other hand, moves the body in all directions erratically, and this is called a 'tumble'. Runs are roughly in a straight line and have a much larger duration than tumbles, which generate the greatest change in direction. The durations of both runs and tumbles are exponentially distributed and the long-time motion is diffusive, with $D_{\text{eff}} = \nu^2\tau/d$ in d dimensions, if ν is the run speed and τ is its mean duration [Berg 83]. Experiments with *E. coli*, a spherocylinder $\sim 2\mu\text{m}\times 1\mu\text{m}$ and average density $\rho_b = 1.08\,\text{g/cm}^3$, give $\nu = 30\mu\text{ms}^{-1}$, $\tau \approx 1\text{s}$ [Bray 01], and $D_{\text{eff}} \sim \mathcal{O}(100\mu\text{m}^2\text{s}^{-1})$ [Berg 03, Berg 90]. It is interesting to note that an equivalent passive colloid, such as an *E. coli* mutant without flagella, diffusing due to Brownian motion alone, has $D \sim 0.5\mu\text{m}^2\text{s}^{-1}$ at 300 K, and so a thermal diffusion corresponding to running and tumbling would correspond to an effective temperature of $\mathcal{O}(10^4\text{ K})$: the system is far from equilibrium.

Bacteria can also multiply but will be limited by the space and nutrients available. The simplest growth term that satisfies these criteria is the logistic growth model, sometimes called the Verhulst-Pearl model after P.F. Verhulst who first introduced the density-dependent limiting term to the exponential growth model [Verhulst 1838] and R. Pearl who used the equation to model population growth in the United States [Pearl 20]. We expect the population to grow at a birth rate b, this will consist of a constant term b_0 and will decline as ρ increases with a rate k_b: $b = b_0 - k_b\rho$. Similarly, the death rate d will have a constant term d_0 and will increase as ρ increases: $d = d_0 + k_d\rho$. Note this is a first-order approximation: we are assuming that the birth and death rates depend on the number of individuals in the population only. Neglecting space, we expect the population to grow as:

$$\frac{d\rho}{dt} = \lambda\rho \tag{3.3}$$

where λ is the difference between the birth and death rates, $\lambda = b - d$. This gives:

$$\frac{d\rho}{dt} = \alpha\rho\left(1 - \frac{\rho}{\rho_0}\right) \tag{3.4}$$

where $\alpha = b_0 - d_0$ is the growth rate and $\rho_0 = \frac{k_b - k_d}{b_0 - d_0}$ is the saturation density of the species, for example this is $\sim 10^9$ cells/cm^3 for *E. coli* [Bailey 86]. Note that this gives as approximate volume fraction (the ratio of total volume occupied by bacteria to the volume of space available) $\frac{10^9 \times 10^{-18}}{10^{-6}} = 10^{-3}$, which is very small. The concentration being this dilute means we can effectively ignore interactions and helps to justify using normal Fickian diffusion to model *E. coli*.

This, coupled with the diffusive motion detailed above, and setting $\rho_0 = 1$, gives the F-KPP, which therefore provides a good macroscopic description of the behaviour of bacteria in, for example, a growth medium in a flat Petri dish (a shallow lidded dish used by biologists to culture cells).

3.1.1 Steady states, stability and Fisher Waves

We can see by inspection of Eq. (3.2) above that there will be two homogeneous steady states, $\rho = 0$ and $\rho = 1$. If we consider one dimension only, and expect a travelling-wave solution propagating with wave speed c:

$$\rho(x,t) = u(x - ct) = u(z). \tag{3.5}$$

F-KPP then reduces to an ordinary differential equation:

$$\frac{d^2u}{dz^2} + c\frac{du}{dz} + u(1-u) = 0. \tag{3.6}$$

Following [Murray 02], we gain initial information about the wave-front behaviour by using a linear stability analysis. We define a momentum $v = du/dz$, then

$$u' = f(u,v) = v \tag{3.7}$$

$$v' = g(u,v) = -cv - u(1-u). \tag{3.8}$$

Phase plane trajectories are therefore given by

$$\frac{dv}{du} = \frac{-cv - u(1-u)}{v}. \tag{3.9}$$

Through any point in the (u,v) there is a unique curve except at singular points (u_0, v_0) where $f(u_0, v_0) = g(u_0, v_0) = 0$. Inspecting Eqs. (3.7) and

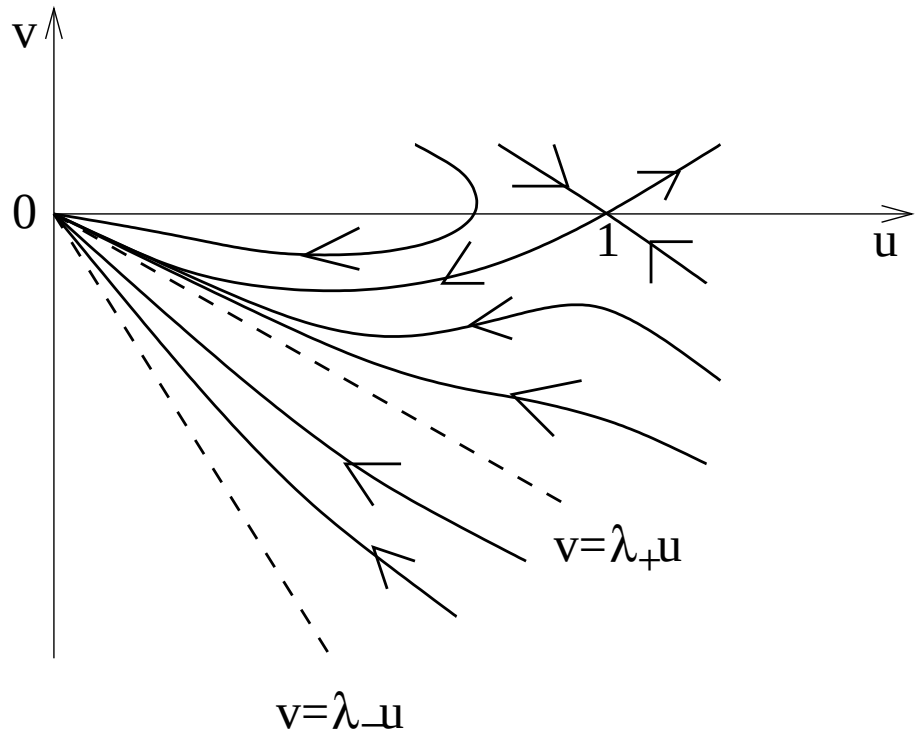

Figure 3.1: Phase plane trajectories for Eq. (3.6) with $\rho_0 = 1$ admitting travelling wave-front solutions ($c^2 > 4$)

(3.8), we see two singular points (0,0) and (1,0) corresponding to the steady states $\rho = 0$ and $\rho = 1$. Using linear stability analysis, we define the matrix $A = \left(\begin{smallmatrix} f_u & f_v \\ g_u & g_v \end{smallmatrix}\right)$:

$$\begin{pmatrix} 0 & 1 \\ -1+2u & -c \end{pmatrix}.$$

Inspection of the eigenvalues of A at the singular points will give information about the phase plane behaviour at these points:

$$(0,0) : \lambda_\pm = \frac{1}{2}\left[-c \pm (c^2-4)^{1/2}\right] \Rightarrow \begin{cases} \text{stable node} & \text{if} \quad c^2 > 4 \\ \text{stable spiral} & \text{if} \quad c^2 < 4, \end{cases} \tag{3.10}$$

$$(1,0) : \lambda_\pm = \frac{1}{2}\left[-c \pm (c^2+4)^{1/2}\right] \Rightarrow \quad \text{saddle point.} \tag{3.11}$$

We see that that (1,0) is a saddle point and the origin can be a stable node if $c^2 > 4$, or a stable spiral if $c^2 < 4$. If $c \geq 2$ and the origin is a stable node, physical solutions are possible, these are trajectories that move from (1,0) to (0,0) keeping $0 \leq u \leq 1$ and $u' \leq 0$. This case is shown in Figure 3.1. What

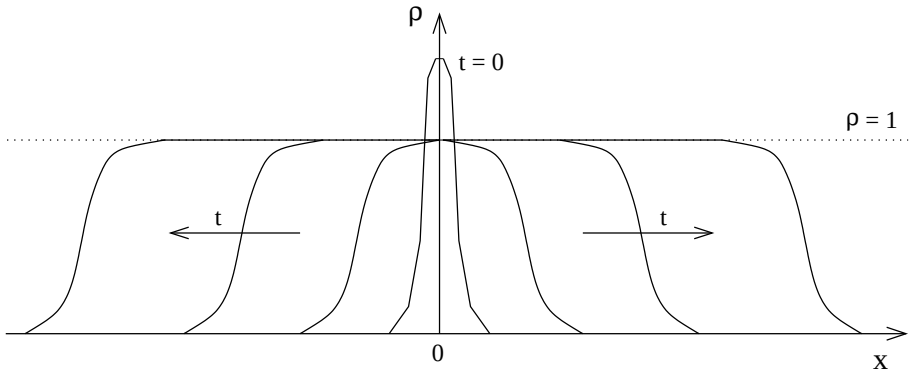

Figure 3.2: Illustration of a travelling wave-front growing outwards from a small high-density region at time $t = 0$.

we see is a wave front, called a Fisher wave, growing out of the $\rho = 1$ state and travelling into the linearly unstable $\rho = 0$ region, leaving everything behind it with $\rho = 1$ (Figure 3.2). It is a remarkable feature that Fisher waves always translate with the lowest possible wave speed, here $c = 2$, whose value can be calculated from a linearised version of F-KPP, and this forms the basis of the Selection Principle derived below.

3.1.2 The Selection Principle

The Selection Principle dictates that, although a whole family of wave speeds could potentially allow perturbations to grow out from the unstable region, in practice only the lowest possible wave speed, the linear spreading velocity or Fisher velocity, v_f, is chosen for the front to propagate with, provided certain criteria for the initial conditions are met[1]. We show this by reproducing the method in [Saarloos 03]. First, we consider the dimensionless version of Eq. (3.2), taking $t \to t/\alpha$ and $x \to \sqrt{D/\alpha}x$, and linearising about $\rho = 0$, we obtain in one dimension:

$$\frac{\partial \rho(x,t)}{\partial t} = \frac{\partial^2 \rho}{\partial x^2} + \rho + O(\rho^2). \tag{3.12}$$

We Fourier transform this equation, using $\tilde{\rho}(k,t) = \int_{-\infty}^{\infty} dx \rho(x,t) e^{-ikx}$:

$$\frac{\partial \tilde{\rho}(k,t)}{\partial t} = (1 - k^2)\tilde{\rho}(k,t). \tag{3.13}$$

[1]specifically that they have compact support, i.e. $u(x,0) = u_o(x) \geq 0$, $u_0(x) = 1$ for $x \leq x_1$ and $u_o(x) = 0$ for $x \geq x_2$, $x_1 < x_2$ and $u_0(x)$ is continuous in the region $x_1 < x < x_2$.

This can be solved by:

$$\tilde{\rho}(k,t) = \bar{\rho}(k)e^{(1-k^2)t}. \tag{3.14}$$

We anticipate a travelling front, travelling with speed $v_f > 0$. We then invert the Fourier transform and change to coordinates co-moving with the front, $\xi = x - v_f t$:

$$\rho(\xi,t) = \frac{1}{2\pi}\int_{-\infty}^{\infty} dk\bar{\rho}(k)e^{ik\xi+(1-k^2+ikv_f)t}. \tag{3.15}$$

At large times, the integral is dominated by $k = k^*$, we therefore use a saddle-point approximation:

$$\frac{d}{dk}(1-k^2+ikv_f)\bigg|_{k=k^*} = 0. \tag{3.16}$$

Solving this for the wave velocity, v_f, gives

$$v_f = -2ik^*. \tag{3.17}$$

We decompose $k^* = k_r + ik_i$, and by requiring v_f be real, obtain $v_f = 2k_i$. Now, to ensure that the front is stable, the solution must neither grow nor decay exponentially with time and therefore the following must apply:

$$1 - k^{*2} - v_f \mathrm{Im}[k^*] = 0. \tag{3.18}$$

Hence, by substituting Eq. (3.17) into the above, we obtain $k_i = \pm 1$ and finally $v_f = 2$. Restoring the original dimensions, we find the Fisher velocity:

$$v_f = 2\sqrt{D\alpha}. \tag{3.19}$$

3.1.3 F-KPP with advection

We are interested in the density profiles of sedimenting bacteria, we therefore use Eq. (3.2) above and add an advection term, $v\frac{\partial \rho}{dx}$ to model the effect of gravity. We now interpret x as a height within a container, with $x = 0$ at the bottom, $\rho(x,t)$ represents the concentration of organisms at this height at time t. Particles within the container can diffuse and multiply and the advection term seeks to push them back towards the origin. This yields the following

equation:

$$\frac{\partial \rho(x,t)}{\partial t} = D\frac{\partial^2 \rho}{\partial x^2} + v\frac{\partial \rho}{\partial x} + \alpha\rho(1-\rho). \tag{3.20}$$

It is important to note that the boundaries play an important role here. As we are interested in a real system, i.e. bacteria in a box, we impose no-flux boundary conditions at the top and bottom of the container. The boundary conditions are given by:

$$D\frac{\partial \rho}{\partial x} + v\rho\Big|_{x=0,L} = 0. \tag{3.21}$$

As is often the case in non-equilibrium systems [Schutz 93], the boundaries are crucial, as, without them, one can simply transform away the advection term using a Galilean transformation, i.e. changing to a frame co-moving with the advection would restore the original F-KPP equation [Dahmen 00]. The presence of boundaries negates this possibility, and they play an important role in the resulting observed behaviour.

If we rescale space and time in Eq. (3.20), by taking $t \to Dt/v^2$ and $x \to Dx/v$, the equation now exhibits a dimensionless control parameter, $\lambda = D\alpha/v^2$:

$$\frac{\partial \rho(x,t)}{\partial t} = \frac{\partial^2 \rho}{\partial x^2} + \frac{\partial \rho}{\partial x} + \lambda\rho(1-\rho). \tag{3.22}$$

The parameter, λ, modulates the effect of the non-linear term, and is small as the growth rate is assumed small. This suggests we try to obtain a perturbative solution by expanding in powers of λ. $\lambda = 0$ clearly restores normal colloidal sedimentation, whereby we would observe, as steady states, exponentially-decaying density profiles $\rho(z) \propto \exp(-vx/D)$. A linear stability analysis, similar to the one employed above, gives for the fixed point at the origin the following eigenvalue:

$$\gamma_{\pm}^{(0,0)} = \frac{1}{2}\left[-(c+1) \pm \sqrt{(c+1)^2 - 4\lambda}\right] \Rightarrow \begin{cases} \text{stable node} & \text{if} \quad (c+1)^2 > 4\lambda \\ \text{stable spiral} & \text{if} \quad (c+1)^2 < 4\lambda. \end{cases} \tag{3.23}$$

The condition for travelling wave-fronts becomes $c > 2\sqrt{\lambda} - 1$ and c can now change sign depending on the magnitude of λ. This is the first indication that something occurs in the system at the threshold $\lambda_c = \frac{1}{4}$. The linearised problem tells us that the steady-state solution will likely be a perturbation

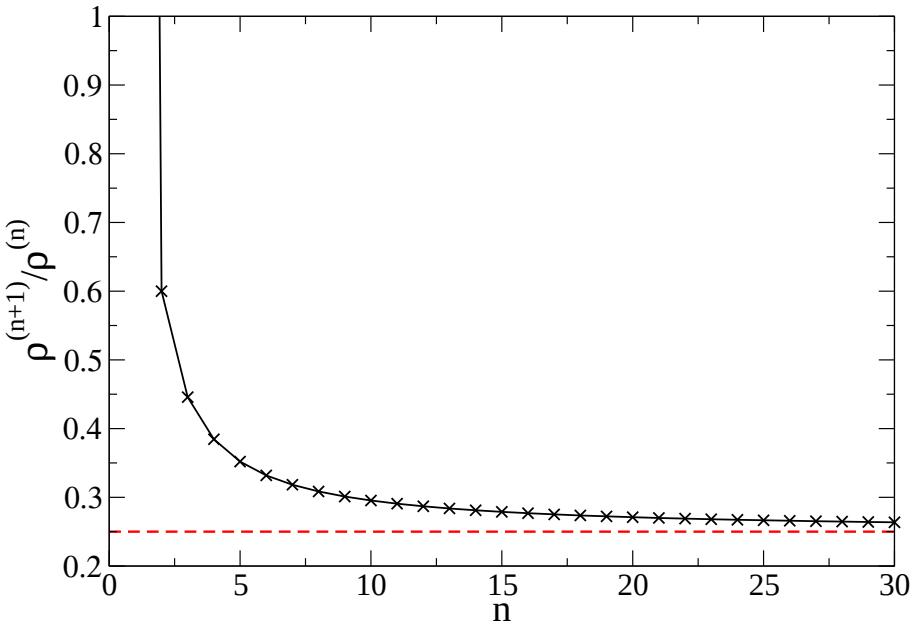

Figure 3.3: Radius of convergence test for series solution $\rho(x) = \sum_n \lambda^n \rho^{(n)}(x)$. The dashed red line indicates the $\lambda = \frac{1}{4}$ convergence threshold.

about the solution for Eq. (3.22) with $\lambda = 0$. We calculated an expansion for small λ using the first 30 terms of a series expansion $\rho(x) = \sum_n \lambda^n \rho^{(n)}(x)$ [Barrett-Freeman 07]. The series indeed converges for $\lambda < \lambda_c$ and diverges otherwise (Figure 3.3) (with $\rho(x)$ within this radius of convergence being very close to the $\lambda = 0$ solution); we will have to consider the full non-linear problem if we are to see what happens when $\lambda > 1/4$. It is also interesting to note from the definition of λ:

$$\lambda = \frac{D\alpha}{v^2} = \frac{1}{4}\left(\frac{v_f}{v}\right)^2 \tag{3.24}$$

i.e. the threshold occurs when the sedimentation velocity, v, exactly equals the Fisher velocity, v_f.

3.2 Agent-Based Simulation

Although, for the reasons given above, we believe our continuous equation will give a good macroscopic description for the system of sedimenting reproducing particles, the system itself is inherently stochastic whereas Eq. (3.20) is deterministic. One route would be to add an explicit noise term to Eq. (3.20), and this is the subject of the following chapter. In this chapter, however, we are

interested in the effect of advection on a system of sedimenting bacteria; the form of the noise in the real system would be difficult to specify and its magnitude would also be hard to quantify. We therefore use a stochastic algorithm to simulate the microscopic behaviour directly with a view to compare with our analysis and eventual simulations of the mean-field equation itself. Now, Eq. (3.20) represents the diffusion and growth of a concentration that is always in the range [0,1] and we want to simulate a number of particles. To do this, we re-introduce ρ_0, to represent the limiting population size. Our growth term becomes $\alpha\rho(1-\rho/\rho_0)$ so that the steady state concentrations are now 0 and ρ_0.

We create a lattice of sites $i = 1, \dots L$, each site represents a horizontal 'slice' of the container at height $x = i\Delta x$. The occupation number, $n_i(t)$, will then be the number particles existing between height $i\Delta x$ and $(i+1)\Delta x$. In each time-step, $t \to t + \Delta t$, the array of occupation numbers is updated according to a 'multiply' step or a 'move' step detailed below. Δt is large enough to guarantee that something happens and the system chooses which step to implement stochastically with probability $\frac{1}{1+w}$ for a 'move' step or $\frac{w}{1+w}$ for a 'multiply' step. w, therefore, is a non-local term chosen to represent the ratio of the total rate of reproduction/death per particle to the total rate of moving per particle.

In a 'move' step, each particle can move independently up or down with probability p or $1-p$. The continuum limit of this process leads to a diffusion constant with $D = \frac{\Delta x^2}{2\Delta t}$ and sedimentation velocity $v = (1-2p)\frac{\Delta x}{\Delta t}$, and hence p is the parameter that controls the strength of the gravitational force. The total rate of moving per particle is therefore:

$$\frac{\sum_{i=1}^{L} n_i p + n_i(1-p)}{\sum_{i=1}^{L} n_i} = 1. \tag{3.25}$$

In a 'multiply' step, each site is updated in the following way: each particle is either replaced by two particles in the same site with probability $\frac{\rho_0}{n_i(t)+\rho_0}$, or is annihilated with probability $\frac{n_i(t)}{n_i(t)+\rho_0}$. In order to correctly model Eq. (3.20) with the new growth term outlined above, we want the growth rate on each site to be αn_i and the death rate to be $\alpha n_i^2/\rho_0$. Thus, the total rate of reproduction/death

per particle will be:

$$\alpha \frac{\sum_{i=1}^{L} n_i + \sum_{i=1}^{L} n_i^2/\rho_0}{\sum_{i=1}^{L} n_i} = \alpha \left(1 + \frac{\sum_{i=1}^{L} n_i^2}{\rho_0 \sum_{i=1}^{L} n_i}\right). \tag{3.26}$$

Thus setting w (the ratio of the above total rates) to:

$$w = \alpha \left[1 + \frac{\sum_{i=1}^{L} n_i^2}{\rho_0 \sum_i n_i(t)}\right] \tag{3.27}$$

ensures that Eq. (3.20) is indeed the continuous limit of our microscopic simulation. The simulation is carried out using the following algorithm at each time-step:

- Choose whether the current time-step is a 'move' (probability $\frac{1}{1+w}$) or a 'multiply' (probability $\frac{w}{1+w}$) step
- In a 'move' step: move every particle 'up' or 'down' with p or $1-p$ respectively.
- In a 'multiply' step: 'multiply' or 'annihilate' every particle with $\frac{\rho_0}{n_i(t)+\rho_0}$ or $\frac{n_i(t)}{n_i(t)+\rho_0}$ respectively.
- Increment the time-step

Note that the state where the lattice is devoid of particles is an absorbing state of the dynamics in the algorithm, which we call model I. We also considered a variation of the dynamics, which we refer to as model II, in which a depopulated site is allowed to be repopulated spontaneously (during the reproduction/death move).

No-flux boundaries are implemented by simply rejecting a move that attempts to remove a particle from the system.

3.3 Results

3.3.1 Non-equilibrium Phase Transition: v versus v_f

Our simulations show a phase transition between two different regimes. If the particles reproduce slowly (α small), we obtain a steady-state density profile which decays sharply with x, as shown in Figure 3.4 (a). We call this the

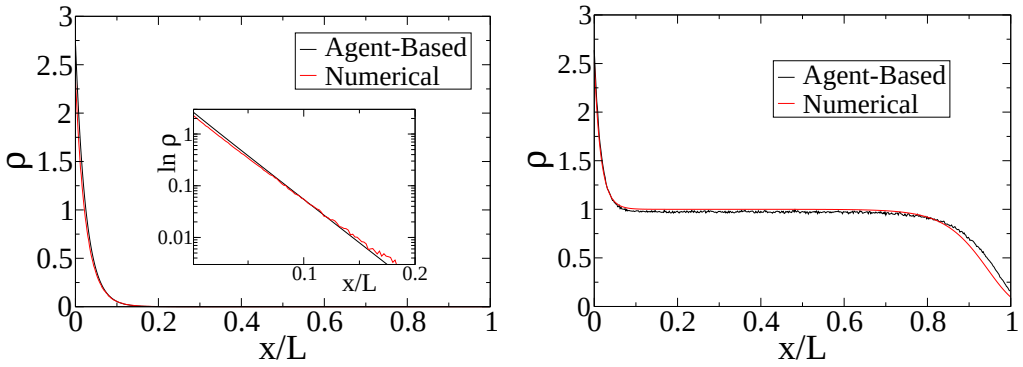

Figure 3.4: The average density, ρ, versus height, x, for a suspension of motile and reproducing active particles in a gravitational field. Simulation results (model I), with (a) $v = 0.7v_c$, and (b) $v = 1.8v_c$.

'sedimentation regime' in analogy with the similar behaviour of passive colloids under gravity. If the growth rate exceeds a threshold, α_c, the steady state is one with a uniform density throughout the bulk of the sample, with depleted and enriched layers in the top and the bottom of the container, see Figure 3.4 (b). We call this the 'growth regime'.

In model II[2], we find the critical value by inspecting the density profiles and locating the point at which it is no longer an exponential: it is close to $\alpha_c = \frac{v^2}{4D}$. As mentioned above, $\alpha = \alpha_c$ corresponds to exactly the point where the sedimentation velocity, v, equals the advancing Fisher wave velocity, v_f. This phase transition can therefore be understood as competition between the two velocities, one trying to push the population to the bottom of the container and one trying to raise it to the top.

3.3.2 Numerical Simulation of the PDE

Using a standard finite-difference scheme (see Chapter 2), the mean-field equation can be discretised in space into sites i with width dx, and in time with

[2]In model I, the presence of an absorbing state widens the sedimentation regime, shifting α_c to a slightly larger value.

timestep dt:

$$\begin{aligned}\frac{\rho_i(t+\mathrm{d}t)-\rho_i(t)}{\mathrm{d}t} =& \frac{D}{\mathrm{d}x^2}\Big(\rho_{i+1}(t)+\rho_{i-1}(t)-2\rho_i(t)\Big) \\ &+\frac{v}{2\mathrm{d}x}\Big(\rho_{i+1}(t)-\rho_{i-1}(t)\Big) \\ &+\alpha\Big(\rho_i(t)-\frac{\rho_i^2(t)}{\rho_0}\Big).\end{aligned} \tag{3.28}$$

To ensure convergence of a solution, care must be taken, as shown in the previous chapter, that $\mathrm{d}t < \mathrm{d}x^2/2D$. In addition to this criterion, it was found numerically that the velocity must obey $v < \frac{2D}{\Delta x}$. This can be found from the condition for stability of the diffusion equation by substituting in the definition $v = \Delta x/\Delta t$.

To implement no-flux boundary conditions, we simply discretise the derivative using the same scheme as in the bulk (FTCS), this leads to the following equation at the boundary:

$$D\frac{\rho_3-\rho_1}{2\mathrm{d}x}+v\rho_1=0. \tag{3.29}$$

Although this equation works perfectly well for the problem considered here, we ran into difficulty when looking at the low-density transitions in Chapter 5 and we therefore changed to a different discretisation for the boundary, details can be found in section 4.3.4.

Defining the dimensionless parameter $\theta = \frac{v}{\sqrt{D\alpha}}$, the existence of a non-equilibrium phase transition at $\theta = \theta_c = 2$ is confirmed by numerical simulation of the PDE and gives remarkably similar density profiles as the stochastic agent-based simulation as can be seen in Figure 3.4. We therefore use direct numerical integration of Eq. (3.20) from this point forward as it is computationally more efficient.

3.3.3 Classification of the Transition

It is interesting to consider the behaviour of the decay length, l, of the exponential density profile in the sedimentation regime (an effective sedimentation length) as a function of $|\theta - \theta_c|$ (Figure 3.5). This sedimentation length is akin to a scaling length in an equilibrium phase transition. We find that after correcting for a small L-dependent shift in θ_c, the sedimentation length does

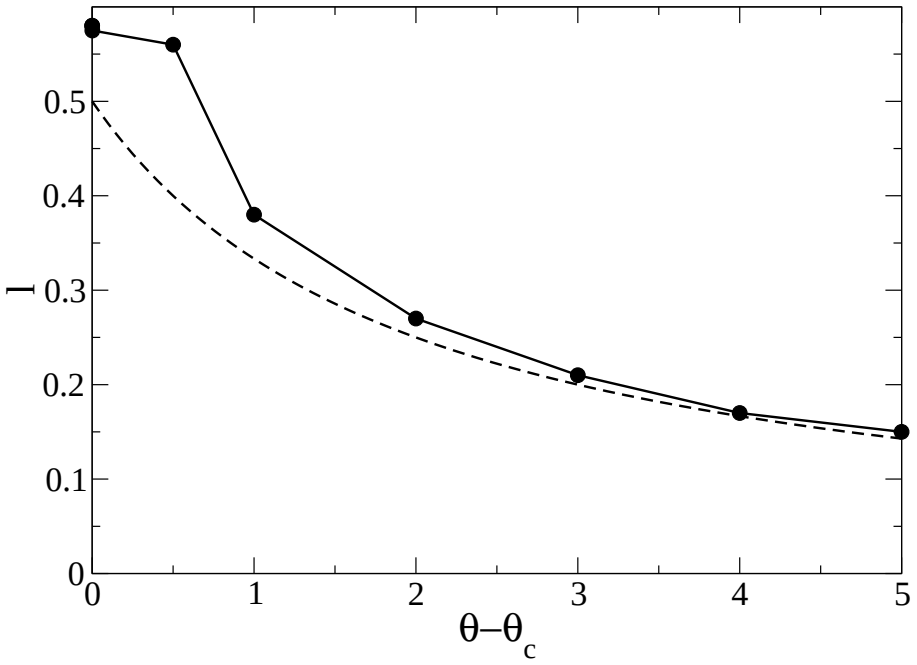

Figure 3.5: The dependence of the sedimentation length, l, on the distance from the critical point $\theta - \theta_c$; the dashed line gives the colloidal value at $\alpha = 0$ ($l = D/v$)

not diverge at the transition, and is only at most $\sim 20\%$ larger than the corresponding sedimentation length with no growth ($\alpha = 0$). Furthermore, if we focus on the steady state concentration value e.g. in the middle of the sample, it switches abruptly, for $L \to \infty$, from 0, for $\theta > \theta_c$, to 1, for $\theta < \theta_c$ (Figure 3.6). These observations are consistent with a discontinuous phase transition.

3.3.4 Finite Size Effect: Banding

For large but finite systems, we find evidence of an intriguing spontaneous banding of the sedimenting particles, which occurs very close to $\theta = \theta_c$. An example is shown in Figure 3.7, in which two steady-state regions coexist in the bulk of the sample, one in which ρ is practically 0 and another one in which it is ~ 1. This kink-like solution, which we call a 'sedimentation band', is similar to a *cline*, found in the population biology literature when solving a reaction-diffusion equation, similar to Eq. (3.20), but with $v = 0$ and a reaction term which is cubic in ρ [Barton 89]. However here we have a boundary between a

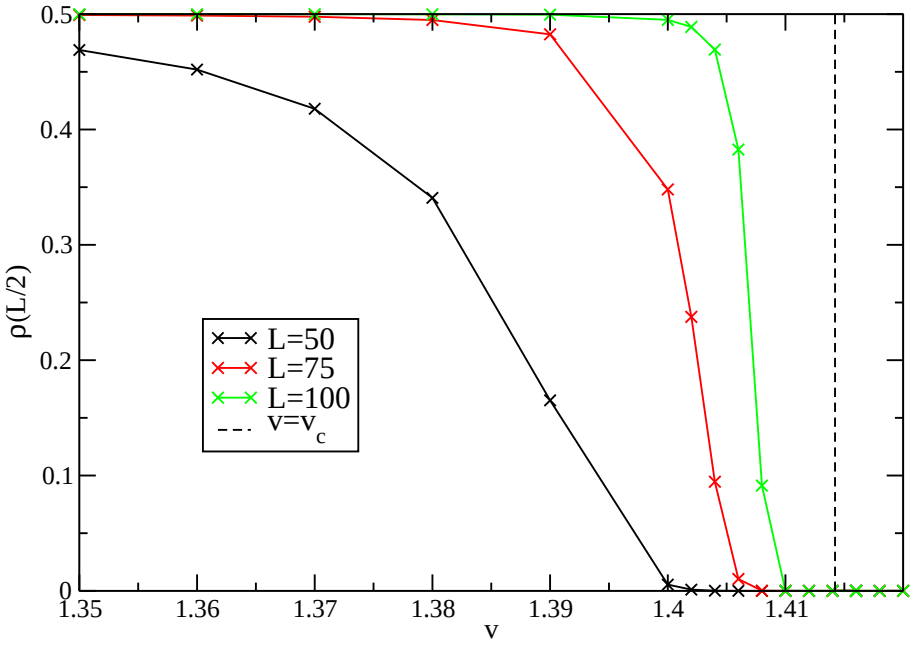

Figure 3.6: The steady-state value at the mid-point of a system with size $L = 50$ (black), $L = 75$ (Red) and $L = 100$ (Green). The maroon line corresponds to the analytic value $v = v_c = \sqrt{2}$

stable and an unstable (or meta-stable) state whereas in [Barton 89] the 'cline' separates two stable states.

In our case then, the existence of sedimentation bands is more surprising, as without advection the state at $\rho = 0$ is unstable, and bands arise due to the vicinity of a phase transition. In this respect, our sedimentation banding is more akin to shear banding, which is obtained when some complex fluids such as liquid crystals and worm-like micelles in the isotropic or disordered phase, are subjected to a shear, slightly smaller than that needed to order them completely [Lu 00].

The position of the band is extensive with the system size, though how it scales is not known; thus the region 'behind' it properly corresponds to the growth regime. This coexistence of the phases also gives further evidence that the transition is discontinuous. Finally, the bands appear in an increasingly small window of θ as L increases, and disappear in the thermodynamic ($L \to \infty$) limit (Figure 3.8).

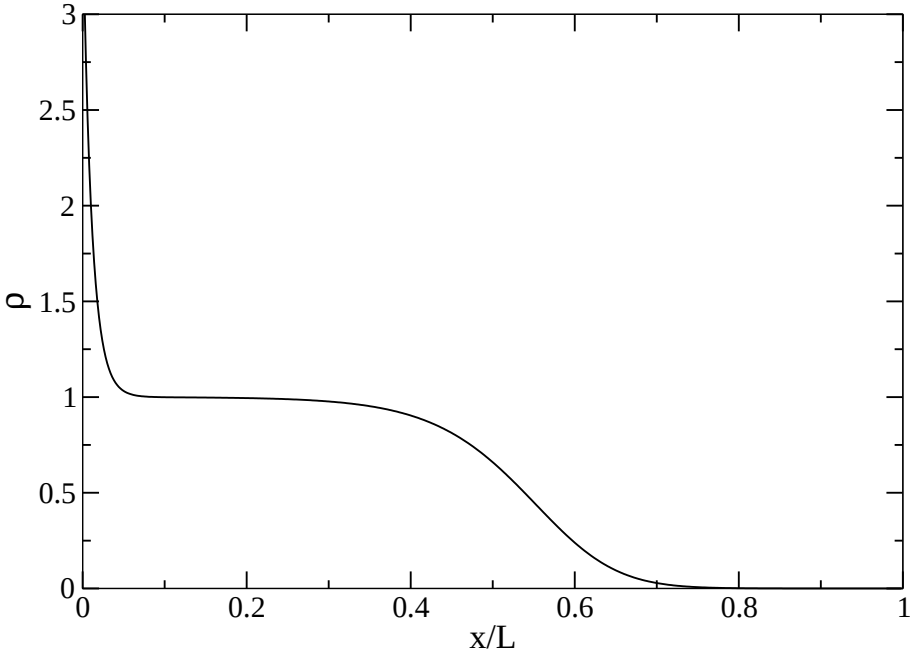

Figure 3.7: An example of a band: the average density, ρ, versus height, x, for a suspension of motile and reproducing active particles in a gravitational field. Numerical results of the PDE with $v = 0.976v_c$ and $L = 50$

3.3.5 Dynamics

The pathway to steady state may be quite slow. This is particularly true close to $\theta_c(L)$, and in the region where sedimentation bands form. In the banding regime for large sample size L, we also find that the behaviour of the part of the sample close to the top, or just after the boundary of the band, displays non-monotonic behaviour: the density first increases with time, as if the systems transiently entered the uniform regime, to decay later on to reach equilibrium (Figure 3.9 (a)). The time scale needed to reach equilibrium[3], $t_{\rm eq}$, is plotted in Figure 3.9 (b) as a function of velocity. Larger systems take longer to equilibrate, while close to criticality we find that $t_{\rm eq}$ increases as a power law of $|\theta - \theta_c|^{-a}$, with $a \simeq 1$ above the transition, and $\theta_c \to 2$ as L is increased (See Figure 3.10). This confirms the presence of a phase-transition at $\theta_c = 2$ and is consistent with [Derrida 07], where the authors look at a similar system and find t_{eq} using

[3]This is defined by the total mass of the system changing by an amount less than 10^{-5} in between two instances of recording the density

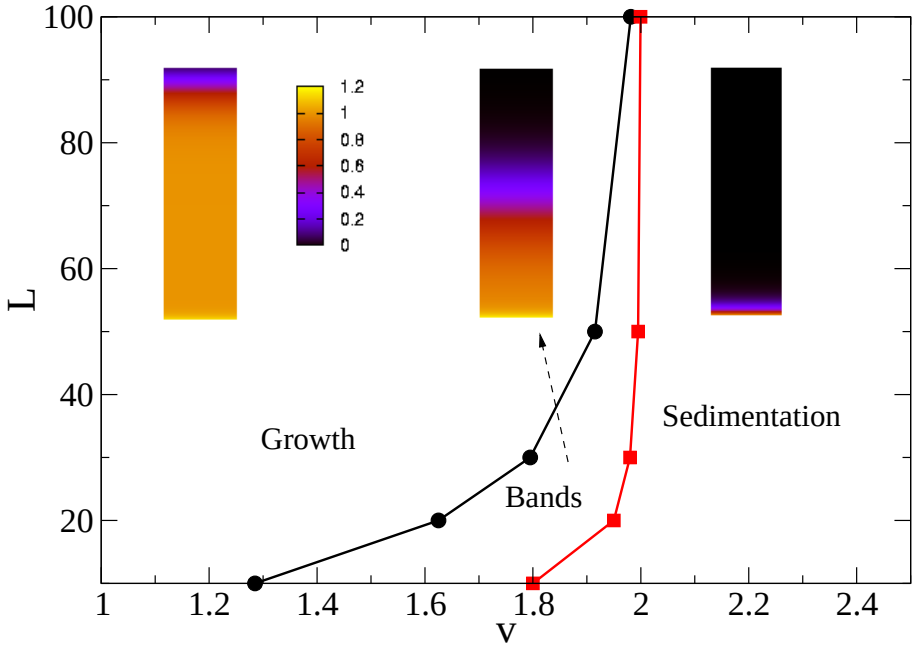

Figure 3.8: Steady state phase diagram in the (v, L) plane for the noise-less version of Eq. (3.20) with $\alpha = 1$. A density profile is classified as 'banded' if the cline stays in the bottom 75% of the sample. Typical concentration profiles in the various regimes are also shown, together with a colour scale for the density.

analytic arguments, summarised at the end of the chapter.

3.3.6 Observation

Would it be possible to observe the transition we predict in a real bacterial suspension? For *E. coli* in water, $v \lesssim 0.1\mu\text{ms}^{-1}$ [Klaus 97] and is fixed, while $D \gtrsim 100\mu\text{m}^2\text{s}^{-1}$ [Berg 90]. In rich, well-aerated media maintained at the optimal temperature of 37°C, the population doubles every ~ 20 minutes, giving $\alpha \sim 10^{-3}$ s^{-1}, and $\theta \approx 0.3$. It is possible to culture the bacterium in what is known as 'motility buffer', in which D is maintained, but growth essentially stops ($\alpha \to 0$). This allows the tuning of θ from 0.3 through 2 to arbitrarily large values, thus permitting the observation of our transition in principle. However, the timescales necessary to perform experiments with real bacteria on the macroscale hinder the gathering of data significantly.

Figure 3.11 shows stills from an experiment involving bacterial sedimenta-

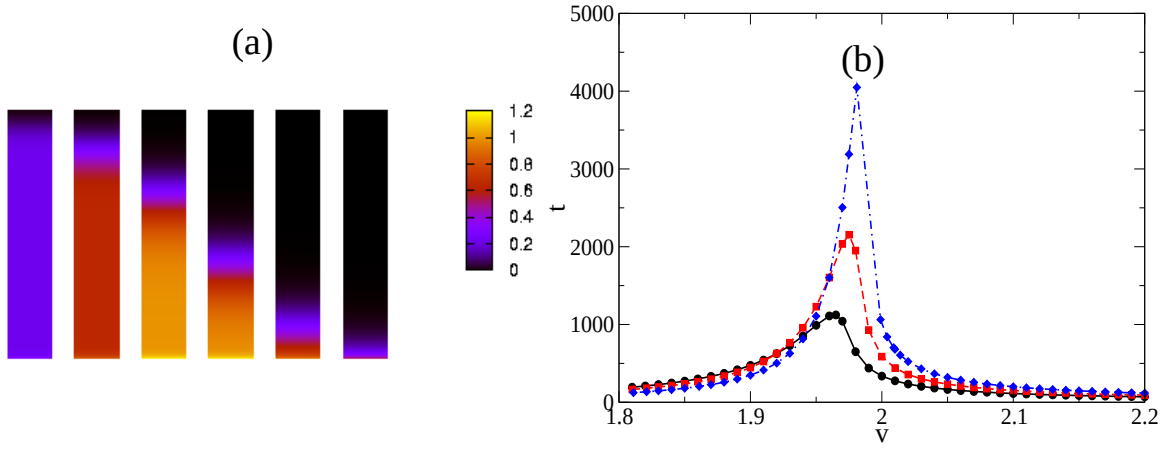

Figure 3.9: (a) Dynamics of the density profile in a system with $L = 30$ (in units of $\sqrt{D/\alpha}$), and with $v = 1.05v_c$. The times corresponding to each profile are (from left to right) 0.99, 2.8, 17.5, 62.2, 121.4, 250 (in units of α^{-1}, the bottom 5% of the sample is cut for colour readability). (b) Plots of the time needed to get to steady state, (in units of α^{-1}), as a function of v (in units of $\sqrt{D\alpha}$), with a system with $L = 20$ (solid line), $L = 28$ (dashed line) and $L = 40$ (dot-dashed line). (L is in units of $\sqrt{D/\alpha}$.) Steady state is defined here as the change in total mass being less than 10^{-5} in 1 second.

tion. The medium is Lysogeny Broth (LB) [Bremer 96] which has a growth rate of 1/30 min^{-1}. According to our analysis, the observed sedimentation is unexpected as the system is in the growth regime though not very far: $\alpha_c = \frac{(10^{-7})^2}{2\times10^2\times10^{-12}} = 5 \times 10^{-5}\text{sec}^{-1}$ and $\alpha \simeq 5.6 \times 10^{-4} \ll \alpha_c$. However, there was a problem in the experiment due to bacteria dying and then behaving like normal colloids. We also see that the experiment lasted several days and this poses another obstacle: the dynamics predict that close to the transition, it may take up to several months for a column of 10 cm height to reach steady state!

There have been recent advances in microfluidics that look promising in this regard. In [Palacci 10], the authors use chemically-powered colloids to observe sedimentation of active particles, environmental factors are easier to control and the timescales involved are far shorter than when using real bacteria.

3.3.7 Similar Systems

The following systems all share similarities with the model described above but differ mainly in the choice of boundary conditions. This different resulting

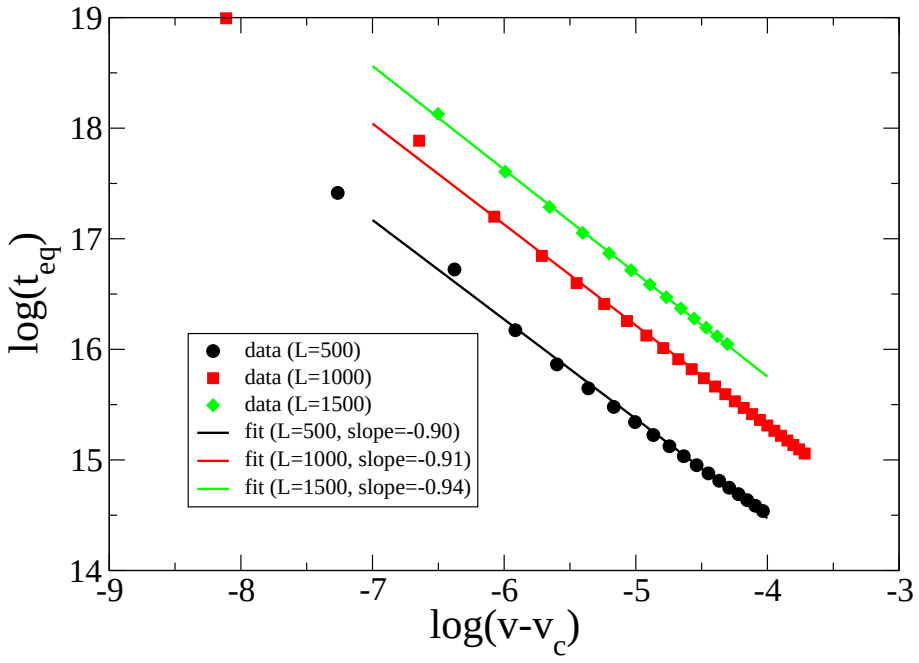

Figure 3.10: The log of the equilibration time, t_{eq}, defined in Figure 3.9, as a function of the log of the distance from the critical point $v - v_c$. Three system sizes are shown: $L = 500$ with $v_c = 1.9923$, $L = 1000$ with $v_c = 1.9957$, and $L = 1500$ with $v_c = 1.9965$, represented by black circles, red squares and green diamonds respectively. The slopes, fitted using Gnuplot, are shown by the solid lines and are clearly approaching 1, as expected by the analytic argument given in [Derrida 07].

phenomena shows that the choice of boundary is indeed crucial to the behaviour observed.

Branching-Annihilating Random Walk in the Presence of an Absorbing Wall

In [Derrida 07], the authors study a system where a particle undergoes a branching random walk in one dimension, whose offspring can be absorbed by a wall advancing in the positive x-direction at speed v. The particles multiply with rate β and the quantity of interest is $Q(x, t)$, defined as the survival probability at time t of the descendants of a particle at x at time $t = 0$. In effect, $1 - Q$ is the extinction probability of the system; they show that $Q(x, t)$ obeys the

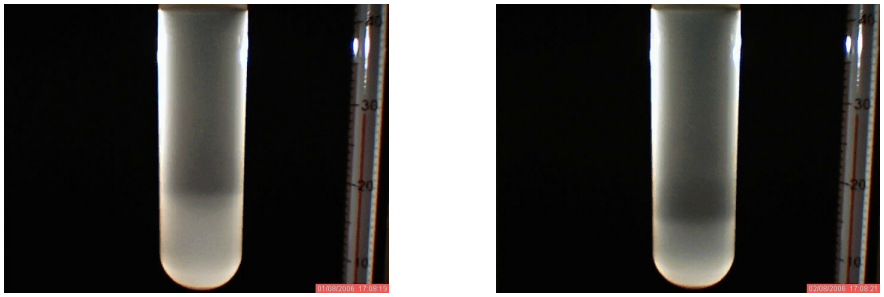

(a) (b)

Figure 3.11: Stills from a video showing E.Coli AB1157 (grown to stationary phase at 37C) sedimenting in a cylindrical test tube in LB at 30C. The video was made by dark field time lapse photography (at 1h intervals) between 5pm on the 1st and 10am on the 3rd of August 2006. (a) shows the start of the experiment and (b) is 1 day later. Images courtesy of O. Croze.

following equation:

$$\frac{\partial Q(x,t)}{\partial t} = D\frac{\partial^2 Q}{\partial x^2} - v\frac{\partial Q}{\partial x} + \beta Q(1-Q) \tag{3.30}$$

which is just Eq. (3.20) with $v \to -v$. Besides this, their boundaries are quite different, with $Q(0,t) = 0$ and $Q(x,0) = 1$ and the system inhabiting a semi-infinite line.

They find a similar phase transition at $v = v_c = 2\sqrt{\beta}$, with the $v > v_c$ phase exhibiting a backwards-propagating Fisher Wave at speed $(v - v_c)$ leaving everything behind in the $Q = 0$ steady state. If $v < v_c$, they recover the shape of the wave described above, except it is now stuck to the $x = 0$ boundary. Finally, if $v \lesssim v_C$, they find the wave advances a distance L into the space and then becomes stuck. This is similar to the bands observed in our system except that they find that L diverges as $v \to v_c$, whereas in our case, even in the infinite system-size limit, the band would be stuck at a well-defined point in the middle of the space if $v = v_c$ exactly.

The authors obtain the relaxation time to steady state τ: by considering the

linearised steady-state equation:

$$0 = Q'' - vQ' + \beta Q \tag{3.31}$$

and by substituting the trial function $Q \sim e^{\gamma x}$, it can be seen that there will be 3 different solutions depending on whether $(v - v_c)$ is positive, negative, or zero. Only the results are quoted here, details of the calculations can be found by the interested reader in [Derrida 07]. Looking first at the $v < v_c$ case and matching it to the critical solution $v = v_c$ near $x = L$, the following steady-state solution can be calculated:

$$Q(x) = \frac{AL}{\pi} \sin\left(\frac{\pi x}{L}\right) e^{v/2(x-L)} \tag{3.32}$$

where $L = \frac{2\pi}{(v_c+v)^{1/2}(v_c-v)^{1/2}}$.

They then write $L = L(t)$, and solve for $L(t)$ by substituting the above solution into the time-dependent but linearised version of Eq. (3.30). Finally, taking a large v gives the relaxation time:

$$\tau \sim |v - v_c|^{-\frac{3}{2}}. \tag{3.33}$$

Using a small v expansion, they find that $L \sim t^{\frac{1}{3}}$.

The $v > v_v$ region is derived by analytic continuation of the $v < v_c$ region explained above. They find that $L(t) \simeq (v - v_c)t$ and the characteristic relaxation time diverges as:

$$\tau \sim |v - v_c|^{-1}. \tag{3.34}$$

As mentioned above, the relaxation time here corresponds with the equilibration time in our system, the exponent for the region above the transition shown in Figure 3.10 is clearly approaching one. The exponent for the region below is shown in Figure 3.12, the values of v_c used to plot $v - v_c$ above the transition are also used here for consistency, and the slope is fitted to the data for the largest available system. The exponent is close to 1.5 as predicted above.

Population Persistence in Rivers and Estuaries

In [Speirs 01], the authors discuss river populations which are subjected to a continual downstream drift. If this is the only transport process considered, any population inhabiting the river is guaranteed to become extinct. This is the "drift paradox" and they attempt to solve it by considering random motion

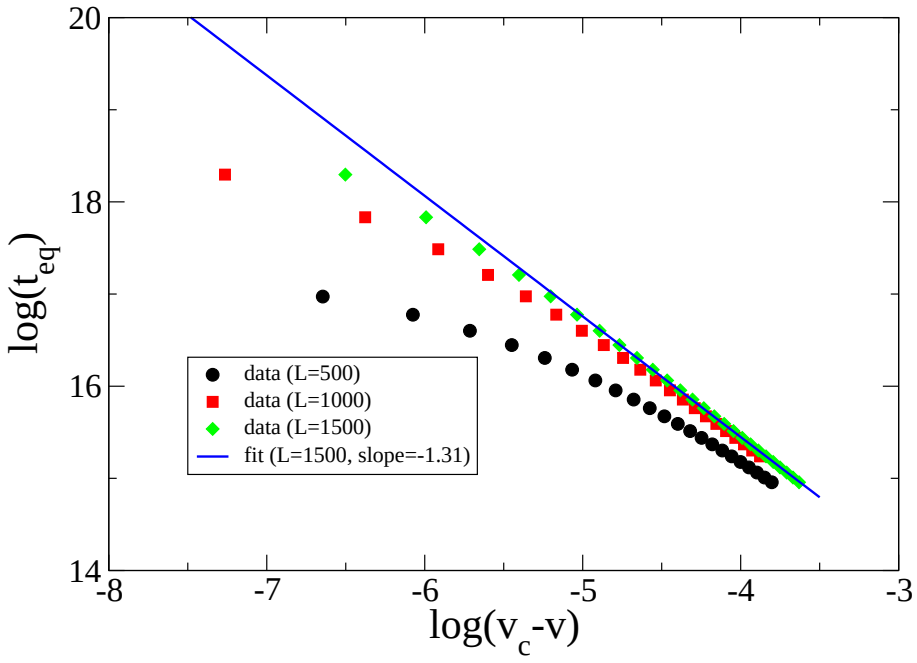

Figure 3.12: The log of the equilibration time, t_{eq}, defined in Figure 3.9, as a function of the log of the distance from the critical point $v_c - v$. Three system sizes are shown: $L = 500$ with $v_c = 1.9923$, $L = 1000$ with $v_c = 1.9957$, and $L = 1500$ with $v_c = 1.9965$, represented by black circles, red squares and green diamonds respectively. The slope fitted to the $L = 1500$ data, is shown by the solid blue line. Its value is close to 1.5, the expected value from the analytic argument given in [Derrida 07]. The discrepancy is not entirely unsurprising given that the graph is very sensitive to the position of the critical point, which itself depends on the system size and is not known exactly. The fit was calculated using Gnuplot's iterative algorithm; after supplying starting values for the slope and intercept, the program finds an iterative solution for the straight line.

due to turbulence and directed movements by individuals which they find to be a key element in population persistence. In the case of a 1-dimensional well-mixed river, they describe the dynamics of the population by:

$$\frac{\partial n(x,t)}{\partial t} = \Phi \frac{\partial^2 n}{\partial x^2} - v\frac{\partial n}{\partial x} + p(n)n. \tag{3.35}$$

Importantly, their boundary conditions differ to ours in that they have an absorbing boundary at the 'downstream' end of the river $x = L$:

$$n(L, t) = 0 \tag{3.36}$$

The upstream boundary condition is no-flux and identical to the one used in this chapter.

By considering a non-linear form of $p(n)$, specifically $p(n) = r(1 - \frac{n}{k})$, they find two possible scenarios: population 'extinction' and 'persistence', controlled by the value of the diffusion coefficient Φ. The dynamics to steady state, as well as the steady-state profiles, are quite different in the two scenarios. In the extinction case, a wave of concentration grows out from a small perturbation, increasing in magnitude as it translates and leaving little or no concentration behind. This wave reaches the absorbing boundary and the population doesn't survive. In the other case, the wave exhibits similar behaviour but the diffusion ensures that some concentration remains in the low x portion of the system, the population therefore persists.

Life and Death near a Windy Oasis

In [Dahmen 00], the authors consider modifying F-KPP in order to model a colony living near or on a favourable patch (of nutrients), an 'oasis', in the presence of a convective velocity, 'wind'. They find a transition between the case where the wind strength, v, is greater than a critical value, v_c, where the population is blown into the 'desert' and becomes extinct, and a case, $v < v_c$, where a steady-state concentration remains near the oasis and survives, although they do not go on to explain this as a phase transition in statistical physics terms. If the desert permits a small population to exist, the transition becomes a de-localisation transition. They use the following equation:

$$\frac{\partial c(\mathbf{x}, t)}{\partial t} = D\nabla^2 c - \mathbf{v}.\nabla c + U(\mathbf{x})c - bc^2 \tag{3.37}$$

All of their interesting behaviour stems from the spatially-varying growth rate $U(\mathbf{x})$, in fact, they claim that the convective drift has no effect on the growth of the bacteria in the case when $U(\mathbf{x})$ is a constant. This is because they consider only periodic boundary conditions, which means that the advection is effectively 'washed away': the original F-KPP equation can be restored by a simple change

of coordinates [Saarloos 03].

3.4 Summary

We have seen that the addition of an advection term to the well-known F-KPP equation has far-reaching consequences, with the caveat that we consider a finite system. As is often the case with non-equilibrium problems, the boundary conditions play a very important role and here, in particular, the usual periodic boundary conditions would in fact remove the effects of advection completely.

We found a discontinuous non-equilibrium phase transition between the usual sedimentation solution, if advection wins over the Fisher waves that attempt to 'invade' the rest of the system, and a solution which is constant in the bulk, visible when the growth is dominant. We have discussed the dynamics to steady state and remarked that although it should be possible to observe this transition in principle, in practice it may take rather a long time to equilibrate. Finally, we looked at the banding regime, a finite size effect, where the two solutions are effectively coexisting giving a kink-link solution. This occurs due to the vicinity of the phase transition and not, as is more usual, due to coexistence of two stable states (the $\rho = 0$ state is unstable).

We used an agent-based simulation in order to study whether the inherent stochasticity of the system would alter the behaviour seen in the mean-field equation and saw that it had little effect. The strength of the noise is however difficult to tune using this method and we now turn to analyse the effect of introducing a noise term explicitly to Eq. (3.20). In the next chapter, we will see that noise can also greatly change the resulting behaviour and relate this problem to the celebrated class of phase transitions in non-equilibrium physics: Directed Percolation.

Chapter 4

Directed Percolation with Drift I: Background and Techniques

In the previous chapter, we considered a non-equilibrium phase transition that arose in the context of bacterial sedimentation, that is, F-KPP with an advection term. We were mostly interested in the effect of adding the advection whilst in the presence of no-flux boundaries. We used numerical integrations of the continuous equation, as we found these to be similar enough to the agent-based simulation to justify their use. However, the system itself is inherently stochastic and in this chapter we pursue further this line of thought: what effect will the stochasticity have if we retain it in our coarse-grained description? What form of noise should we use and will this make a difference? In this chapter and the next, we consider the following equation:

$$\frac{\partial \rho(x,t)}{\partial t} = D\frac{\partial^2 \rho}{\partial x^2} + v\frac{\partial \rho}{\partial x} + \alpha\rho(1-\rho/\rho_0) + \Gamma(\rho)\eta(x,t) \tag{4.1}$$

$\eta(x,t)$ is a random variable and, as we are interested in fluctuations in the individual birth-death processes, we will first use a multiplicative noise term where $\Gamma(\rho) \propto \sqrt{\rho}$. We note that $\rho = 0$ everywhere satisfies Eq. (4.1), and this state has $\Gamma(\rho) = 0$, meaning that the system respects the absorbing state when interpreted in the Ito sense[1]. This also means that detailed balance is violated and we are strongly out of equilibrium. This system is particularly intriguing as it

[1]In this chapter and the next, we will always choose the Ito interpretation of the noise terms in any Langevin equation, as this ensures the system will exhibit an absorbing state as explained in Section 2.3.3.

has two limiting cases of interest. The first is obtained as the magnitude of the noise is taken to zero, and is the case studied in the previous chapter. This leads us to ask whether the phase transition remains when noise is added? And if so, how does the critical behaviour change? The second limiting case is reached by taking the strength of the advection term, v, to zero: this recovers the fluctuating hydrodynamic description for Directed Percolation (DP) [Henkel 08]. DP gives arguably the most well-established universality class for non-equilibrium phase transitions, and we will study whether the resulting transition still belongs to the DP class. Furthermore, DP exhibits a continuous non-equilibrium phase transition as opposed to the sharp discontinuous frontier observed when $\Gamma = 0$ in Chapter 3. There must therefore be a point, existing somewhere between our two limiting cases, where the transition changes character. Will this point exist at one of the boundaries, or will there be a triple point existing somewhere in between?

We will answer all of these questions in Chapter 5, but first we use this chapter to review the relevant background theory. We will discuss Directed Percolation and look at how we introduce the noise and what form of $\Gamma(\rho)$ should be considered. We will also introduce a second alternative form of the noise that we will be studying both on its own merits and to see how the results differ from the first case. We then turn to the simulation techniques employed to study these equations. Simulating systems with absorbing states and multiplicative noise is not trivial and we discuss two different methods for implementing the noise, one from [Dickman 94] and a more recent one from [Dornic 05]. Finally, as we are interested in simulations near absorbing-state phase transitions, we will sometimes be looking at quasi-stationary states of diminishing lifetimes. Fluctuations can easily lead to these states being absorbed prematurely and a method from [Grassberger 02] will be presented to overcome this difficulty.

4.1 Background: Directed Percolation

DP is an archetypal non-equilibrium phase transition, which takes an active phase, where the fluctuating density is non-zero, into an absorbing one with zero density. The transition is continuous and it is non-equilibrium as the presence of the absorbing state means that detailed balance cannot be satisfied. DP gets its name from the study of percolation through porous media [Broadbent 57], where a transition occurs between a phase where the material is porous to one

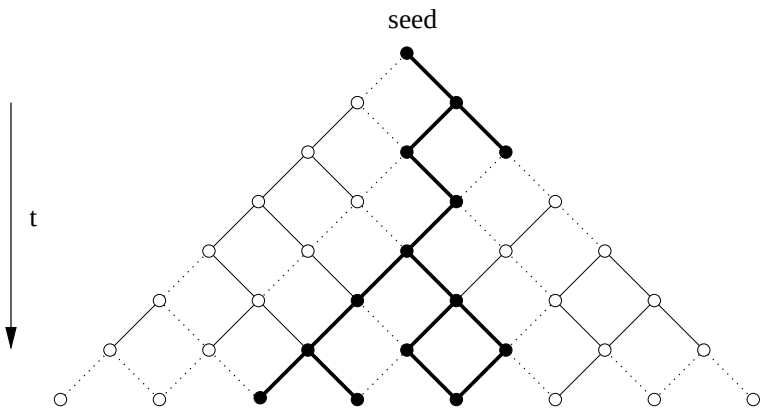

t	N(t)
0	1
1	1
2	2
3	1
4	1
5	2
6	3
7	3

Figure 4.1: Directed percolation through porous media. Dotted line are closed interstices, thin solid lines are open. Wet sites are represented by filled dots and dry sites by empty ones.

where it is essentially congested and therefore blocked. If we consider a filter, the pores can be represented by a lattice and the interstices connecting them by the lattice bonds. There will be irregularities in the network, and this is represented by a given bond being open, with probability p, or closed, with $(1-p)$. This is Percolation and Directed Percolation comes from such a system where the percolation is only allowed to occur in one direction, which is then interpreted as time. This leads to a stochastic process as illustrated in Figure 4.1.

If we label an occupied site by A and a closed one by $\emptyset$, this results in a reaction-diffusion process obeying the following reaction rules:

$$\begin{aligned} A &\rightarrow \emptyset, \\ A &\rightarrow 2A, \\ 2A &\rightarrow A. \end{aligned} \tag{4.2}$$

It turns out that many stochastic particle processes following this or similar update schemes belong to the DP class, and this offers a clue as to why DP has been so successful [Henkel 08]. Indeed, it has also been shown to correctly describe systems as diverse as chemical reaction-diffusion processes, epidemic spreading, contact processes, growing microbial populations and branching-annihilating random walks [Munoz 98].

This broadness is now expressed by the following "DP conjecture":

> All systems exhibiting a continuous transition into a unique absorbing state, characterised by a one-component order parameter, and not showing any extra symmetries or conservation laws, belong to the DP universality class [Grassberger 82].

The fact that the transition must be continuous is important as we will see in the next chapter. The continuous limit of the above reaction-diffusion process is usually described by the following Langevin equation originally derived by Janssen [Janssen 81]:

$$\frac{\partial \rho(x,t)}{\partial t} = D\frac{\partial^2 \rho}{\partial x^2} + \alpha\rho(1-\rho) + \Gamma_0\sqrt{\rho}\eta(x,t) \tag{4.3}$$

where $\eta(x,t)$ is Gaussian white noise[2]. As it is rarely explained in the literature, I have included a method to show that this Langevin equation is indeed equivalent to the microscopic model above in Appendix A.

We note finally that DP phase transitions, although extremely successful in theoretical models, have proven extremely difficult to observe in experiment, although many candidates for an experimental set-up have been proposed. This is possibly due to the difficulty in having a perfectly-absorbing state in nature [Hinrichsen 00], but a more likely cause is quenched disorder. Defects, leading to spatial or temporal inhomogeneities, will introduce disorder in the percolation rates and this can change the universality class of the resulting transition [Hinrichsen 00]. The first successful realisation of DP in experiment has now been published [Takeuchi 07, Takeuchi 09], which gives a firmer footing to the vast amount of numerical data that has been accrued over the years. Gray spots in a layer of excited nematic liquid crystals both decay and engender new spots in their vicinity, similar to a 2-dimensional contact process, and 12 different critical exponents have been measured.

4.2 Model: From F-KPP to DP

As we mentioned above, the model for bacterial sedimentation in the previous chapter is inherently stochastic; we now consider the effect of this stochasticity by explicitly adding it to our F-KPP equation with advection. This results in Eq. (4.1) leaving us only to specify the form of the noise, $\Gamma(\rho)\eta(x,t)$. $\eta(x,t)$ is

[2] A spatio-temporal Gaussian white noise refers to a noise whose mean is zero ($<\eta(x,t)>=0$) and whose 2^{nd} moment is a δ-function in space-time ($<\eta(x,t)\eta(x',t')>=\delta(x-x')\delta(t-t')$).

chosen to be Gaussian as this is the simplest form and other forms of noise on the microscopic level will converge to a macroscopic Gaussian due to the Central Limit Theorem. Only the first two moments need therefore be considered. The first moment must be zero so that the noise remains unbiased, and the second one will yield:

$$< \eta(x,t)\eta(x',t') >= f(\rho)\delta(x-x')\delta(t-t'). \tag{4.4}$$

In order to specify $f(\rho) = \Gamma^2(\rho)$, we use a Landau expansion:

$$f(\rho) = a + b\rho + c\rho^2 + ... \tag{4.5}$$

We set $a = 0$ to respect the absorbing state: if the density is zero, the noise must also be zero so that the state truly cannot be escaped. We also neglect the second order term, as we are in the neighbourhood of the absorbing state, and ρ will be small. Finally, we relabel $b = \Gamma_0^2$ giving for the multiplicative factor:

$$\Gamma(\rho) = \Gamma_0\sqrt{\rho(x,t)}. \tag{4.6}$$

For most of the results in the following chapter, we will simulate Eq. (4.1) directly. For the deterministic part, we use the same integration scheme as in Section 3.3.2 in the last chapter. Care however must be taken in the implementation of the noise, and several methods for doing this are discussed below. Different values of v and Γ_0 give greatly differing behaviour and the resulting phase diagram is the subject of the next chapter.

4.2.1 An alternative noise: $\Gamma(\rho) \propto \rho(x,t)$

As can be seen in the literature [Munoz 98], the type of noise included in these systems can greatly alter the type of transition that is observed. For this reason, it can be interesting to consider another form of noise entirely. We chose to investigate the behaviour of the system when $\Gamma(\rho) \propto \rho$. This kind of noise is often used in the context of population dynamics to represent fluctuations in a population rather than in the individual birth-death processes: if we consider the rate at which individuals die $W(n \to n-1)$ or multiply $W(n \to n+1)$ in any one time-step, then, as we take the population size, n, large and all rates are identical, we observe fluctuations of the order $\sqrt{n}$ as the noise self-

averages to form a Gaussian distribution with variance n. If, however, we consider changes in the environment, where all of the individuals become more likely to die or more likely to multiply, i.e. the rates themselves can change, then the fluctuations generate a noise proportional to the population size itself. The result is Eq. (4.1) with $\Gamma(\rho) = \Gamma_0\rho(x,t)$:

$$\frac{\partial\rho(x,t)}{\partial t} = D\frac{\partial^2\rho}{\partial x^2} + v\frac{\partial\rho}{\partial x} + \alpha\rho(1-\rho) + \Gamma_0\rho\eta(x,t). \tag{4.7}$$

Without advection ($v = 0$), this model was studied in [Munoz 98, Grinstein 96, Tu 97]. It was shown that the system can be mapped onto the Kardar-Parisi-Zhang equation (KPZ) [Kardar 86], by means of a Cole-Hopf transformation $\rho(x,t) = e^{h(x,t)}$. Using the Ito Formula Eq. (2.34) and setting the advection strength to zero gives:

$$\frac{\partial h(x,t)}{\partial t} = D\frac{\partial^2 h}{\partial x^2} + D(\frac{\partial h}{\partial x})^2 + \alpha(1-e^h) - \frac{\Gamma_0^2}{2} + \Gamma_0\eta(x,t). \tag{4.8}$$

This is exactly KPZ apart from the αe^h term, which can be shown to vanish in the steady state of either the absorbing state or at the critical point ($\rho = 0$ in both cases) [Tu 97]. As a consequence, the absorbing state phase transition at $v = 0$ is continuous, but does not belong to the DP universality class. For instance, holding Γ_0 constant and varying a close to criticality yields $\langle\rho\rangle \sim (a - a_c)^\beta$ with $\beta = 1.5$, whereas $\beta \simeq 0.28$ in DP [Dickman 94].

4.2.2 Varying α or varying Γ_0?

In the DP literature, it is more usual to see the noise strength, Γ_0, held constant and the growth, α, varied, giving the critical point as a value of the growth, $\alpha = \alpha_c$. We are, however, interested in the effect of adding the noise term to our model for bacterial sedimentation and will therefore be varying the noise. It is not immediately obvious that the two are equivalent, does varying the noise past a critical value, Γ_c, effect the same transition? We show that it does: first we vary the growth, $\alpha \to \Lambda\alpha$, and then we see the effect on the other variables, $x \to \Lambda^\mu x$, $t \to \Lambda^\nu t$, and $\rho \to \Lambda^\gamma\rho$. Inserting these into Eq. (4.3) gives:

$$\Lambda^{\gamma-\nu}\dot{\rho} = \Lambda^{\gamma-2\mu}D\rho'' + \Lambda^{\gamma+1}\alpha\rho - \Lambda^{2\gamma}\rho^2 + \Lambda^{\frac{\gamma}{2}-\frac{\nu}{2}-\frac{\mu}{2}}\Gamma_0\sqrt{\rho}\eta \tag{4.9}$$

where the dimensions of $\eta(x,t)$ are given by $\sqrt{(\mathrm{d}x)(\mathrm{d}t)}$ because of its variance: $\langle\eta(x,t)\eta(x',t')\rangle \propto \delta(x-x')\delta(t-t')$. This rearranges to give:

$$\dot{\rho} = \Lambda^{\nu-2\mu}D\rho'' + \Lambda^{\nu+1}\alpha\rho - \Lambda^{\gamma+\nu}\rho^2 + \Lambda^{\frac{\nu}{2}-\frac{\mu}{2}-\frac{\gamma}{2}}\Gamma_0\sqrt{\rho}\eta. \tag{4.10}$$

We want to assess the impact of varying α on the noise term alone and therefore choose the coefficients so that the remaining terms are unchanged. This gives $\nu = 2\mu$ for the diffusion term and $\nu = -1$, $\gamma = 1$ for the growth terms. These values restore Eq. (4.3) except with

$$\Gamma_0 \to \Lambda^{-\frac{3}{4}}\Gamma_0. \tag{4.11}$$

This means that varying the growth is indeed equivalent to varying the noise and, for example, that if $\alpha_c = 0.78$ when $\Gamma_0 = 1$ (the usual result quoted in the DP literature), then $\Gamma_c = 0.72$ when $\alpha = 0.5$. This is a useful result as for most of our simulations this will be the value of the growth that we will employ.

If we restore the advection we see that, under the same transformation, $v\rho' \to \Lambda^{\nu-\mu}v\rho' \to \Lambda^{-\frac{1}{2}}v\rho'$. Hence, two of the three parameters can be varied independently while holding the third fixed. Another way to express this is using Buckingham's π Theorem [Weisstein b], we have 3 units and 5 parameters ($\rho_0 = 1$) and hence there are $5-3=2$ dimensionless numbers in our equation. Because of our particular interest in advection and noise, we therefore choose to look at the phase diagram in the Γ_0-v parameter plane.

4.3 Simulation Techniques

The deterministic part of the equation is discretised in space and time as in Chapter 3; we now have a noise term which is discretised in the following way:

$$\Gamma(x,t) = \Gamma_0\eta(x,t)\sqrt{\rho(x,t)} \to \Gamma_0\frac{\eta_i(t)}{\sqrt{\mathrm{d}x\mathrm{d}t}}\sqrt{\rho_i(t)}. \tag{4.12}$$

In general, we will need data from configurations where the density on any one site may be small as we will often be considering systems that exhibit phase transitions into an absorbing state. The form of multiplicative noise above is proportional to the square-root of the density, and therefore, upon time discretisation the noise might induce a large negative fluctuation. This

would result in a negative density which is obviously unphysical. As we will be interested in the manner in which the density goes to zero, this is a crucial problem.

Naively, we might attempt to simply set all negative densities immediately to zero. Unfortunately, this amounts to an asymmetric truncation of the noise and results in a shift of the critical point in our system (and removal of the absorbing state entirely with DP [Dickman 94]). Another method would involve introducing a small field that repels the density away from zero, although this will remove the absorbing state altogether. A limiting procedure would then need to be introduced in which progressively smaller fields are considered eventually restoring the original problem. We chose two methods for simulating absorbing states and we present them below. They both gave the same behaviour, as shown in the next chapter, in section 5.5. Dickman's method [Dickman 94] was much easier to implement than Dornic's [Dornic 05] but the latter was found to be more efficient computationally. Typical values for time and space discretisation were $\mathrm{d}x = 0.1$ and $\mathrm{d}t = 0.001$ using Dickman's algorithm but, using Dornic's, we were able to increase these up to $\mathrm{d}x = 0.5$ and $\mathrm{d}t = 0.05$ thus significantly decreasing simulation time.

Both methods are based on the principle that the time evolution for the density can be split into two parts and each evolved separately. This can be justified as follows: solving the Langevin equation is equivalent to solving the Fokker-Planck equation $\partial_t P(\rho, x, t) = -HP$, where H is a Hamiltonian, and simulating this is in turn equivalent to evolving an initial P_0 using e^{-tH}. If we suppose that H consists of two pieces $H = H_A + H_B$ then

$$P(t+dt) = e^{-\mathrm{d}tH} P(t) = e^{-\mathrm{d}t(H_A+H_B)} P(t) \simeq e^{-\mathrm{d}tH_A} e^{-\mathrm{d}tH_B} P(t) + O(\mathrm{d}t^2) \quad (4.13)$$

where in the last step, we used Baker-Campbell-Hausdorff [Weisstein c] to split the operators. This means that, in a single timestep, $\rho(t)$ can be evolved using H_A to give $\rho^{int}(t)$, which can then be evolved using H_B to give $\rho(t + dt)$.

4.3.1 Dickman's method for simulating phase transitions into absorbing states

This method, originally proposed in [Dickman 94], attempts to solve the problem of generating negative densities in the following way: if the noise term is

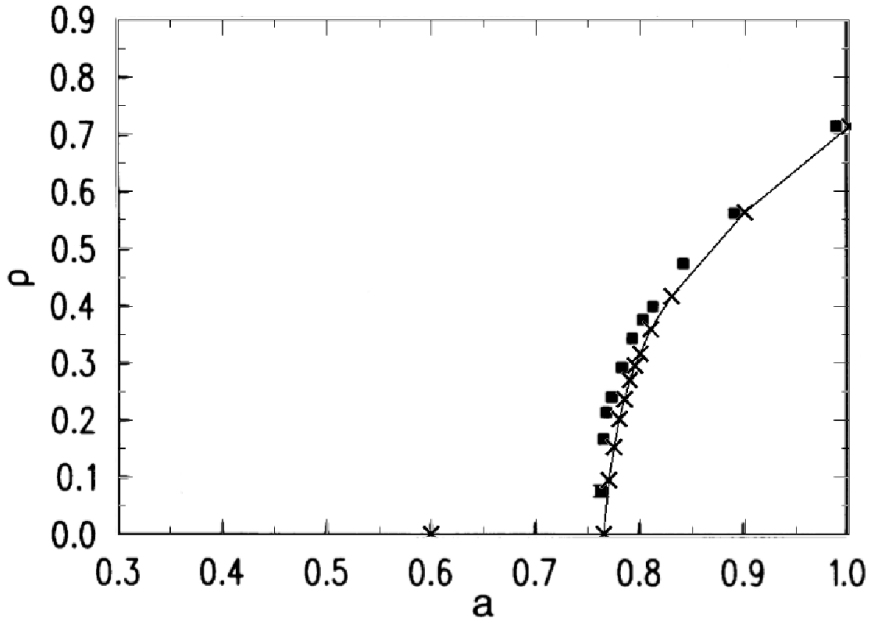

Figure 4.2: The steady state density, ρ, versus the growth rate, a, for numerical integrations of the continuous description for DP using the first method from [Dickman 94]. The squares are points from the original paper, this has been overlaid with points from our simulation (crosses). Simulation parameters are $\Gamma_0 = 1$, $D = 1$, $L = 500$, $\mathrm{d}x = 0.1$, $\mathrm{d}t = 0.001$, the growth term is modelled as $a\rho - b\rho^2$ with $b = 1$.

written as $\Gamma(x,t) = \Gamma_0 \eta(x,t)\sqrt{\rho(x,t)}$, then $|\eta|$ is limited to not exceed a chosen value η_{max}. This amounts to a symmetrical truncation of the Gaussian. In addition to this, the density is discretised $\rho_i \to n_i \rho_{min}$, and η_{max} and ρ_{min} are related by:

$$\rho_{min} = \eta_{max}^2 \Gamma_0^2 \mathrm{d}t/\mathrm{d}x. \tag{4.14}$$

This means that the largest value that can be generated by the noise at each site i is:

$$\Gamma_i^{max}(t) = \Gamma_0 \eta_i^{max}(t) \frac{\sqrt{\rho_i(t)}}{\sqrt{\mathrm{d}x\mathrm{d}t}} = \Gamma_0 \frac{\sqrt{\rho_i(t)}}{\sqrt{\mathrm{d}t\mathrm{d}x}} \sqrt{\rho_{min}(t)} \frac{\sqrt{dx}}{\Gamma_0\sqrt{dt}} = \frac{1}{\mathrm{d}t}\sqrt{\rho_i(t)\rho_{min}}. \tag{4.15}$$

Since $\rho_i(t) > \rho_{min}$, $|\Gamma_i| \leq \rho_i$ in any one $\mathrm{d}t$ and so the density can no longer become negative. The noise is constructed such that no fluctuation can exceed the smallest recorded value of the density.

Each time the density is discretised, there will be a small error at each site.

We must keep track of these errors as they accumulate, so that if it exceeds ρ_{min} at any one site, it can be re-introduced into the system. This yields the following algorithm at each time-step:

1. Evolve the discretised density using the deterministic portion of Eq. (4.1)
2. At each site: discretise the density and keep track of the accumulated error (the difference between the discretised and exact density)
3. At each site: check whether $\rho_i^{error} \geq \rho_{min}$. If this is the case, increment the discretised density and subtract ρ_{min} from ρ_i^{error}.
4. Evolve the discretised density via the noise term ensuring that $\eta \leq \eta_{max}$
5. Repeat step 2
6. Repeat step 3

This method is easy to implement but raises some fundamental questions: can we be sure that we are in fact simulating the same equation? For DP, the results are convincing, see Figure 4.2, but this does not guarantee that we are not creating any artefacts of the discretisation in our system. Another potential problem is that there will be an error on each site that has $\rho < \rho_{min}$, these sites will no longer evolve deterministically even though there is still some concentration there. To minimise this error, we need to keep ρ_{min} as close to zero as possible and this is one of the reasons that dt must remain small using this method.

We now turn to an alternative method presented in [Dornic 05]. Although more complicated, this method represents not only a significant improvement in computational efficiency over Dickman's method above, but also removes the doubts that can be raised over whether we are in fact simulating the same system after having discretised the density. Furthermore, using two distinct methods affords us more confidence that the behaviour we are observing is the true behaviour of the system in question.

4.3.2 Dornic's method for simulating phase transitions into absorbing states

This method, taken from [Dornic 05], uses the operator-splitting scheme in the following way: we split H into a noise term and a deterministic part, $H =$

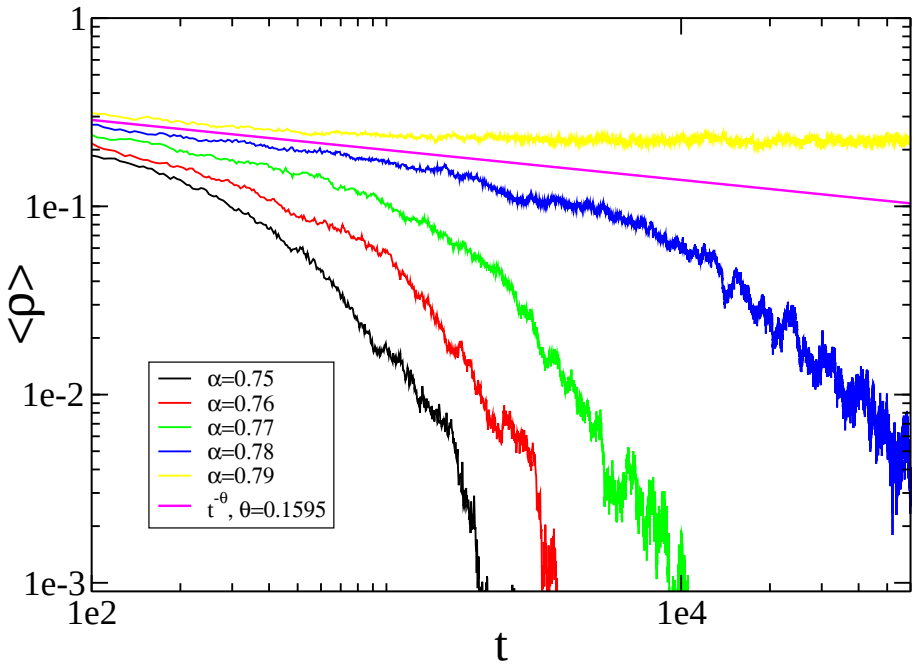

Figure 4.3: The transient density, ρ, as a function of time for $\alpha = 0.75, 0.76, 0.77, 0.78, 0.79$ using the Dornic Method. The Magenta line represents $< \rho > \propto t^{-\theta}$ at criticality with $\theta = 0.1595$ from [Dornic 05]. This confirms the presence of the critical point at 0.785 close to the value found with Dickman's method ($\alpha = 0.77$). Simulation parameters are $\Gamma_0 = 1$, $D = 1$, $L = 5000$, $\mathrm{d}x = 1$, $\mathrm{d}t = 0.1$, the growth term is modelled as $\alpha\rho - b\rho^2$ with $b = 1$.

$H_N + H_D$, and choose H_N such that an exact solution is known. We can then produce an intermediate density profile, ρ^{int}, by sampling from the probability distribution that solves $\partial_t P = -H_N P$ exactly, and finally evolve ρ^{int} using the deterministic part as before. This can almost always be done, because at worst we can choose H_N to represent the noise alone, which can usually be transformed into an equation with additive noise. For example, for the multiplicative noise used in DP, we can use $\mu = \sqrt{\rho}$, which if $\dot{\rho} = \sqrt{\rho}\eta(x,t)$, yields $\dot{\mu} = -\frac{1}{8u} + \frac{1}{2}\eta(x,t)$ using the Ito formula Eq. (2.34).

In the case of DP, however, we can do better as an exact solution for the Langevin equation without the non-linear growth part ($-\alpha\rho^2$) has been known for some time [Feller 51] and is relatively straightforward to sample. We therefore follow [Dornic 05] and space-discretise the Langevin equation, using the

centred space prescription Eq. (2.76), to yield the following single-site problem:

$$\dot{\rho_i} = a_i + b\rho_i - \alpha\rho_i^2 + \Gamma_0\sqrt{\rho_i}\eta_i(t) \tag{4.16}$$

where $a_i = \frac{D}{dx^2}(\rho_{i+1} + \rho_{i-1})$ and $b = \alpha - 2\frac{D}{\mathrm{d}x^2}$ are constants (when considering site i only). If we remove the non-linear part, this is a single-site linear Fokker-Planck equation with a known solution [Feller 51]:

$$P(\rho_i, t) = \lambda e^{-\lambda(\rho_0 e^{bt} + \rho_i)} \left[\frac{\rho_i}{\rho_0 e^{bt}}\right]^{\frac{\mu}{2}} I_\mu(2\lambda\sqrt{\rho_0\rho_i e^{bt}}) \tag{4.17}$$

where $\lambda = \frac{2b}{\Gamma_0^2(e^{bt}-1)}$, $\mu = -1 + \frac{2a}{\Gamma_0^2}$, and I_μ is the Modified Bessel function of order μ.

To sample this probability distribution, we use the Taylor expansion of $I_\mu(x)$ [Weisstein a]:

$$I_\mu(x) = \left(\frac{x}{2}\right)^\mu \sum_{n=0}^{\infty} \frac{(x/2)^{2n}}{n!\Gamma(\mu + n + 1)} \tag{4.18}$$

where $\Gamma(x)$ is the gamma function. After re-arranging, this gives:

$$\begin{aligned} P(\rho, t) &= \textstyle\sum_{n=0}^{\infty} \frac{(\lambda\rho_0 e^{bt})^n e^{-\lambda\rho_0 e^{bt}}}{n!} \frac{\lambda e^{-\lambda\rho}(\lambda\rho)^{n+\mu}}{\Gamma(n+\mu+1)} \\ &= \textstyle\sum_{n=0}^{\infty} W(n) f_n(\rho) \end{aligned} \tag{4.19}$$

where $f_n(\rho)$ is a Gamma distribution for ρ and all of the $W(n)$ are positive real numbers and hence correspond to the weights of the $f_n(\rho)$ that make up $P(\rho, t)$. $W(n)$ is in fact a Poisson distribution of n with parameter $\lambda\rho_0 e^{bt}$ and therefore can be sampled as a probability distribution in its own right. We can therefore sample $P(\rho, t)$ by first choosing n from the available weights and then taking a ρ from $f_n(\rho)$. This results in a 3-step procedure to generate ρ^{int} from $\rho_0 = \rho(t)$:

1. Use $\rho_0 = \rho(t)$ to calculate the Poisson parameter $\lambda\rho_0 e^{bt}$.
2. Sample the associated Poisson distribution in order to generate n.
3. Pick a Gamma distributed ρ^{int} from $f_n(\rho)$.

Both the Poisson and Gamma distributions are sampled using rejection methods from [Press 92]. Once we have ρ^{int}, we can then evolve it deterministically to give $\rho(t+dt)$. To summarise, at each time-step, we evolve $\rho(t)$ via the following steps:

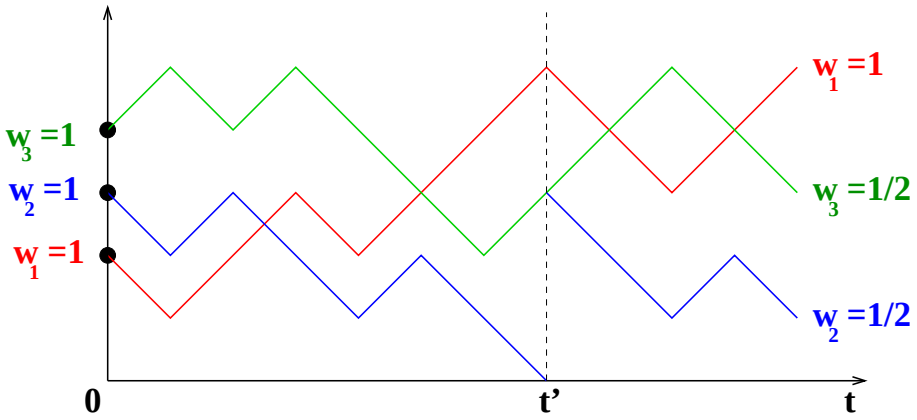

Figure 4.4: The PERM method for simulating quasi-stationary states: three simulations are run in parallel. The blue run falls into the absorbing state at $t = t'$ and the green one is then 'cloned' to maintain 3 runs in total, all non-absorbed. The corresponding weights are halved in order to produce the correct averages when the simulation is finished.

1. Generate ρ^{int} by sampling from Eq. (4.17) using $\rho_0 = \rho(t)$ (using the above 3-step procedure)

2. Evolve ρ^{int} using $\dot{\rho} = -\alpha\rho^2$

For details of how to sample probability distributions in general and Poisson and Gamma distributions in particular, see [Press 92].

4.3.3 PERM method for simulating quasi-stationary states

Another difficulty that arose was due to the presence of metastable states. For example, in Chapter 5, we study a dynamical transition between a long-lived metastable state and an unstable state. Both of these states are always absorbed at long times and it becomes more and more likely that a fluctuation can occur that 'kills' the system as the dynamical transition is approached. This makes pinpointing the critical point separating the two regimes very difficult. In order to simulate the quasi-stationary states, we used the 'Pruning and Enrichment Rosenbluth Method' (PERM) reviewed in [Grassberger 02].

The simulation starts with N independent versions of the same system evolving in parallel each with weight $w_i = 1$. If one of the 'clones', j, is absorbed, the following process occurs:

1. Choose one of the remaining clones, k, with probability $\frac{w_k}{\sum_k w_k}$.

2. Set j to be a reproduction of k, i.e. $\rho_i^{(j)} = \rho_i^{(k)} \forall i$.

3. The weights for both j and k are halved: $w_{j,k} \to w_{j,k}/2$.

4. If $W = \sum_i w_i < 1$, then enrich all of the weights $w_i \to N w_i / W$.

The last step is taken to ensure that the weights do not become too small if the system is repeatedly reaching the absorbing state. As we will see in Chapter 5, as the dynamical transition is approached, there will be many cloning events even when we are definitely simulating a system on the metastable side of the line, and without this step $W \to 0$ very quickly. In every step that the weights are enriched, t_i, the enrichment value $N/W(t_i)$ is stored. The resulting quasi-stationary distribution is the average over all of the clones, taking the relative weights into account:

$$\rho_i^{\text{quasi}} = \frac{1}{N} \sum_j w_j \rho_i^{(j)} \prod_k \frac{N^k}{W(t_k)}. \tag{4.20}$$

4.3.4 Boundary Conditions

We want to implement no-flux boundary conditions Eq. (3.21) at both ends of the 'container' and this can be done in a number of ways because the derivative can be discretised in more than one way, all of which give the same result in the continuous limit. If we simply discretise the derivative as we did in the previous chapter, Eq. (3.29), we find that this choice leads to mass 'leaking' out of the bottom of the container. This did not cause a problem for bacterial sedimentation because we were interested in the transition between an exponential and growth phase: the system always retained a finite mass. However, in this and the next chapter, we consider transitions into absorbing states, and the error is likely to shift the position of the absorbing state. We therefore use a different prescription here: we note that, in the absence of growth, the system obeys Fick's law: $\dot{\rho}_i = \nabla J_i$, where J_i is the flux. Using the same three-point derivative as in the bulk, we have $\nabla J_i = \frac{J_{i,i+1} - J_{i-1,i}}{2\mathrm{d}x}$ and can therefore define the flux:

$$J_{i,j} = \frac{D}{\mathrm{d}x}(\rho_j - \rho_i) + v(\rho_j + \rho_i) \qquad j = i \pm 1. \tag{4.21}$$

No-flux at the boundary means, in the case of the bottom boundary at $i = 0$, $J_{1,2} = 0$, and hence:

$$\rho_1 = \left(\frac{D + \frac{v\mathrm{d}x}{2}}{D - \frac{v\mathrm{d}x}{2}} \right) \rho_2. \tag{4.22}$$

It should be noted that we re-checked the results of the last chapter with this more correct boundary condition and found the difference to be negligible.

In the following chapter, we present the results of our study on the behaviour of Eq. (4.1) with both forms of noise discussed above.

Chapter 5

Directed Percolation with Drift II: Results

In this chapter, we will analyse in detail the behaviour of Eq. (5.1):

$$\frac{\partial \rho(x,t)}{\partial t} = D\frac{\partial^2 \rho}{\partial x^2} + v\frac{\partial \rho}{\partial x} + \alpha\rho(1-\rho/\rho_0) + \Gamma(\rho)\eta(x,t), \tag{5.1}$$

where D is the diffusion coefficient, v is a drift velocity, α a growth rate, ρ_0 is the saturation density (usually set to unity) and $\eta(x,t)$ is Gaussian white noise scaled by $\Gamma(\rho)$. We will study both the case where the fluctuations are of order $\sqrt{\rho}$, due to individual birth/death events, and using linear noise of order ρ, as can be seen when there are random changes in the environment that affect the whole population[1]. We are interested in the region between the two limiting scenarios: $\Gamma_0 \to 0$ represents bacterial sedimentation, studied in Chapter 3, where we observe a discontinuous transition between an exponential profile to a growth phase, largely constant throughout the system. The other case, when $v \to 0$ (and $\Gamma(\rho) \propto \sqrt{\rho}$), admits the celebrated Directed Percolation (DP) transition into an absorbing state introduced in Chapter 4.

Using the simulation techniques described in the previous chapter, we first map out the phase diagram in the $v - \Gamma_0$ plane and find that there are now two distinct low-density phases, at large v, separated by a dynamical transition. This is reminiscent of a spinodal transition [Jones 02], as it is the limit of the

[1]This kind of noise is sometimes called "multiplicative" in the literature [Munoz 98], but we prefer to use this terminology here to describe generic dependence of the noise on the density.

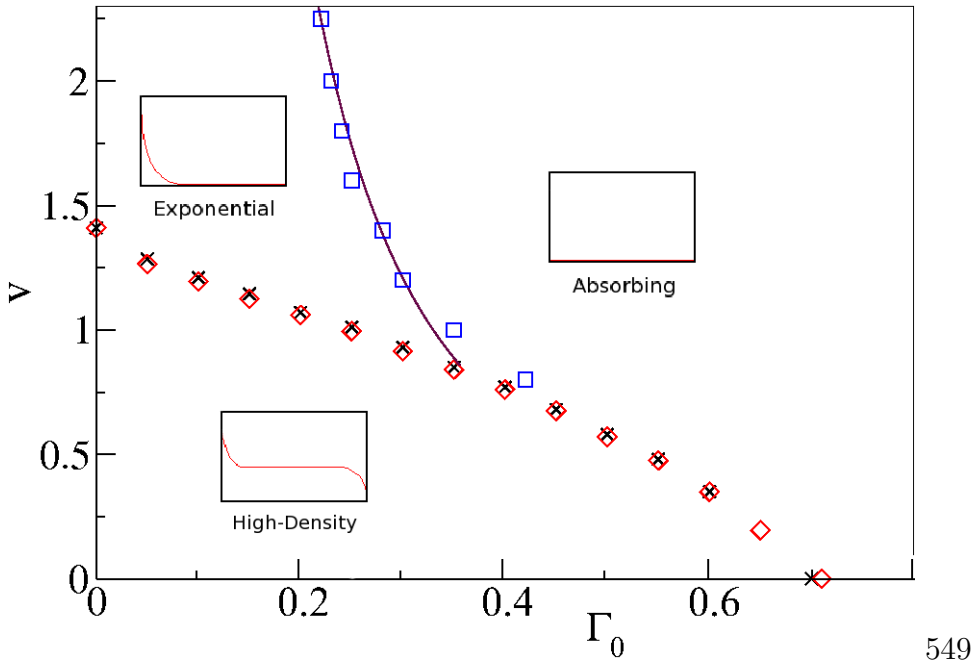

Figure 5.1: Phase boundary for $a = 0.5$ and $\eta \propto \sqrt{\rho}$. The critical points found via the Dickman and Dornic *et al.* algorithms are shown as black crosses and red diamonds, respectively. Both methods agree up to an accuracy of about 1%. The solid maroon line corresponds to the theoretical prediction (see below) for the spinodal line whereas the blue squares correspond to its numerical counterpart (see below).

metastability of the low-density phase, past which, as the noise is increased, the system becomes unstable. We will discuss the nature of the three types of transitions observed for this system and use a zero-dimensional approximation to justify and locate the dynamical transition. Finally, we will compare the behaviour in this phase diagram with the same system in the linear noise case. We find that it is different in several important ways, highlighting once again [Munoz 98] that care should be exercised when deriving fluctuating hydrodynamic equations for non-equilibrium models, as the very form of the noise, which is sometimes overlooked, may drive unexpected changes in the physics of the system.

5.1 Phase Diagram

The phase diagram in the $\Gamma_0 - v$ parameter plane is presented in Figure 5.1. A full line of critical points $v = v_c(\Gamma_0)$ links the two limiting cases of DP ($v = 0$)

and F-KPP with advection ($\Gamma_0 = 0$). For small Γ_0 and v, we observe a high-density phase, where the total mass M of the system is extensive with system size, this is the 'growth regime' from Chapter 3. Whereas before we only had only one low-density phase, the 'sedimentation regime', we now find that there are two low-density regions: the exponential profile and the absorbing state. In both of these regions, $M/L \to 0$ as $L \to \infty$, and together they constitute the rest of the phase diagram. We should note that the low-density phases are always absorbed in the $t \to \infty$ limit. Finally, the absorbing state, accessed via fluctuations, is favoured by larger values of Γ_0 and, as a consequence, the critical velocity $v_c(\Gamma_0)$, above which the high density phase is not observed, is a decreasing function of noise strength.

5.1.1 Two low-density Regimes

As mentioned above, long time simulations of the system show that its dynamical behaviour in the low-density phase is not uniform. The exponential phase, observed in F-KPP with advection, is long-lived for small Γ_0 and we refer to this regime as the 'low noise' case. While holding the velocity fixed, increasing Γ_0 has the effect of decreasing the average lifetime of the exponential state, until we can barely see it; this is the beginning of the 'strong noise' case. As we shall see, this threshold of Γ_0 corresponds to a (non-equilibrium) spinodal line which separates the two dynamical regimes (See Figure 5.1).

5.2 Low Noise Regime

The low noise regime is characterised by being similar to the $\Gamma = 0$ case presented in Chapter 3. It does however differ in several important ways detailed below.

5.2.1 Discontinuous Phase Transition

In order to identify the critical points we define the order parameter $m = M/L$, where $M = \int_0^L \rho \mathrm{d}x$ is the total mass in the system. We compute the average of m in the quasi-stationary state, the steady state of the probability distribution conditioned on survival, over a number of different simulations. We then plot this average as a function of v, for fixed Γ_0. The quasi-stationary state in the low noise regime is so long-lived that in practice we do not even need to implement the PERM method explained in Chapter 4. As we approach the

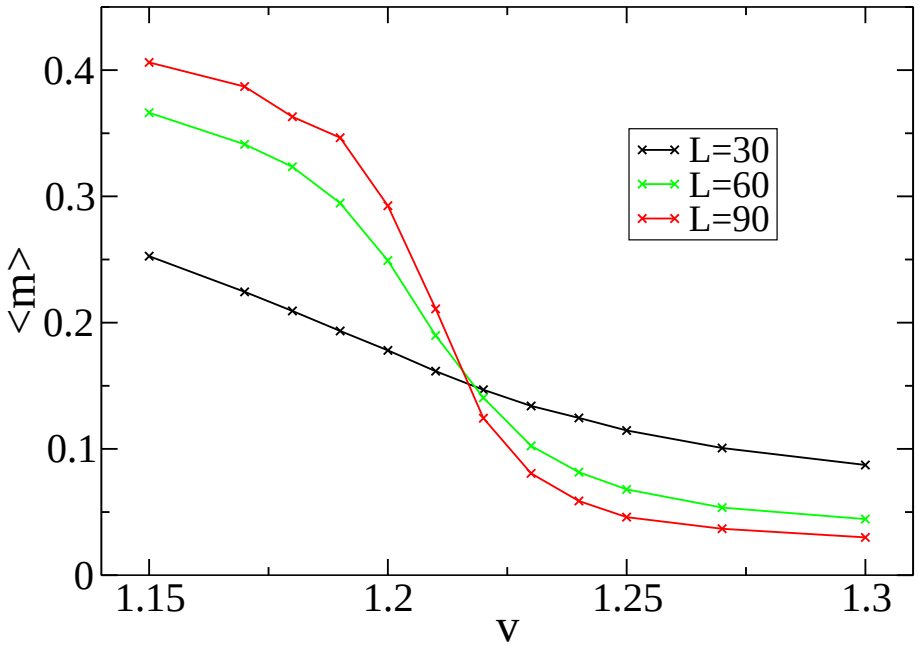

Figure 5.2: Plots of the average order parameter $\langle m \rangle$ as a function of v, for $\Gamma_0 = 0.10$ and for three different system sizes (see legend), where L is given in simulation spatial units. The presence of a stable crossing point of the order parameter curves indicates that the transition is discontinuous.

spinodal transition (see below) however, more care must be taken.

For finite systems, the crossover between low- and high-density phases sharpens when the system size is increased, but the order parameter curves intersect at a well-defined non-zero value of v (see Figure 5.2), which we take as the critical velocity v_c. The presence of a stable crossing point is indicative of a discontinuous transition: in the thermodynamic limit, as $v \nearrow v_c$ the density in the steady state approaches a non-zero value, whereas for $v \searrow v_c$ it is strictly zero. Thus, for all non-zero values of v, there will be a discontinuous "jump" at the transition point. The system thus no longer belongs to the DP universality class.

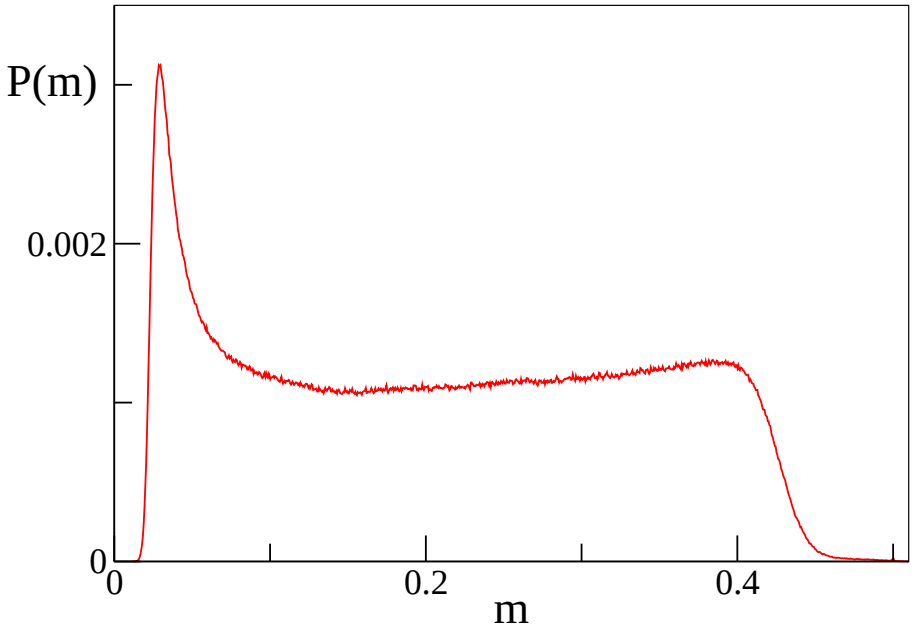

Figure 5.3: Probability distribution of the order parameter, $\langle m \rangle$, for $v = v_c \simeq 1.21$ and $L = 100$

5.2.2 Banding Region

Whereas the nature of the transition differs from that of DP, it is also different from the one of the noiseless case ($\Gamma_0 = 0$) discussed in Chapter 3. In the absence of noise, a band structure is formed at criticality and a stationary front separates high- and low-density regions in the steady state. In the noisy case considered here, the transition is in general different. Even the low noise regime, while still bearing some resemblance to the noiseless case, shows qualitatively distinct behaviour. This can be appreciated by looking at the quasi-stationary probability distribution of the average density of the system at criticality, which is shown in Figure 5.3. This distribution is composed of an approximately flat part coexisting with a peak close to zero. The physical interpretation is that in the low noise regime, the band is still present but the front, no longer stationary, now performs a random walk and occasionally gets stuck in the exponential profile. We checked numerically that the roaming band indeed performs a random walk by measuring the variance of the order parameter as

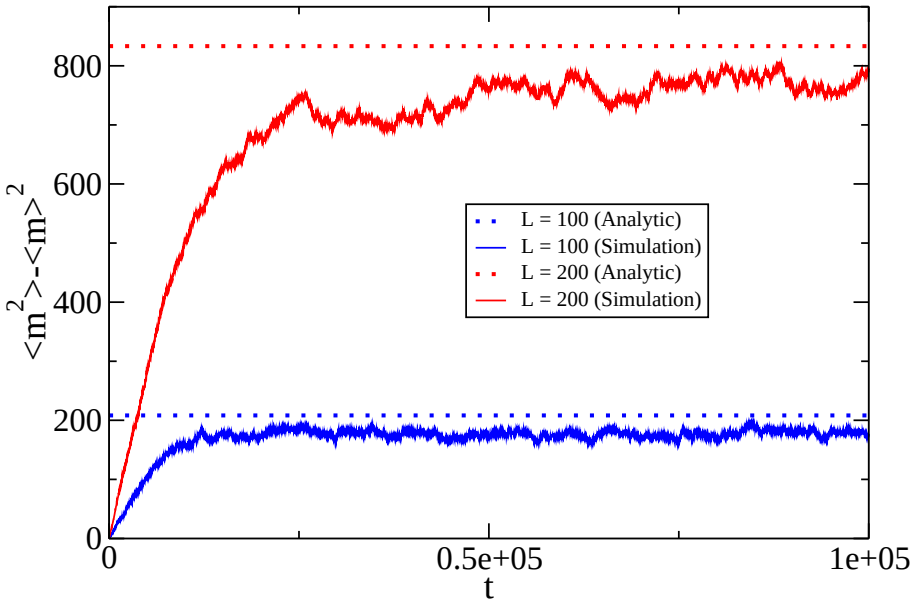

Figure 5.4: Variance of the order parameter, $\langle m^2 \rangle - \langle m \rangle^2$, for $v = v_c \simeq 1.21$ and $L = 100$ (blue) and $L = 200$ (red). Simulation (solid lines) are compared with theoretical prediction (dotted lines).

a function of time. If we approximate the probability distribution as being flat $P(m) = \frac{2}{L}$ (as $\alpha = \frac{1}{2}$), then we expect the variance to reach:

$$\langle m^2 \rangle - \langle m \rangle^2 = \int_0^{\frac{L}{2}} m^2 P(m) \mathrm{d}m - \left(\int_0^{\frac{L}{2}} m P(m) \mathrm{d}m \right)^2 = \frac{L^2}{12} - \frac{L^2}{16} = \frac{L^2}{48}. \quad (5.2)$$

In Figure 5.4, we see that the variance indeed approaches this analytical limit with an L-dependent linear slope, the L^2 dependence is respected and there is a slight discrepancy from the theoretical value, presumably due to the fact that the probability distribution is not in reality entirely flat, it rises slightly with m possibly due to the vicinity of the boundary, and then slopes off at the top.

In equilibrium statistical mechanics, the order parameter distribution is linked to the shape of the free energy, and in the case of a standard discontinuous transition, close to criticality, there would be two coexisting free energy minima resulting in two peaks in the probability distribution of the order parameter. In our case however, we have coexistence between one peak corresponding to the exponential profile and a flat piece in which all values of the total mass

are essentially equally probable. The latter piece of the distribution corresponds to the high-density phase, in which the average of the order parameter scales with the system size.

5.3 Strong Noise Regime

The transition into the low-density, strong noise regime is quite different and, as might be expected, is reminiscent of what happens in DP. In this regime, there is no longer any front, or band structure, due to the large fluctuations, and the system now uniformly collapses into the absorbing state.

5.3.1 Still a Discontinuous Phase Transition

The numerics in this region are more difficult. Since we are working with finite size systems, when $v \lesssim v_c$ the system is occasionally absorbed, even though it properly belongs to the high-density phase. To overcome this difficulty, we use PERM described in the previous chapter for simulating the quasi-stationary state. Despite the apparent similarity with DP, the transition is still discontinuous, as can be seen in Figure 5.5. However, the order parameter distribution at criticality also differs from the low noise case (Figure 5.6). The peak corresponding to the exponential phase has disappeared and the flat part in the distribution is now replaced by a broad peak at a finite value. For completeness, the quasi-stationary distribution, obtained using PERM, should be complemented by a delta function at $\langle\rho\rangle = 0$. Therefore this case is closer to a standard discontinuous transition, with two competing peaks at criticality. Note again that in the low density phase, only the delta function survives in the long-time limit.

5.4 Non-equilibrium Spinodal Line

The frontier between the low and strong noise regimes can be probed via the dynamical stability of the exponential phase. To do so, we study the evolution of the total mass in the system $M(t) = \int_0^L \rho(x,t)dx$, obtained by integrating Eq. (4.1) with $\Gamma(\rho) = \Gamma_0\sqrt{\rho}$:

$$\dot{M} = aM - b\int_0^L \rho^2(x,t)\mathrm{d}x + \Gamma_0\int_0^L \sqrt{\rho(x,t)}\eta(x,t)\mathrm{d}x. \tag{5.3}$$

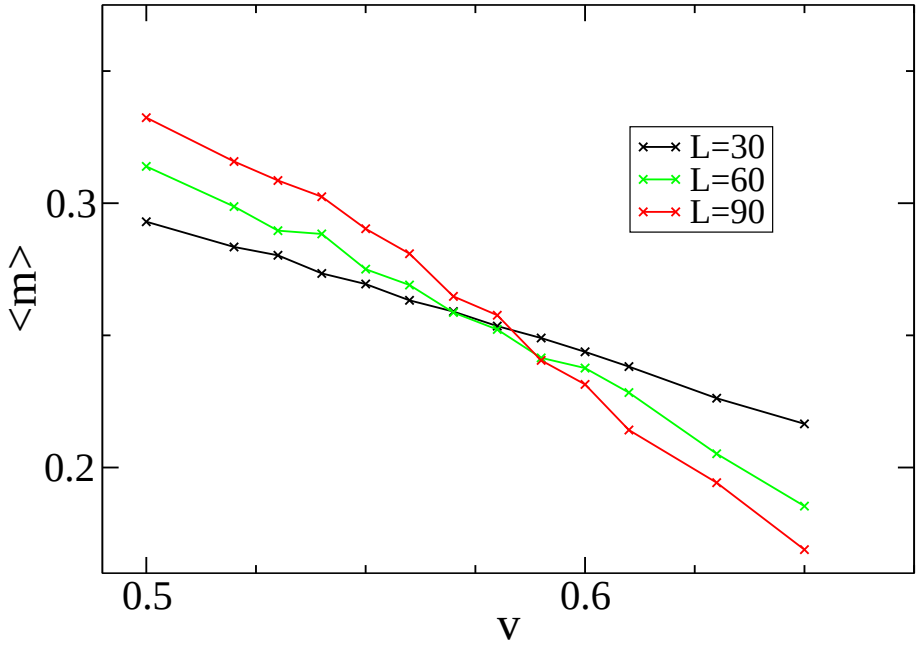

Figure 5.5: Plots of the average order parameter $\langle m \rangle$ as a function of v, for $\Gamma_0 = 0.50$ and for three different system sizes (see legend). The presence of a stable crossing point of the order parameter curves indicates that the transition is discontinuous.

The diffusion and advection terms have dropped out due to the boundary conditions:

$$\int_0^L (D\frac{\partial^2 \rho}{\partial x^2} + v\frac{\partial \rho}{\partial x})\mathrm{d}x = (D\frac{\partial \rho}{\partial x} + v\rho)\Big|_{x=0,L} = 0. \tag{5.4}$$

We approximate this by the following simplified Langevin equation[2]:

$$\dot{M} = aM - \beta M^2 + \Gamma_0 \sqrt{M}\tilde{\eta}(t) \tag{5.5}$$

where $\tilde{\eta}(t)$ is Gaussian white noise of unit variance. Both noise terms in (5.3) and (5.5) are equivalent as they are Gaussian and have the same mean and variance. The term $-\beta M^2$ is an approximation; we know from (5.3) that there must be saturation terms in the effective dynamics of $M(t)$, and retain only

[2]A similar approximation was used by Munoz in [Munoz 98]

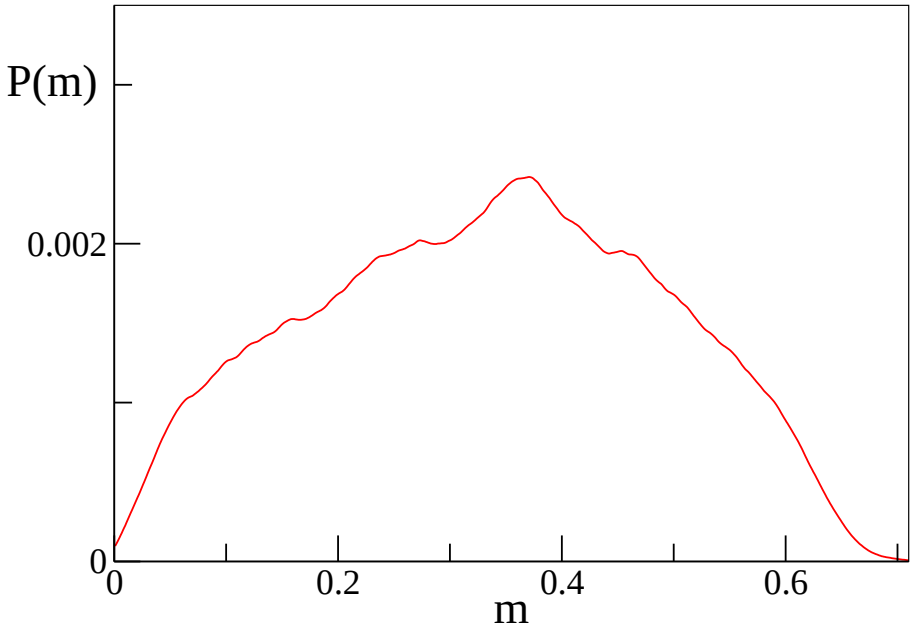

Figure 5.6: Probability distribution of the order parameter, $\langle m \rangle$, for $v = v_c \simeq 0.58$ and $L = 100$

the lowest order in M. We believe this approximation to be reasonable as we only consider the low-density regime, and hence small mass. In the high-density phase, the mass would be extensive with the system size and the approximation would break down. The parameter β contains the dependence on v and b but its form is not known exactly.

The dynamical stability of the exponential is not easily studied from Eq. (5.5) as the noise is multiplicative. We therefore recast it into an additive Langevin equation via the following change of variable $u(t) = 2\sqrt{M(t)}/\Gamma_0$. Using the Ito formula Eq. (2.34) again, Eq. (5.5) becomes

$$\dot{u} = \frac{au}{2} - \frac{\beta\Gamma_0^2 u^3}{8} - \frac{1}{2u} + \tilde{\eta}(t). \tag{5.6}$$

For its explanatory power, we will write this as:

$$\dot{u} = -\partial_u V_{\text{eff}}(u) + \tilde{\eta}; \quad V_{\text{eff}}(u) = -\frac{au^2}{4} + \frac{\beta\Gamma^2 u^4}{32} + \frac{\log u}{2}. \tag{5.7}$$

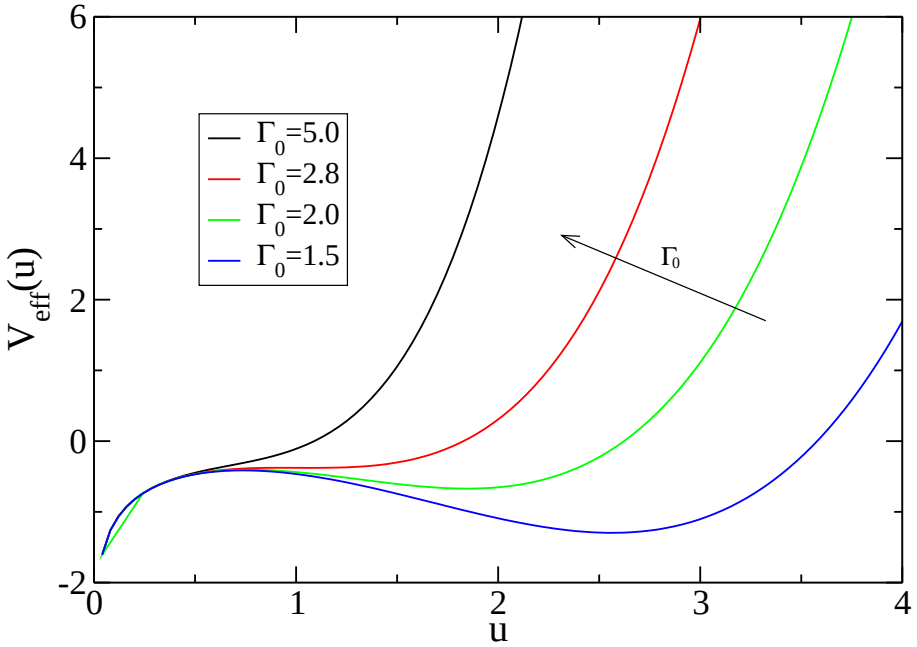

Figure 5.7: Plot of the effective potential for $\Gamma \propto \sqrt{\rho}$, $a = 2$, $\beta = 0.5$. From top to bottom, we used $\Gamma_0 = 5.0$; 2.8; 2.0; 1.5 while $\Gamma_c = 2\sqrt{2}$.

The problem is now reduced to the diffusion of a particle in a potential V_{eff}. A steady-state solution is thus given by $P(u) \propto \exp[-2V_{\text{eff}}(u)]$. One notes however that $P(u) \sim u^{-1}$ when $u \to 0$. The potential is thus not normalizable, which simply highlights that the low-density phases are always absorbed as $t \to \infty$, i.e. the only normalizable steady-state solution is $P(M) = \delta(M)$. The shape of V_{eff} nevertheless contains relevant information for the dynamics, as illustrated in Figure 5.7. When $\Gamma_0 < \Gamma_c = \frac{a}{\sqrt{\beta}}$, the effective potential has a local minimum corresponding to a potential well for positive M. The well lies above the global minimum at $M = 0$ and corresponds to a metastable phase with finite mass: the exponential phase. Conversely, for $\Gamma_0 > \Gamma_c$ there is no metastable state and the system falls directly into the absorbing state. Γ_c thus corresponds to a spinodal point at which the exponential phase turns from metastable to unstable. To construct the spinodal line $\Gamma_c(v)$ from the 0D model, we try to relate β to v (the dependence on b is not relevant since b is constant throughout our study). To do so, we compare the mean time, τ, taken to reach the absorbing state for both the system and its 0D approximation. For the 0D model, this mean

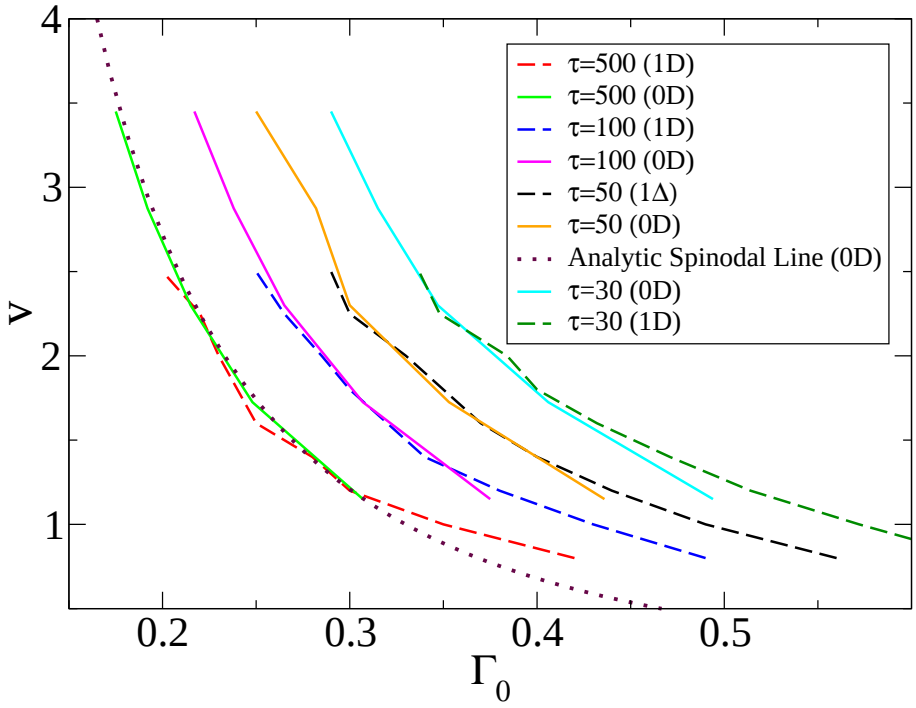

Figure 5.8: Contour lines in the (v, Γ_0) plane for which τ equals, from left to right, 500, 100, 50 and 30. In order to plot the contour lines of the 0D model, we use $\beta = 2.3\, v$ (see the main text). The analytical prediction for the spinodal line is also plotted, and closely matches the curves for which $\tau = 500$.

first-passage problem can be solved exactly up to a numerical integration, and we use this as a check in Section 5.5 below.

We compute numerically a set of contour lines for τ in the planes (v, Γ_0) and (β, Γ_0), corresponding to the 1D and 0D systems respectively (see Figure 5.8). Strikingly, simply setting $\beta \simeq 2.3\ v$ suffices to make the two sets of contour lines overlap. This strongly supports the validity of the 0D model and hence validates our interpretation of the frontier between low and strong noise regimes as a dynamical phase transition. We see in Figure 5.8 that the theoretical prediction for the spinodal line corresponds to a mean first passage time (MFPT) to absorption of $\tau = 500$. In simulations, we indeed observe long-lived exponential profiles when the MFPT to absorption is larger than 500 whereas they are barely seen otherwise. The simulation data corresponding to $\tau = 500$ was thus used to pinpoint the spinodal on Figure 5.1.

5.5 Simulation checks

In order to further enhance the validity of the simulation and thus in turn the observed behaviour, we used an entirely different method to simulate the 1D problem. The method due to Dornic et al., introduced in the previous chapter, represents a more difficult but much more efficient method for simulating DP. In order to implement the advection term, we simply add it to the final step, i.e. when evolving ρ^{int} deterministically, we add $+v\frac{\partial \rho}{\partial x}$. We find the critical points in a different way here, using a method much like the one shown in Figure 4.3. We begin with a large $\mathrm{d}x$ and $\mathrm{d}t$, and pinpoint the critical point for a given value of v. We then decrease $\mathrm{d}t$ until this critical point ceases changing. Finally, we decrease $\mathrm{d}x$ and repeat the previous analysis until we find the maximum $\mathrm{d}x, \mathrm{d}t$ for an accurate measurement of the critical point. This serves as a starting point for finding further values of Γ_c for different v. The results are basically the same, agreeing up to an accuracy of about 1%, as can be seen in Figure 5.1.

We also thought it sensible to check the MFPT to extinction found when simulating the 0D model. To do this, we use the definition of $\tau = T_1$ in Eq. (2.58). We show below how this can be calculated when only the Langevin, or indeed the FFPE, is known. We then use the result for our problem and briefly detail the simple Monte Carlo integration technique we used to obtain a result. Finally, Figure 5.9 shows that the MFPT when simulating the 0D model numerically agrees well with the theoretical prediction.

5.5.1 Computing the mean time to extinction

We consider a stochastic process whose probability distribution $P(x,t|z,t_0)$ obeys a Backwards Fokker-Planck Equation (BFPE) of the following form:

$$\frac{\partial}{\partial t}P(x,t|z,t_0) = f(z)\frac{\partial}{\partial z}P(x,t|z,t_0) + \frac{g^2(z)}{2}\frac{\partial^2}{\partial z^2}P(x,t|z,t_0). \tag{5.8}$$

We want to find τ, the mean time to extinction, defined by:

$$\tau = \int_0^\infty tQ(z,t)\mathrm{d}t \tag{5.9}$$

where $Q = Q(z,t)$ is the probability distribution that the system reaches the absorbing state at time t starting at z (See Section 2.3.6 for a more detailed

explanation). $Q(z,t)$ will then also obey the same BFPE and hence, by considering $\int_0^\infty t\partial_t Q \mathrm{d}t$, integrating by parts and using Eqs. (5.8) and (5.9):

$$f(z)\tau'(z) + d(z)\tau''(z) = -T_0 = -1 \tag{5.10}$$

where $d(z) = g^2(z)/2$ and $T_0 = \int_0^\infty Q(z,t)\mathrm{d}t = 1$. The boundary conditions are $\tau(0) = 0$, $\tau(\infty) = C$. We solve this using standard Green's function methods; We seek the Green's function $G(z,z')$, which will obey:

$$d(z)\frac{\partial^2 G}{\partial z^2} + f(z)\frac{\partial G}{\partial z} = \delta(z - z'). \tag{5.11}$$

At $z = z'$, $G(z,z') = G_1(z,z') + G_2(z,z')$ where G_1 obeys the boundary at infinity and G_2 obeys the condition at the origin. Therefore, using Eq. (5.11), we can write

$$G_1(z,z') = A(z'). \tag{5.12}$$

For G_2, we use the integrating factor:

$$W(z) = \exp \int^z \frac{f(z')}{d(z')}\mathrm{d}z' \tag{5.13}$$

so that, by construction:

$$\frac{\mathrm{d}}{\mathrm{d}z}\left\{\frac{\partial G}{\partial z}W(z)\right\} = 0. \tag{5.14}$$

Integrating gives $\frac{\partial G}{\partial z}W(z) = B(z')$ and so:

$$G_2(z,z') = \int_0^z \frac{B(z')}{W(z'')}\mathrm{d}z''. \tag{5.15}$$

This obeys the boundary condition $G_2(0,z') = 0$. Now we have two conditions at $z = z'$: G is continuous (i.e. $G_1(z',z') + G_2(z',z') = 0$), and $\frac{\mathrm{d}G}{\mathrm{d}z}$ is discontinuous by 1. the latter gives:

$$\left(\frac{\mathrm{d}G_1}{\mathrm{d}z} + \frac{\mathrm{d}G_2}{\mathrm{d}z}\right)\Bigg|_{z=z'} = 1 = \frac{B(z')}{W(z')} \tag{5.16}$$

implying $B(z) = W(z)$. The continuity of G therefore allows us to write:

$$A(z') = -W(z') \int_0^{z'} \frac{1}{W(z'')} \mathrm{d}z''. \tag{5.17}$$

This gives for the Green's Function:

$$G(z, z') = W(z') \left\{ \int_0^{z} \frac{1}{W(z'')} \mathrm{d}z'' \theta(z' - z) - \int_0^{z'} \frac{1}{W(z'')} \mathrm{d}z'' \theta(z - z') \right\}. \tag{5.18}$$

Finally, this gives for the particular integral of Eq. (5.10):

$$\tau(z) = \int_0^{\infty} -\frac{G(z, z')}{d(z')} \mathrm{d}z' \tag{5.19}$$

$$= \int_0^{z} \frac{W(z')}{d(z')} \int_o^{z'} \frac{1}{W(z'')} \mathrm{d}z'' \mathrm{d}z' - \int_z^{\infty} \frac{W(z')}{d(z')} \mathrm{d}z' \int_0^{z} \frac{1}{W(z'')} \mathrm{d}z''. \tag{5.20}$$

5.5.2 Monte Carlo integration

First, we apply Eq. (5.20) to our model. We have $f(z) = az - \beta z^2$ and $d(z) = \Gamma_0^2/2$, giving:

$$W(z) = \exp\left(\frac{2az - \beta z^2}{\Gamma_0^2} \right). \tag{5.21}$$

Inserting this into Eq. (5.20), we seek to integrate:

$$\tau(z) = \int_0^{z} \frac{2}{\Gamma_0^2 z'} \exp\left(\frac{2az' - \beta z'^2}{\Gamma_0^2} \right) \int_0^{z'} \exp\left(\frac{-2az'' + \beta z''^2}{\Gamma_0^2} \right) \mathrm{d}z'' \mathrm{d}z' \tag{5.22}$$

$$- \int_z^{\infty} \frac{2}{\Gamma_0^2 z'} \exp\left(\frac{2az' - \beta z'^2}{\Gamma_0^2} \right) \mathrm{d}z' \int_0^{z} \exp\left(\frac{-2az'' + \beta z''^2}{\Gamma_0^2} \right) \mathrm{d}z''. \tag{5.23}$$

Evaluating these integrals is simple using a standard Monte Carlo integration scheme: we draw N random numbers flatly distributed over the region of interest, here $z' \in [0, z]$, we evaluate the integrand, $I(z')$, with this value of z', and sum all of these results together. The integral is then given by the average value of the integrand multiplied by the region size, i.e. $\sum_{z'} \frac{I(z')}{N} z$. The integrals on the first line Eq. (5.22) are treated separately to those on the second line Eq. (5.23). For Eq. (5.22), we are effectively performing a double integral, we must

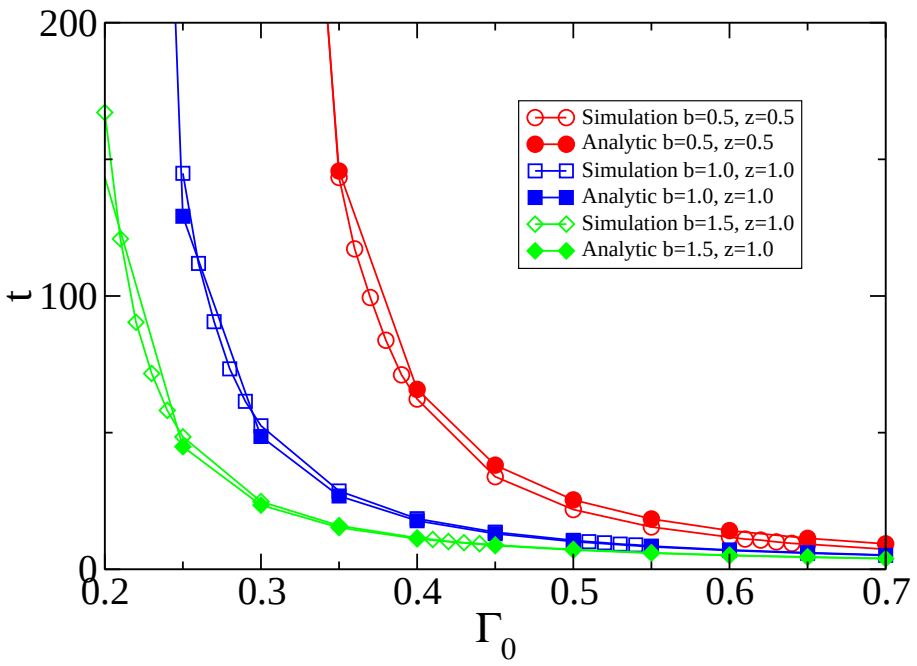

Figure 5.9: Measurements of the mean first-passage time to extinction for the 0D model. Simulations of Eq. (5.5) are compared with analytic results from Eq. (5.20), $\alpha = 0.5$ remains fixed while Γ_0 is varied with fixed b. Curves for b=0.5 (red circles), 1.0 (blue squares), and 1.5 (green diamonds) are shown. Filled symbols indicate the result of the integration and hollow symbols are simulation results. The good agreement between the two curves supports the validity of the 0D simulations.

first integrate all of the z'' from 0 to z' and then integrate over all z' from 0 to z. In practice, we draw 2 random numbers, one to represent z'' and one for z'. If $z'' < z'$, the two integrands are evaluated, multiplied together, and added to the running total. If not, nothing happens. Once this has been repeated N times, the value is given by the total multiplied by z/N^2.

The two integrals in Eq. (5.23) are essentially independent and can therefore be evaluated separately. The second contains no difficulties and can be approximated using the method above. The first integral is taken over the range $[z, \infty]$, which can't be evaluated on a computer directly. We therefore make a change of variable, $z \to 1/z$, and then evaluate the integral in the same way. Figure 5.9 shows close agreement between the simulation results and the expected mean lifetime using the calculation above.

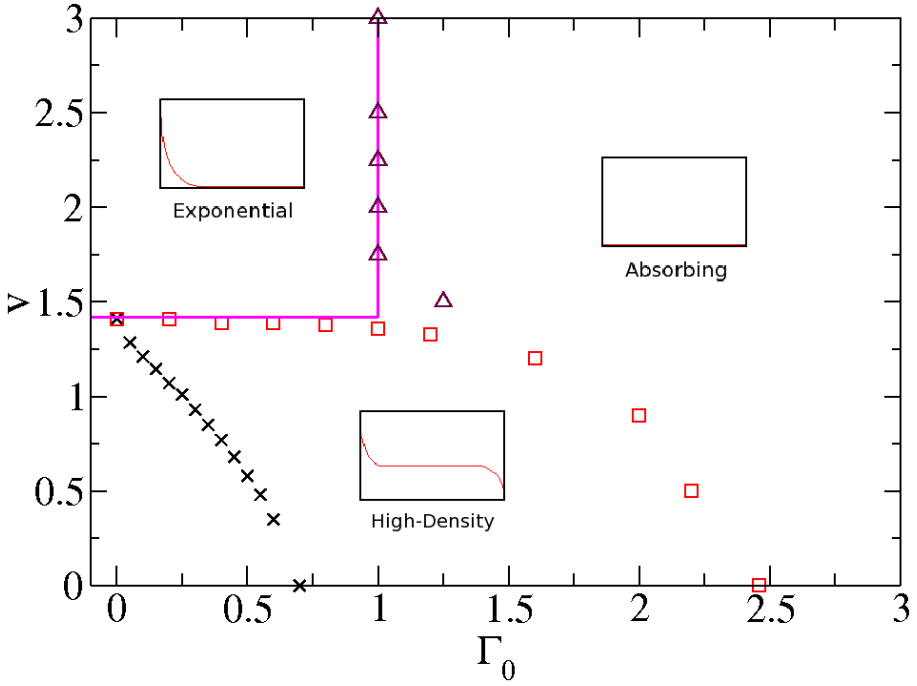

Figure 5.10: Phase diagram for $\Gamma \propto \rho$, ($a = 0.5$). The red squares correspond to the transition between high- and low-density phases. Within the low-density region, there is now a second true phase transition between low and strong noise, indicated by the maroon triangles. For comparison, we include the phase boundary of the square root noise case (black crosses). The horizontal magenta line corresponds to the zero-noise transition point $v_c \simeq 1.41$ whereas the vertical one is the theoretical prediction from the 0D model.

5.6 Linear Noise

We now turn to the investigation of the dependence of the phase diagram on the type of noise used in Eq. (4.1), by considering $\Gamma(\rho) = \Gamma_0 \rho$.

5.6.1 Phase Diagram

Upon switching from the square root to the linear noise, the phase diagram is dramatically altered (Figure 5.10).

First, the transition between the high- and low-density phases (whether exponential or absorbing) is changed significantly. To pinpoint this critical line, we proceed numerically as before. The model is now easier to simulate since close to the transition, when $\rho \ll a/b$, the fluctuations remain of order ρ and are much smaller than in the previous case, where they scaled as $\sqrt{\rho}$. Rare

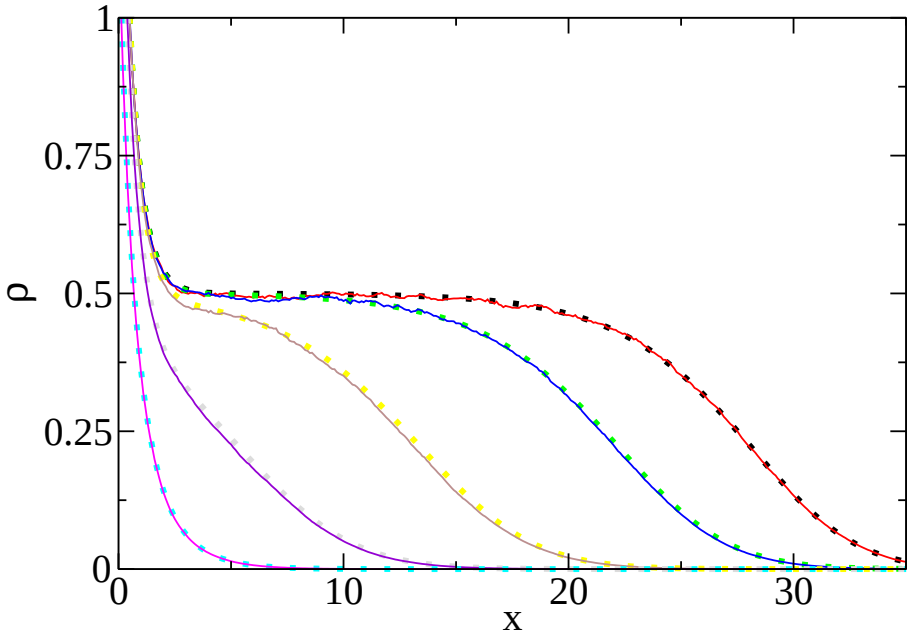

Figure 5.11: Plots of the steady-state density profiles for the linear noise ($\Gamma_0 = 0.1$, solid lines) and noiseless ($\Gamma_0 = 0$, dotted lines) cases, for $L = 40$ and values of v, from right to left, 1.30, 1.36, 1.39, 1.40 and 1.41.

events leading to absorption are unlikely and Dickman's algorithm (Section 4.3.1) works very well, in particular discretisation of the density is unnecessary as long as we truncate the noise symmetrically as before ($\eta(x,t) \leq \eta^{max}$). The noise term now cannot exceed:

$$\Gamma_i^{max}(t) = \Gamma_0 \eta^{max} \frac{\rho_i}{\sqrt{\mathrm{d}x\mathrm{d}t}}. \tag{5.24}$$

In order to avoid negative densities, we require that $|\mathrm{d}t\Gamma_i^{max}(t)| < \rho_i(t)$, but in this case the ρ dependence cancels and we are simply left with the following condition:

$$\Gamma_0 \eta^{max} \frac{\sqrt{\mathrm{d}t}}{\sqrt{\mathrm{d}x}} < 1. \tag{5.25}$$

Our results suggest that for small noise the fluctuations are irrelevant (Figure 5.11) and we recover a transition identical to the one in the deterministic limit ($\Gamma_0 \to 0$). In fact, the transition line between exponential and high-density regimes is independent of Γ_0 in the numerics, and hence horizontal,

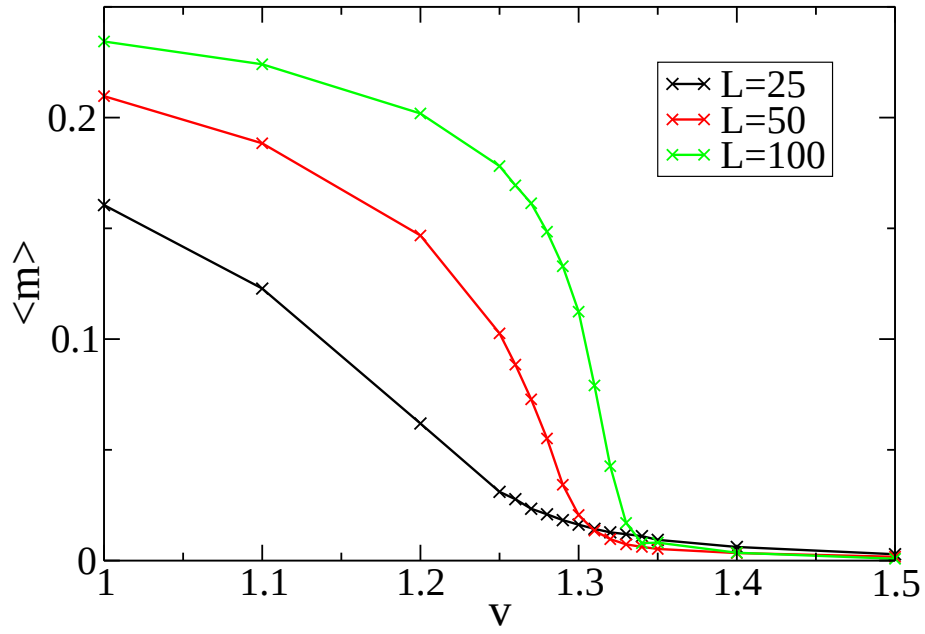

Figure 5.12: Plots of the average order parameter $\langle m \rangle$ as a function of v, for $\Gamma_0 = 1.25$ in the linear noise case, for three different system sizes (see legend). This figure is consistent with a continuous transition.

with $v_c \simeq 1.41$ as in the noiseless limit. Note that this transition is discontinuous and the band is stationary, in sharp contrast with the $\sqrt{\rho}$ noise where it performed a random walk at criticality. In the large noise case, where the stable state is absorbing rather than exponential, our simulations are consistent with a continuous transition (see Figure 5.12) and more data would be needed to discriminate it from the $v = 0$ limiting case.

5.6.2 A True Phase Transition in Low-Density Phases

The exponential profile is now completely stable for small Γ_0 and the transition between low and strong noise is a true phase transition. To understand why, we rely again on a 0D model, obtained by replacing $\sqrt{M}$ by M in the noise term of Eq. (5.5). This time, we consider the change of variable $w = \Gamma^{-1} \log M$ to obtain the additive Langevin equation. Using again the Ito formula Eq. (2.34), we obtain:

$$\dot{w} = \left(\frac{a}{\Gamma_0} - \frac{\Gamma_0}{2} \right) - \frac{\beta}{\Gamma_0} e^{\Gamma_0 v} + \tilde{\eta}(t) \tag{5.26}$$

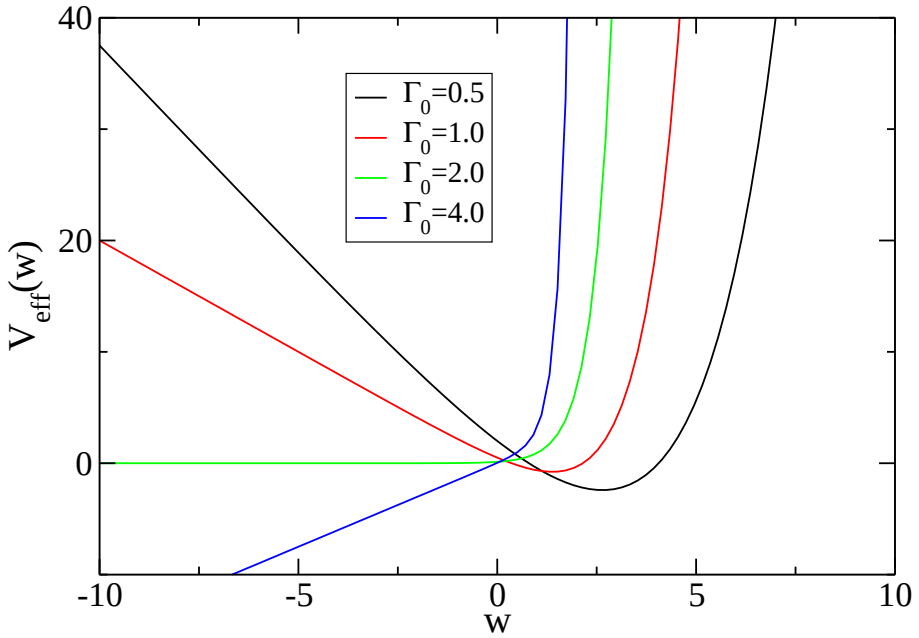

Figure 5.13: Plot of the effective potential for for $\Gamma \propto \rho$, $a = 2$, $\beta = 0.5$. From top to bottom (on the left-hand side), we used $\Gamma_0 = 0.5; 1.0; 2.0; 4.0$ while $\Gamma_c = 2$.

As before, the corresponding equation reads

$$\dot{w} = -\partial_w V_{\text{eff}}(w) + \eta; \quad V_{\text{eff}}(w) = \left(\frac{\Gamma}{2} - \frac{a}{\Gamma}\right) w + \frac{\beta}{\Gamma^2} \mathrm{e}^{\Gamma w} \tag{5.27}$$

and the putative steady state is given by $P(w) \propto \exp[-2V_{\text{eff}}(w)]$. For $\Gamma < \sqrt{2a}$, this is normalizable and the system is thus not absorbed, there is a proper normalizable steady-state distribution with $M \neq 0$. For $\Gamma \geq \sqrt{2a}$, $\exp[-2V_{\text{eff}}(w)]$ is not normalizable and the steady-state distribution once again corresponds to a delta function at the origin, the system will be absorbed. Considering now the stability of the exponential profile, we see that the effective potential has a single minimum which switches from $w = -\infty$ ($M = 0$) to finite w depending on the sign of the first term. The transition point $\Gamma_c = \sqrt{2a}$ corresponds to the normalization criterion, the spinodal line has become a true phase transition. Note that the critical line $\Gamma_c(a, \beta) = \sqrt{2a}$ is now independent of β and hence of the velocity. Numerically, we find that, for $a = 1/2$, the transition line is almost vertical and very close to $\Gamma_c(v) = 1$. This close agreement with our pre-

dictions is reinforced by the absence of any fitting parameter. As we approach the high-density phase, the mass of the exponential profile increases, and the slight bend of the transition line is presumably due to non-linear terms beyond the quadratic one, neglected in the 0D approximation. In the low noise regime, for $\Gamma_0 < \Gamma_c$, the exponential state is now stable rather than metastable and hence constitutes a true phase.

5.7 Conclusion

We have seen that the addition of an advective term, however small, has an immediate effect on the DP phase transition. It changes its character from a continuous to a discontinuous non-equilibrium transition thus lifting it out of the DP universality class. We have observed that the boundaries are crucial to the resulting behaviour. With periodic boundary conditions, advection would have little or no effect as the impact would be washed away, however no-flux boundaries mean that a preferred direction is important as density will 'pile up' at one end of the system.

With the addition of a small noise term, whose amplitude is proportional to the square root of the density, the stationary fronts observed in the banding region defined in Chapter 3 now perform a random walk throughout the system, occasionally becoming 'stuck' in the exponential profile. This regime and the strong noise regime, where the system goes to zero in a manner more like DP, are separated by an interesting dynamical transition, much like a spinodal transition.

Finally, the form of the noise is very important to choose correctly when we write down coarse-grained descriptions of microscopic models. We see here that changing the type of noise into one whose amplitude is proportional to the density itself changes the transitions quite dramatically. The dynamical transition now becomes a true phase transition and the absorbing state transition in the strong noise portion of the low-density regimes appears to have changed into a continuous transition. We can envisage the possibility of noise terms with even higher order exponents of the density, but, as the steady state probability distribution will most likely be normalizable, we expect the resulting behaviour to be much less rich.

In the next chapter, we turn to the dynamics of filopodial protrusion, an intriguing biological model that is under current scrutiny from various disciplines.

Chapter 6

Filopodial Protrusion with Molecular Motors

The dynamics of filopodial growth is of current interest to researchers in various fields as it brings together studies from biochemistry, cell biology, as well as experimental and theoretical biophysics. Filopodia and their close counterparts, lamellipodia, play an important role in cell motility [Bray 01] and other biological processes including embryonic development, wound healing and cancer metastasis [Zhuravlev 10]. Filopodia are protrusions of actin fibres, closely bundled together, that reach out and 'sense' the environment around eukaryotic animal cells. They extend and retract due to actin polymerising and depolymerising at the ends of the fibres, and their rich dynamical behaviour is still under scrutiny: for instance, Monte Carlo simulations of varying levels of complexity have been implemented [Lan 08] and Mogilner and Rubinstein proposed a mean-field theory in [Mogilner 05]. Current models have predicted realistic initial growth rates but have been unable so far to predict the wide range of lengths that have been observed [Mogilner 05]. There are various open questions about filopdia. The initiation of filopdia from lamellipodia is not completely understood, in particular, the transition between different actin morphologies. The steady-sate lengths observed in nature have not been reproduced using any existing model for protrusion, nor have the growth rates been very well understood in a quantitative way. Finally, the importance of molecular motors in filopodial growth has been confirmed, but the precise manner in which they are involved is not well understood. It is the last few questions that we seek to

address in this chapter. We use a fully agent-based model to test the current theory and its associated mean-field model. We then suggest improving the model by taking into account the role of myosin motors in transporting actin proteins, the filopodial building blocks, to the tip. We propose a new set of mean-field equations taking into account this new advection term.

6.1 Background

We first discuss some of the biology and biophysics that is known about filopodia and the processes that are currently considered to control their growth. After introducing the background theory, we present the existing set of equations [Mogilner 05] that model filopodial growth. We develop an agent-based simulation to test this mean-field description and then extend the PDEs to include the effect of myosin transport on the filopodial length.

6.1.1 Filopodia

Filopodia are finger-like protrusions at the leading edge of animal cells, emerging from a network of actin filaments resembling a scaffold, called the lamellipodium, whose role in cell motility and structure is well-documented [Pollard 03]. Filopodia 'reach out' to explore the cell's immediate environment and can bind to nearby structures: the protrusion can then retract, effectively 'pulling' the cell in the desired direction. The dynamical behaviour of filopodial growth is rich and key to several important biological processes as mentioned above.

Actin protein, called *G-actin* when freely diffusing, is the most abundant protein in many eukaryotic cells. G-actin can self-assemble to form filaments, which are double helical polymers whose subunits are arranged head to tail. These actin monomers, now called *F-actin*, are usually decorated with *myosin*, which are molecular motors that can walk along the fibres. These motors give the filaments an arrowhead pattern that has led to the terminology 'barbed' and 'pointed' ends referring to the leading edge and base of the filopodium respectively. The barbed end favours growth and the pointed end favours de-polymerisation leading to a treadmilling effect. These filaments can form branched networks, *lamellipodia*, or bundles all pointing in the same direction, *filopodia*, where the bundles are cross-linked by actin-binding proteins, and enclosed by the cell membrane, Figure 6.1. The typical diameter of a filopodium is in the region of 100 nm to 300 nm depending on the number of filaments,

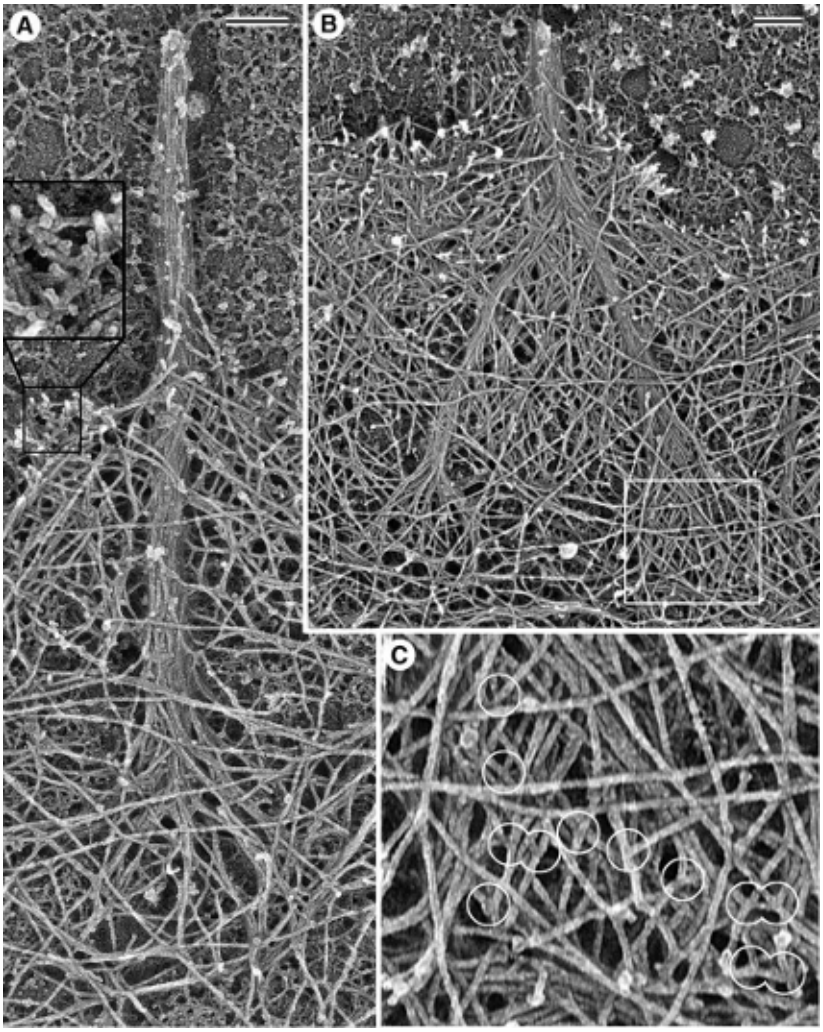

Figure 6.1: "Filopodial filaments originate from the surrounding dendritic network. Platinum replica EM. (A) Filopodium contains a tight bundle of actin filaments that splays apart at its root and becomes an integral part of the surrounding network. Filaments in the roots are long compared with the branching network of the adjacent lamellipodium (inset). (B) Recently fused filopodium consists of two sub-bundles, each of which has a splayed root; the boxed region at the root of the right sub-bundle is enlarged in C and shows many branches (encircled) at which filopodial filaments originate. Rough background outside the cell edge is due to laminin coating of the glass coverslip. Bars, 0.2 μm". Photo and caption taken from [Svitkina 03].

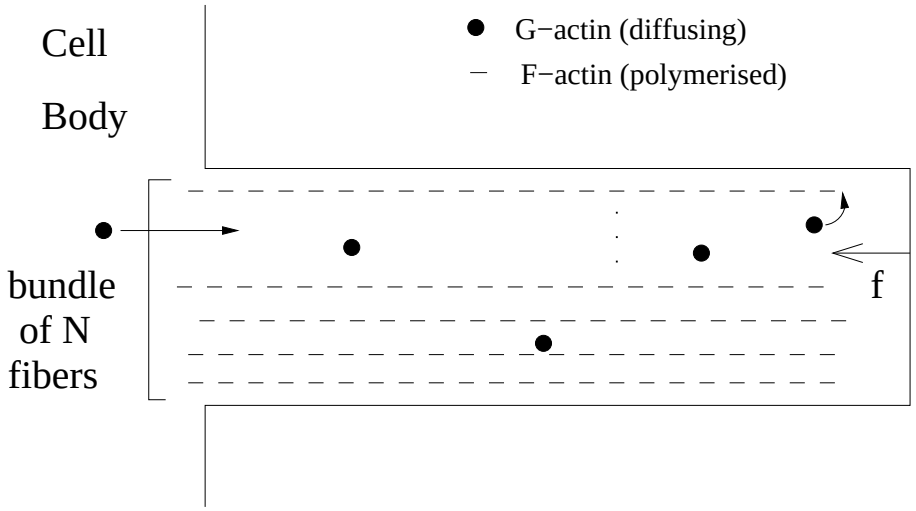

Figure 6.2: Schematic diagram of a filopodium. Diffusing G-actin and polymerised F-actin are shown.

$N \approx 10 - 30$ [Mogilner 05], and they usually grow to several microns in length although they have been observed up to 40 μm [Mogilner 05]! G-actin diffuse in the bulk of the cell with concentration 10 μM and with diffusion constant $D \approx 5\mu\text{m}^2/\text{s}$ [McGrath 98]. Although a comprehensive set of the individual proteins involved in filopodial growth is established, their interactions remain to be explained [Lan 08].

A filopdodium, such as those in Figure 6.1, is shown schematically in Figure 6.2. Several processes are involved in the current model for filopodial growth. There is the membrane resistance force, $f = 10 - 50$ pN [Mogilner 05], where tension in the membrane due to its elasticity seeks to restore its shape. Note that this force is not due to viscous drag, which yields a force many orders of magnitude smaller. In [Mogilner 05], the authors find that at least 10 filaments are required to prevent buckling and support growth to the μm range. Diffusing G-actin polymerise favourably at the barbed ends of the filaments but this is limited by the availability of actin monomers in the vicinity of the tip, and therefore by diffusion. The monomers must be correctly oriented for polymerisation to occur, and this happens in about 2% of collisions [Pollard 03], resulting in an effective polymerisation rate $k_{\text{on}} = 10\mu\text{M}^{-1}\text{s}^{-1}$ [Mogilner 05]. The half-width of an actin monomer is $\delta = 2.7$nm; this gives a growth rate of $0.27\mu\text{m s}^{-1}$ indicating that other effects must also be in play ([Mogilner 05] gives $0.05\mu\text{m s}^{-1}$ for the protrusion rate). F-Actin slowly de-polymerises, at

Table 6.1: Model Parameters

Symbol	Meaning	Value	Reference
r_{cyl}	Radius of filopodium	100 nm	[Sheetz 92]
N	Number of fibres	$\sim 10 - 30$	[Mogilner 05]
f	Membrane resistance force	$\sim 10 - 50$pN	[Mogilner 05]
k_bT	Thermal energy	4.1 pN $\times$ nm	[Peskin 93]
δ	Actin monomer half-width	2.7 nm	[Peskin 93]
D	G-actin diffusion constant	$\sim 5\mu\text{m}^2/\text{s}$	[McGrath 98]
c_0	G-actin concentration in the cell body	10 μM	[Mogilner 05]
k_{on}	Polymerisation rate	10 $\mu\text{M}^{-1}\text{s}^{-1}$	[Pollard 86]
k_{off}	De-polymerisation rate at tip	1.4 s^{-1}	[Carlsson 01]
v_{retr}	Retrograde flow velocity	10-30 nm s^{-1}	[Gardel 08]
η	Geometric conversion coefficient	18.9 μM^{-1} μm^{-1}	[Mogilner 05]

a rate $K_{\text{off}} = 1.4\text{s}^{-1}$, at the pointed end as the lamellipodium advances. This de-polymerisation, together with the polymerisation at the tip, provides the 'treadmilling' effect. Finally, there is a retrograde flow, a complicated feedback mechanism, whereby the growing network's push on the membrane yields a force moving the filaments back towards the cell body [Lin 95]. Values for the velocity of the retrograde flow vary from 10 nm s^{-1} [Berg 02] to 70 nm s^{-1} [Lan 08], where the authors also attribute its cause to the above-mentioned treadmilling effect. Other limiting mechanisms are in play, such as capping at the barbed end via specialised capping proteins, but we do not model them here as they are often disabled during filopodial growth [Schafer 04].

6.1.2 Mean-field theory

We first summarise the existing mean-field theory proposed in [Mogilner 05]: first, we have a diffusion equation for the G-actin concentration, $c(x,t)$, in a horizontal slice of the filopodium at a distance from the base $x \to x + \text{d}x$:

$$\frac{\partial c}{\partial t} = D\frac{\partial^2 c}{\partial t^2}. \tag{6.1}$$

$c(x,t)$ also obeys boundary conditions, which describe a constant concentration at the base:

$$c(0) = c_0 \tag{6.2}$$

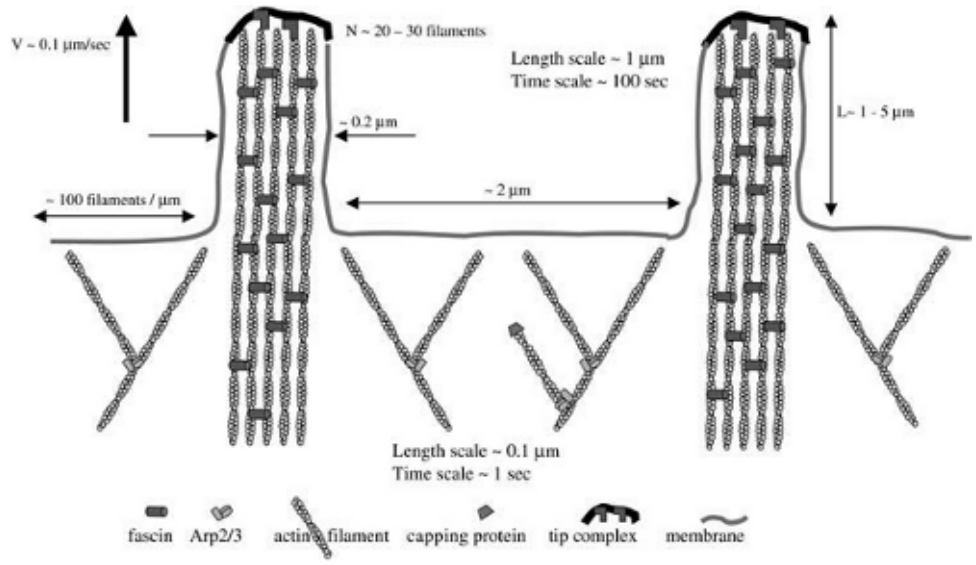

Figure 6.3: Organization and characteristic scales of filopodia and lamellipodia. Photo and caption from [Mogilner 05]

and the flux of G-actin at the tip is equal to the number of monomers polymerising onto the filaments [Mogilner 05]:

$$-D\frac{\partial c}{\partial x}\bigg|_{L(t)} = \left(\frac{N}{\eta\delta}\right)\frac{\mathrm{d}L}{\mathrm{d}t}\bigg|_{v_{\mathrm{retr}}=0} \tag{6.3}$$

where $\eta = 600\pi r_{\mathrm{cyl}}^2$ $\mu\mathrm{M}^{-1}$ $\mu\mathrm{m}^{-1}$ is a geometric conversion factor giving the number of actin monomers per micrometre of length (1 μM corresponds to about 600 particles / $\mu\mathrm{m}^3$). The right-hand side of Eq. (6.3) is evaluated without retrograde flow as this term will affect the length of the filopodium but not the flux at the tip.

6.1.3 Brownian Ratchet

The length of the protrusion $L(t)$ depends on the concentration of G-actin at the tip and the availability of space between the filament end and the membrane for the actin to occupy once polymerised. The membrane tip fluctuates around $L(t)$ subject to a restoring force, f, pushing it in the $-x$ direction back towards the cell body. $\frac{\mathrm{d}L}{\mathrm{d}t}$ therefore obeys the Brownian ratchet equation [Peskin 93], which is derived as follows. Neglecting flexibility, we consider one fibre only,

the probability density $P(x,t)$ that the membrane is a distance x from the fibre tip at time t will diffuse with constant D_{mem} subject to the force f. If $x < \delta$, $P(x,t)$ will be enhanced by configurations with membrane distance $x+\delta$ polymerising with probability $\alpha = k_{\text{on}}c(L)$ and decreasing the distance from the tip to x. Similarly, it will deplete at a rate $\beta = k_{\text{off}}$. On the other hand, if $x > \delta$, $P(x,t)$ will increase via the above mechanism and via de-polymerisation of configurations with $x-\delta$ and will be decreased both by polymerisation and de-polymerisation. Putting all of this together we obtain:

$$\begin{aligned}\frac{\partial P(x,t)}{\partial t} = D_{\text{mem}}\frac{\partial^2 P}{\partial x^2} + \left(\frac{fD_{\text{mem}}}{k_B T}\right)\frac{\partial P}{\partial x} \\ + \alpha[P(x+\delta,t) - \theta(x-\delta)P(x,t)] \\ + \beta[\theta(x-\delta)P(x-\delta,t) - P(x,t)]\end{aligned} \tag{6.4}$$

where $\theta(x) = 0$ for $x < 0$ and $= 1$ for $x > 0$ is the Heaviside function. Once $P(x,t)$ is obtained, we can write an equation for the ratchet velocity. This will equal δ times the net rate of polymerisation per system in the ensemble:

$$v = \delta\frac{\alpha\int_\delta^\infty P(x)\mathrm{d}x - \beta\int_0^\infty P(x)\mathrm{d}x}{\int_0^\infty P(x)\mathrm{d}x} \tag{6.5}$$

where the limits in the first integral in the denominator are set to exclude any configurations where $x < \delta$. We assume that the diffusion of the membrane is fast compared with the polymerisation rate, $=\frac{k_{\text{on}}\delta^2}{D_{\text{mem}}} \sim 100\text{s}^{-1}\times(3\times10^{-9}\text{m})^2/(1\times 10^{-6}\text{m})^2\text{s}^{-1} = 3\times10^{-4} \ll 1$, and therefore ignore the terms proportional to α, β in Eq. (6.4). We can then easily solve for the steady state giving $P(x) \propto e^{-fx/k_BT}$, and finally insert this into Eq. (6.5), to obtain:

$$\frac{\mathrm{d}L}{\mathrm{d}t} = \delta\left(\alpha e^{-f\delta/k_BT} - \beta\right) \qquad\qquad f > 0. \tag{6.6}$$

In order to modify this equation to account for a bundle of N fibres, we take $k_{\text{on}} \to Nk_{\text{on}}$ and $k_{\text{off}} \to Nk_{\text{off}}$ to account for increased polymerisation and de-polymerisation rates as each fibre can do both. Similarly, it will take N polymerisations to extend L by an amount δ and this is equivalent to setting $\delta \to \delta/N$ [Burroughs 06]. Finally, if we introduce the retrograde flow, whose velocity v_{retr} constantly decreases L, we have a full expression for the velocity

of the filopodial tip:

$$\frac{\mathrm{d}L}{\mathrm{d}t} = \delta\left(k_{\mathrm{on}}e^{-\beta f\delta/N}c(L) - k_{\mathrm{off}}\right) - v_{\mathrm{retr}} \tag{6.7}$$

where $1/\beta = k_bT = 4.1\mathrm{pN} \times \mathrm{nm}$ is the thermal energy. Several predictions can be obtained from these equations. First, we can compute an initial protrusion rate, using the values in table 6.1 above, and taking $f = 20$ pN, $N = 20$ fibres and $v_{\mathrm{retr}} = 15$ nm s^{-1}, we obtain $v_{\mathrm{ini}} = 0.12\mu$m s^{-1} which is close to the value given in [Mogilner 05] for the protrusion rate (0.05μm s^{-1}).

We can derive a maximal length predicted from the above equations. We assume that the density profile in the steady state will be a linear decreasing function of x, and the gradient can therefore be reasonably approximated by:

$$\frac{\partial c}{\partial x} = \frac{c(L) - c(0)}{L}. \tag{6.8}$$

This assumption is backed up by observation of the numerics (Figure 6.13 (a)). We then use the boundary condition at the tip Eq. (6.3) to derive an expression for the concentration at the tip, $c(L)$:

$$c(L) = \frac{LNk_{\mathrm{off}} + c(0)D\eta}{D\eta + LNk_{\mathrm{on}}\exp(-f\delta/Nk_BT)}. \tag{6.9}$$

We then substitute this result into Eq. (6.7) and require $\mathrm{d}L/\mathrm{d}t = 0$ to find the steady-state length:

$$L_{\mathrm{max}} = \frac{D\eta}{Nk_{\mathrm{on}}}\left(\frac{\delta k_{\mathrm{on}}c(0)}{v_{\mathrm{retr}}} - \left[\frac{\delta k_{\mathrm{off}}}{v_{\mathrm{retr}}} + 1\right]\mathrm{e}^{\frac{f\delta}{Nk_BT}}\right). \tag{6.10}$$

Using the same values as the previous calculation, we find the maximum length to be 7.4μm. Figure 6.4 shows a simulation of the above PDEs using these same values, we see that the predicted maximum length agrees well as does the initial growth rate (inset), albeit only for a very short time. Finally, we can use Eq. (6.7) to predict the ratchet stalling force, the force required to stop growth altogether. Setting $\dot{L} = 0$, we find:

$$f_s = -\frac{Nk_BT}{\delta}\log\left(\frac{k_{\mathrm{off}}}{c_0k_{\mathrm{on}}} + \frac{v_{\mathrm{retr}}}{\delta k_{\mathrm{on}}c_0}\right). \tag{6.11}$$

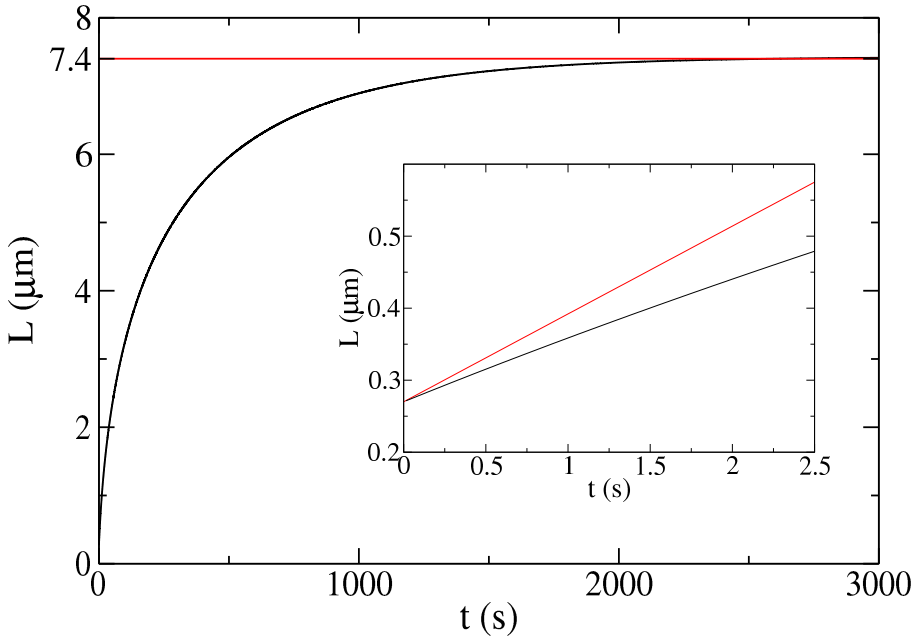

Figure 6.4: Filopodium length as a function of time for numerical integration of Eqs. (6.1) and (6.7) (black) compared with theoretical predictions for the maximal steady state length (red) and the initial growth velocity (inset). Simulation parameters are $N = 20$, $f = 20$ pN, $a_0 = 10$ μM, $k_{\text{off}} = 1$ s^{-1} and $v_{\text{retr}} = 15$ nm s$^{-}1$.

Using $v_{\text{retr}} = 15$ nm s^{-1} gives $f_s = 81$ pN, which is outside of the assumed range for the membrane resistance force (10-50 pN) and presumably does not therefore have an effect in the dynamics of real filopodia.

6.2 Agent-based Simulation

Agent-based simulations are useful for modelling the microscopic dynamics of a process directly. By producing such a simulation, we can include a very high level of detail, such as the diffusive motion of each G-actin monomer. We now write a fully agent-based simulation for a filopodium, which includes fluctuations in the G-actin density. Our purpose is to test the mean-field results for the existing theory, and we give details of this microscopic approach below. We will record the fibre and g-actin positions in three dimensions and use a parallel update scheme. We will then implement the following physical processes: diffusion, injection of particles at the base, diffusion of the membrane tip subject to the restoring force, polymerisation at the tip, de-polymerisation at the base,

Table 6.2: Typical Simulation Parameters

Symbol	Meaning	Value	Relevant Real Value
$\mathrm{d}l$	Actin monomer half-width	0.5	$\delta = 2.7$ nm
$\mathrm{d}l_\mathrm{g}$	G-actin maximum step	0.2	$D = 5\ \mu\mathrm{m}^2/\mathrm{s}$
$\mathrm{d}l_\mathrm{m}$	Membrane maximum step	0.1	$D_m \sim \mathcal{O}(1)\ \mu\mathrm{m}^2/\mathrm{s}$
Δx	Converts x_sim to x_real	5.4 nm	
Δt	Converts t_sim to t_real	0.039 μs	
$\Delta\rho$	$1/\eta$	52.9 μM nm	
δ_pol	Polymerisation radius	0.5	
P_pol	Polymerisation probability	0.00917	$k_\mathrm{on} = 10\ \mu\mathrm{M}^{-1}\mathrm{s}^{-1}$

and the retrograde flow.

6.2.1 Set-up

We set up the simulation as follows:

- **Simulation constants**: input the real values for δ, D, c_0, r_cyl, z_top, f, N, kT (see Table 6.1). We choose simulation parameters for $\mathrm{d}l$, $\mathrm{d}l_\mathrm{g}$, $\mathrm{d}l_\mathrm{m}$ (see table 6.2).

- **Simulation units**: We first obtain the length scales in the simulation in terms of nm, μs, and μM:
$$\Delta x = \frac{\delta}{\mathrm{d}l}, \tag{6.12}$$
i.e. one in simulation units corresponds to Δx nm. Similarly, to fix Δt we use Eq. (2.72):
$$\Delta t = \frac{\mathrm{d}l_\mathrm{g}^2 \Delta x^2}{6D}. \tag{6.13}$$
We calculate $\Delta\rho$, which converts μM values into number of molecules per unit length:
$$\Delta\rho = \frac{1}{\eta} = \frac{1}{0.6\pi r_\mathrm{cyl}^2} \tag{6.14}$$
where η is the geometric factor from [Mogilner 05] (1 μM gives about 600 molecules per $\mu\mathrm{m}^3$). Finally, we convert all of the real values into simulation units using these conversion factors, e.g. $r_\mathrm{cyl}^\mathrm{sim} = r_\mathrm{cyl}/\Delta x$.

- **Fibre position**: create an array to record the 3-dimensional positions of each F-actin monomer in each fibre. Although the fibres are constrained

to be straight, recording the position of each monomer allows the simulation to be extended to include bending more easily. The fibres must be positioned far enough apart that the polymerisation region (see below) around each tip do not overlap.

There is a further subtlety in the positioning of the base of each fibre, i.e. the distance from the bottom. In reality, the fibres will bend and fluctuate a little but we model them here as completely rigid and positioned with deterministic precision. A problem arises when we extend the ratchet equation Eq. (6.6) to account for a bundle of fibres resulting in Eq. (6.7). If we model the fibres as all having their base position at the same distance from the bottom of the filopodium, the membrane tip will 'lock' onto the end of the bundle, and spoil the growth as well as the mean-field approximation of taking $\delta \to \delta/N$. This can be overcome by placing the fibres randomly within δ of the base or, as we have chosen to do, spacing them equally in the region $[0, \delta]$ to ensure maximum distance from this 'locking' problem.

- **G-actin positions**: We record the 3-dimensional positions for the $n_{\mathrm{g}} = c_0 z_{\mathrm{top}}/\Delta\rho$ monomers that are randomly distributed along the filopodium at the start of the simulation.

6.2.2 Physical Processes

All of the processes below are carried out during each time-step.

Diffusion

Each particle diffuses in each dimension as explained in Chapter 2: we randomly choose one of the freely-diffusing G-actin monomers and draw one random number, r_i, flatly-distributed within [0,1] for each dimension $i = 1, 2, 3$. The particle attempts to move by an amount $(1 - 2r_i)\mathrm{d}l$ for each i and the move is accepted if its final position is within the filopodium, i.e. no-flux boundary conditions. The move is also accepted if the particle attempts to exit the filopodium via the base, i.e. it is allowed to re-enter the main body of the cell but cannot traverse the cell membrane. This is repeated n_{g} times so that each particle moves on average once in each time-step.

As a check, we added a further complication that if the particle attempts to move beyond the cylinder wall, it will 'bounce' off the wall rather than the move

simply being rejected (reflecting boundary conditions). We found that this had very little effect and therefore did not implement it in any further simulations.

G-actin Source at base

The cell body has a concentration of G-actin c_0 and there will be a constant source of G-actin at the base of the filopodium. To work out the probability for a monomer to cross into the system per unit time, we consider one particle within $\mathrm{d}l_\mathrm{g}$ of the base. It has probability $1/\mathrm{d}l_\mathrm{g}$ of being at distance x from the origin of the protrusion. The probability that this particle will enter the system is:

$$\int_x^{\mathrm{d}l_\mathrm{g}} \frac{1}{2\mathrm{d}l_\mathrm{g}} \mathrm{d}m = \frac{1}{2}\left(1 - \frac{x}{\mathrm{d}l_\mathrm{g}}\right). \tag{6.15}$$

Multiplying this by $1/\mathrm{d}l_\mathrm{g}$ and integrating over all possible starting positions gives a probability $1/4$ for this particle to enter the system in one time-step. Finally, we multiply by the number of monomers that will be found within range of the base $c_0\mathrm{d}l_\mathrm{g}/\Delta\rho$.

Care must be taken over where to place the new monomer as the probability of its initial distance from the base is not uniform: the number of monomers that can reach a position, y, by jumping into the system will increase as the boundary is approached and simply making it uniform results in an artificially high steady-state concentration in the system. We consider a G-actin particle sitting outside of the filopodium but within a distance $z = \mathrm{d}l_\mathrm{g} - y$ of the base, where $y \in [0, \mathrm{d}l_\mathrm{g}]$. Its probability to 'jump' into the system at position y is constant $P(\text{'jump to y'}) = 1/2\mathrm{d}_\mathrm{g}$. This means that the number of monomers to jump to position y must be proportional to the number of monomers existing within the slice with width z of the base. This will increase linearly with z, and therefore decrease linearly with y. We therefore seek to draw a random number from the following distribution:

$$p(y)\mathrm{d}y = (\mathrm{d}l_\mathrm{g} - y)\,\mathrm{d}y. \tag{6.16}$$

We use the transformation method in [Press 92], and find that, if x is a random number uniformly distributed over [0,1], then y will give the correct distribution if:

$$y(x) = \mathrm{d}l_\mathrm{g}\left(1 - \sqrt{1-x}\right). \tag{6.17}$$

Membrane Force at tip

The membrane at the leading edge of the protrusion experiences a restoring force, $f \sim$ 10-50 pN [Mogilner 05]. This attempts to pull the membrane back towards the cell body, but the membrane is stopped by the fibres of filopodia themselves (the ratchet). We model the tip as a flat disc with diameter equal to the diameter of the filopodium. The membrane will fluctuate about its position in the direction of protrusion and we therefore make it undergo a random walk in the presence of a force. We use Metropolis-Hastings [Press 92]: moves that take the tip away from the cell body will incur an energy penalty and will only be accepted with probability $\exp(-f|\Delta z|/k_bT)$. Moves that take the membrane tip towards the cell body are accepted automatically as long as there is space, i.e. the membrane cannot go further back than the tip of the longest fibre. We use $\mathrm{d}l_\mathrm{m} = 0.1$, corresponding to a diffusion coefficient $D_\mathrm{m} = 1.25\ \mu\mathrm{m}^2\ \mathrm{s}^{-1}$. This is reasonable; if we consider the Stokes value of the diffusion for a spherical particle $D = k_bT/6\pi\eta R$, and assume the viscosity of water, we get $D \sim 4.1{\times}10^{-21}\mathrm{J}/(20{*}\ 10^{-3}\mathrm{Pa\ s}{*}0.54{\times}10^{-6}\mathrm{m} \sim 0.5\ \mu\mathrm{m}^2\ \mathrm{s}^{-1}$. Note that this is fast compared with the polymerisation ($k_\mathrm{on}\delta^2 = 100\mathrm{s}^-1 * 2.7^2 \times 10^{-6} \sim 7 \times 10^{-8}\ \mu\mathrm{m}^2\ \mathrm{s}^{-1}$), as required for the ratchet equation to be a good approximation [Peskin 93].

Polymerisation

G-actin that diffuses up to the leading edge of the filopodium will polymerise to become F-actin. In order for this to occur, the particle must be within range of the tip of the fibre on to which it will attach and there must be enough space between the fibre tip and the membrane for the fibre to grow by δ. In the simulation, the monomers are essentially point particles so we must invoke a polymerisation radius [Andrews 04], a region surrounding the fibre tip within which particles can polymerise. The radius must be large enough so that a particle cannot 'jump' over the fibre in one time-step but not so large that neighbouring fibres will overlap. Once the region width is set, we must choose a polymerisation probability for a particle to polymerise so that the steady-state polymerisation rate, k_on, agrees with experiment.

The polymerisation probability can be obtained via a simple calculation, we have a polymerisation volume $4\pi\delta_\mathrm{pol}^3/3$ and 1 μM gives 4.966×10^{-5} particles in this volume. This means that, if the polymerisation probability is unity, there will be 1277 polymerisations per second. Setting $P_\mathrm{pol} = 0.00783$ should

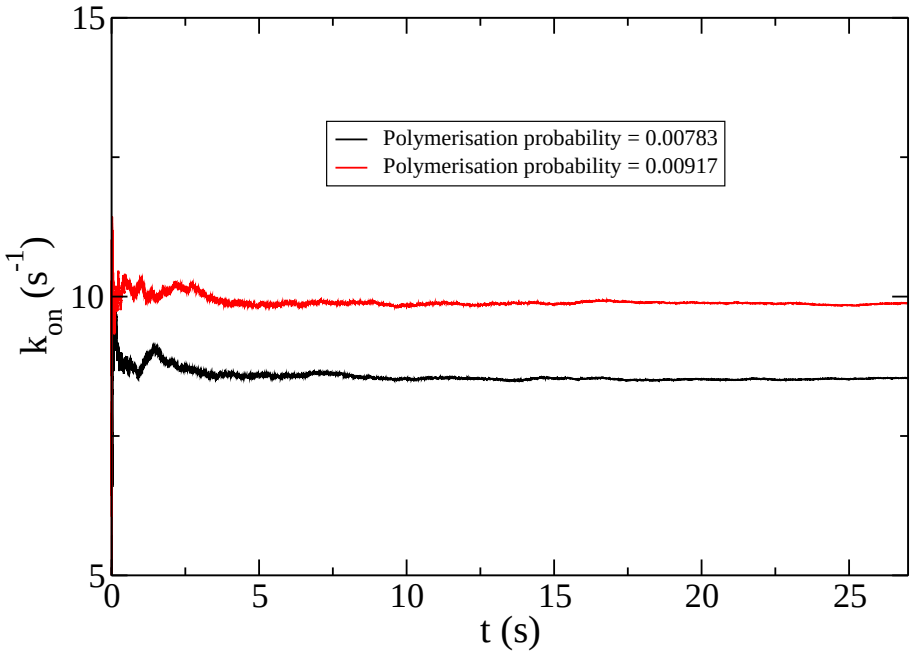

Figure 6.5: Measurement of k_{on} as a function of time from G-actin diffusing in a closed cylinder; once polymerised, the actin are replaced randomly in the space. Two values of P_{pol} are shown.

therefore give the required $k_{\text{on}} = 10\mu\text{M}^{-1}\text{s}^{-1}$ per fibre.

In order to test these numbers, we use a more artificial set-up for the simulation. We have a closed cylinder with a fixed concentration of freely-diffusing monomers; when one of the particles polymerises, the fibre remains the same length and the particle is re-inserted at a random location within the cylinder. We found that using $P_{\text{pol}} = 0.00783$ gave a reduced $k_{\text{on}} = 8.5\ \mu\text{M}^{-1}\ \text{s}^{-1}$ per fibre (Figure 6.5) and therefore used $P_{\text{pol}} = 0.00917$ in subsequent simulations. We also ensured that k_{on} remained constant under changes of concentration, number of fibres and cylinder radius.

De-polymerisation

Occasionally, F-actin at the tip of the fibre will de-polymerise. This occurs in real cells at a rate $k_{\text{off}} = 1.4\ \text{s}^{-1}$ [Carlsson 01]. We model this by removing one monomer at the tip of each fibre at each time-step with probability $\Delta t/k_{\text{off}}$. This particle then becomes a freely-diffusing G-actin monomer.

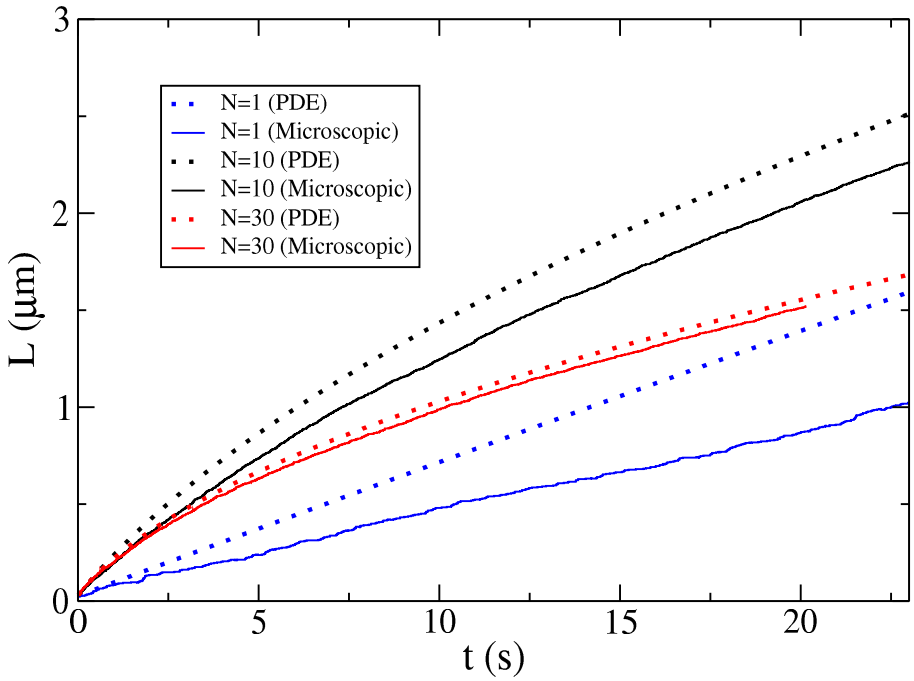

Figure 6.6: Filopodium length as a function of time for agent-based simulations (solid lines) and numerical integration of Eqs. (6.1) and (6.7) (dotted lines) for $N = 1, 10, 30$ actin filaments in the bundle. Other simulation parameters are $f = 2$ pN, $a_0 = 10$ μM, $k_{\text{off}} = 1$ s^{-1} and $v_{\text{retr}} = 0$.

Retrograde Flow

Finally, we model the retrograde flow by 'pulling back' the fibres by one F-actin monomer every fixed number of time-steps thereby losing one particle from the base.

6.3 Comparison with Mean-Field Results

Now that we have both the agent-based simulation and numerical integration of the stochastic PDEs Eqs. (6.1) and (6.7) in place, we can generate data for the filopodium length as a function of time with a view of comparing the two. This will help to understand whether the mean-field model is a good approximation for the system it tries to describe and, if so, what ranges of parameters it works well for. In general as we show below, the agreement is good; for some values of the parameters the two methods agree quantitatively as well as qualitatively. Varying the different constants affects the degree to which the two agree, as we

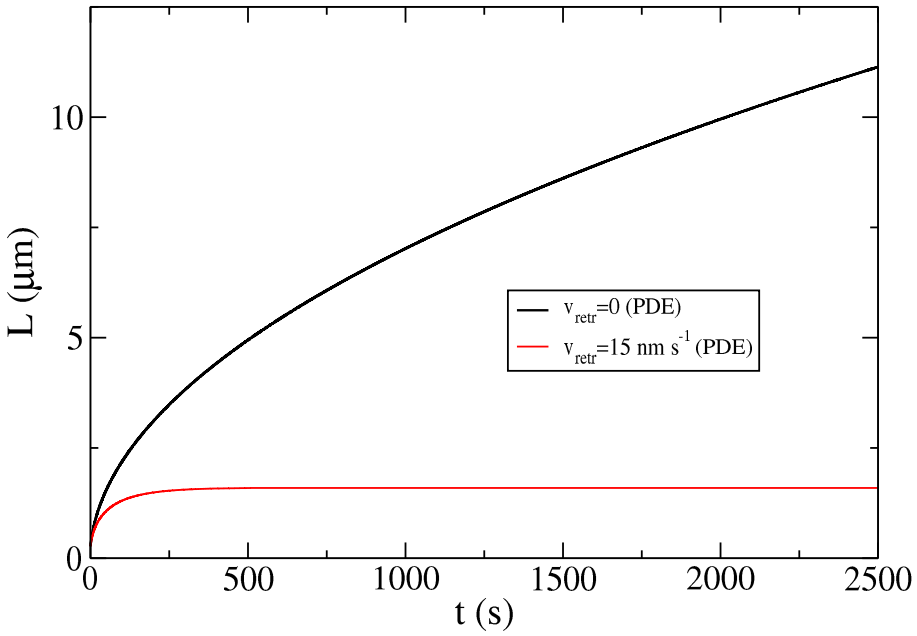

Figure 6.7: Continuum model results for filopodium length as a function of time for $N = 100$ actin filaments in the bundle. We see that although growth is very slow and slows down considerably at the beginning, steady state is still not reached after 2500 seconds when there is no retrograde flow. We see that even a small retrograde flow rate ($v_{\text{retr}} = 15$ nm s^{-1}) induces the system to reach a steady state relatively quickly. Other simulation parameters are $f = 2$ pN, $a_0 = 10$ μM, $k_{\text{off}} = 1$ s^{-1}.

will see below, but even when they differ quantitatively, they are in qualitative agreement.

In Figure 6.6, we see that for larger N, the agreement between agent-based simulation and the PDEs is good but deteriorates when N is reduced. This is probably due an increased effect of fluctuations (neglected in the mean-field continuum approach) with small numbers of fibres. Predictably, increasing N slows down the growth even though steady state is still not reached (see Figure 6.7); with $N = 1$ however, the growth is considerably reduced as in this case the force $f = 2$ pN is approaching the stalling force ($f_s = 7.8$ pN).

With $N = 30$, the effect of varying the force, f, is small in the PDE (Figure 6.8). Increasing f decreases growth but not markedly for small values $f = 1-5$ pN. When $f = 5$ pN, the agent-based simulation begins to be affected, thus creating a discrepancy between the simulation and numeric results. Increasing

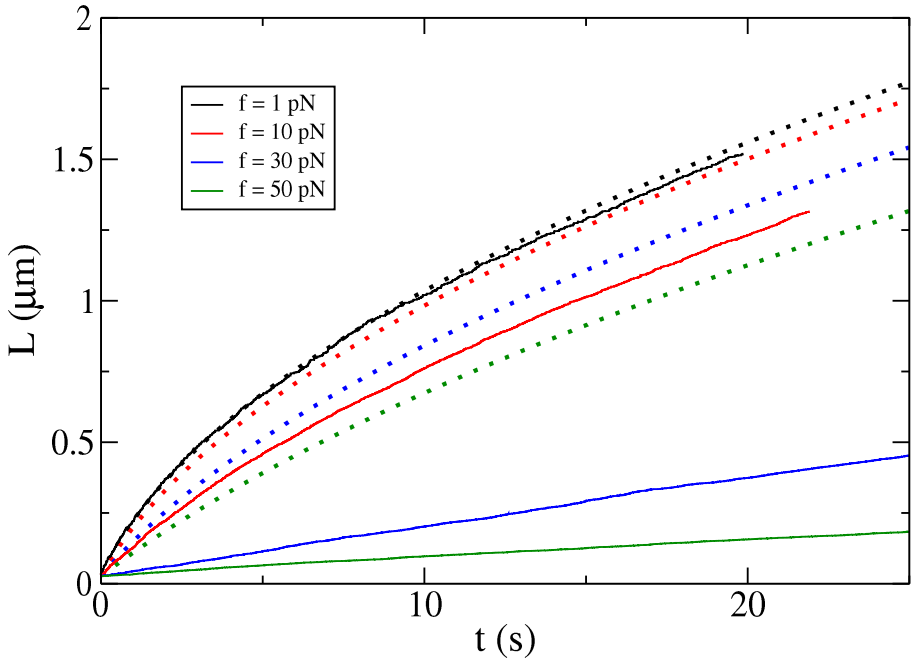

Figure 6.8: Filopodium length as a function of time for agent-based simulations (solid lines) and numerical integration of Eqs. (6.1) and (6.7) (dotted lines) while varying the membrane resistance force $f = 1, 10, 30, 50$ pN. Other simulation parameters are $N = 30$, $a_0 = 10$ μM, $k_{\text{off}} = 1$ s^{-1} and $v_{\text{retr}} = 0$

the force further decreases the growth rate until the stalling force is reached. The prediction for the stalling force with $N = 30$ is given by Eq. (6.11) as $f_s = 210$ pN and both the continuum model solution and the microscopic dynamics respect this. The greater sensitivity of the agent-based simulation is presumably due to the strong mean-field approximation inherent in taking $\delta \to \delta/N$ for the bundle. It should be mentioned that any other boundary condition for the fibres, e.g. having all of the pointed ends at the same height, results in a worsening of this problem.

Increasing a_0 speeds up the growth (Figure 6.9), as would be expected, and has seemingly little effect on the agreement of the mean-field with the microscopic simulation. If we now reintroduce the retrograde flow, v_{retr}, we find that the system can now reach a steady state (Figure 6.7) indicating that the filopodium is not only limited by the diffusion of G-actin but must also be controlled by a steady rearward flow of all of its components. For a small membrane resistance force, $f = 1$ pN, we see in Figure 6.10 that the agreement between

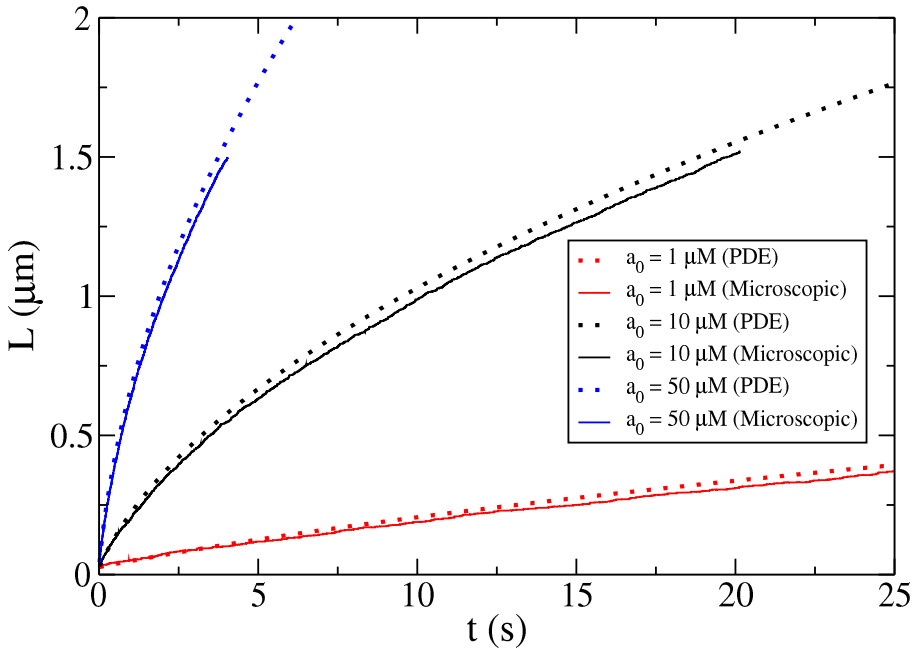

Figure 6.9: Filopodium length as a function of time for agent-based simulations (solid lines) and numerical integration of Eqs. (6.1) and (6.7) (dotted lines) while varying the concentration in the bulk of the cell $a_0 = 1, 10, 50$ μM. Other simulation parameters are $N = 30$, $f = 2$ pN, $k_{\text{off}} = 1$ s^{-1} and $v_{\text{retr}} = 0$

the agent-based simulation and analytical solution of PDEs is good. For small realistic values of the retrograde flow, it takes the PDEs around 1000 seconds to reach the steady state, but with greater values, such as $v_{\text{retr}} = 70$ nm s^{-1} employed in [Mogilner 05], we find that it happens an order of magnitude faster. In Figure 6.11, we compare the steady-state lengths found in the numerical simulation of the analytics with the prediction Eq. (6.10) for several values of the resistance force and the retrograde flow.

We have seen in this section that in general the agreement between the agent-based model and numerical simulation of the mean-field model is very good. Specifically, the only parameter which appears to behave differently in the simulation is the force, where increasing the force yields a much stronger effect on the agent-based model than on the PDE, presumably due to effects neglected in the mean-field approximation to derive the continuum model. The numerical simulation of the PDEs is computationally more efficient, allowing for longer times to be simulated and for more variation in the parameters.

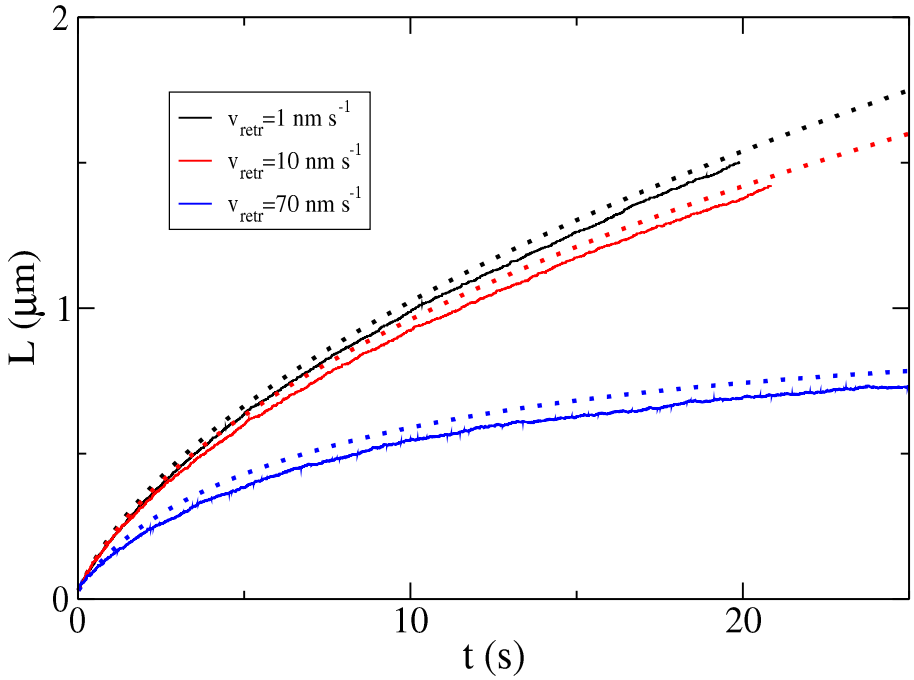

Figure 6.10: Filopodium length as a function of time for agent-based simulations (solid lines) and numerical integration of Eqs. (6.1) and (6.7) (dotted lines) while varying the retrograde flow rate $v_{\text{retr}} = 1, 10, 70$ nm s^{-1}. Other simulation parameters are $N = 30$, $f = 2$ pN, $k_{\text{off}} = 1$ s^{-1} and $a_0 = 10$ μM

We can see from the numerical results that for realistic values of the parameters, the maximal length that can be supported by this diffusion-limited process is quite small. Although there will be fluctuations about the observed length, the distribution will be narrow due to the membrane load and the actin concentration profile [Lan 08]. There must therefore be another mechanism that allows the filopodia to reach lengths as large as 40 μm, and for this we propose the effect of directed transport by myosin motors. The role of motors in transporting and polymerising actin is established, [Berg 01], and has been suspected to be involved with filopodial growth for some time [Wang 96, Berg 02]. Whereas a long bundle will have to wait a significant amount of time for an actin monomer to reach the tip by diffusion alone, it is possible that the transport process from advection will be much faster. In the following section, we analyse the effect of adding this new term to the existing mean-field model and explore this new system using numerical simulations of the resulting partial differential

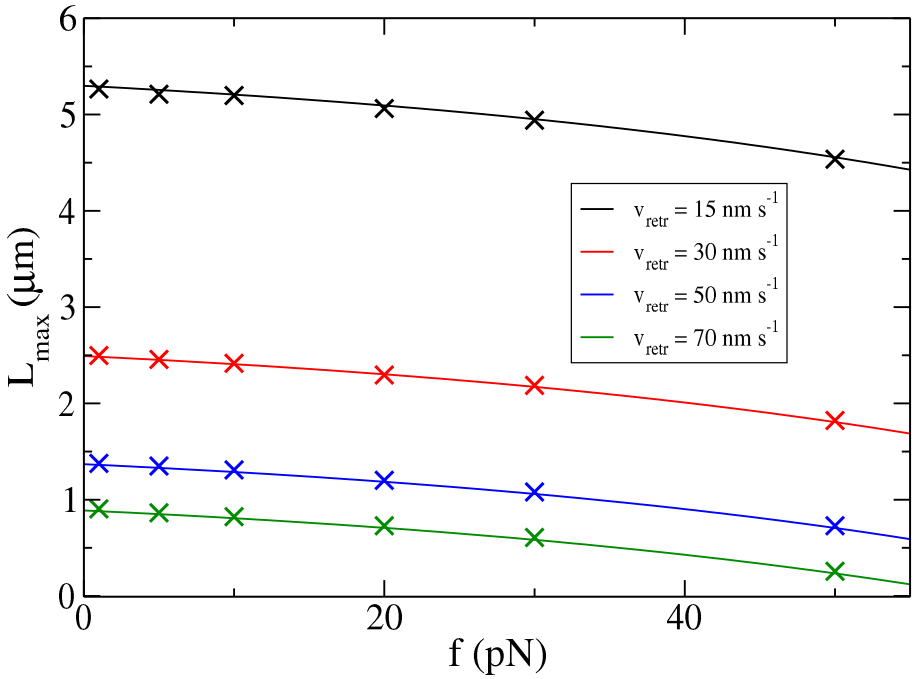

Figure 6.11: Steady-state filopodium length as a function of membrane resistance force from analytic prediction (solid lines) and numerical integration of Eqs. (6.1) and (6.7) (crosses) for various values of the membrane resistance, $f = 1.0, 5.0, 10.0, 20.0, 30.0, 50.0$ pN. The retrograde flow rate is also varied $v_{\text{retr}} = 15, 30, 50, 70$ nm s^{-1}. Other simulation parameters are $N = 30$, $k_{\text{off}} = 1$ s^{-1} and $a_0 = 10$ μM

equations.

6.4 Adding advection to the mean-field model

We now turn to the effect of advection on the filopodial growth due to myosin motors. The role of molecular motors in filopodial extension has been known from experiment for some time [Wang 96] but has not been successfully introduced to the mean-field system of equations. It should be mentioned in this connection that since starting the work contained in this chapter, simulation results for filopodial dynamics including the effect of motors have been published [Zhuravlev 10]. The authors use a spatial Gillespie algorithm but do not include any extension of the associated PDEs. As we will see below, our results from studying numerical simulations of our proposed PDEs agree qualitatively with those in [Zhuravlev 10].

We now wish to write down a set of mean-field equations that will account for the actin transport towards the tip via the motors. We assume that the fibres are uniformly covered by the motors and that diffusing G-actin will attach to these motors with a rate k_a. These attached monomers, whose concentration we denote by $c_a(x,t)$, can then be advected towards the tip with velocity $v_{\rm adv}$ where they will polymerise if there is room below the membrane. Attached actin can also detach, at a rate k_d, to rejoin the ranks of diffusing actin, whose concentration we now call $c_d(x,t)$.

We propose the following set of equations:

$$\frac{\partial c_a}{\partial t} = v_{\rm adv}\frac{\partial c_a}{\partial x} + Nk_{\rm a}c_d - k_{\rm d}c_a, \tag{6.18}$$

$$\frac{\partial c_d}{\partial t} = D\frac{\partial^2 c_d}{\partial x^2} - Nk_{\rm a}c_d + k_{\rm d}c_a, \tag{6.19}$$

$$\frac{\partial L}{\partial t} = \delta\left[k_{\rm on}e^{-\beta f\delta/N}c_d(L) + \frac{v_{\rm adv}\eta c_a(L)}{N}e^{-\beta f\delta/N} - k_{\rm off}\right] - v_{\rm retr}. \tag{6.20}$$

The first equation describes the motion of the attached G-actin: it is carried at rate $v_{\rm adv}$ towards the tip, and it can also be increased/decreased by attachment/detachment. The second equation is the diffusion equation considered above, albeit modified now by the added terms due to attachment and detachment rates. The attachment terms contain dependence on the number of fibres, N, as the overall sink from the diffusing G-actin due to attachment to the motors will be proportional to the number of fibres available to which they can attach. Similarly, the detachment terms are simply proportional to the density of attached actin, which already contains the N dependence without having to be added explicitly. The extra term in the ratchet equation accounts for the advected actin; we assume the attached actin will be limited by the same exponential factor at the tip as the diffusing actin as it will also have to wait for space for polymerisation to occur.

6.4.1 Boundary Conditions

We consider the following boundary conditions:

$$
\begin{aligned}
c_a(x=0,t) + c_d(x=0,t) &= c_0, && (6.21)\\
\frac{c_a(x=0,t)}{c_d(x=0,t)} &= N\frac{k_a}{k_d}, && (6.22)\\
-D\frac{\partial c_d}{\partial x}\bigg|_{L(t)} &= \left(\frac{N}{\eta\delta}\right)\frac{\mathrm{d}L}{\mathrm{d}t}\bigg|_{v_{\mathrm{retr}}=0}. && (6.23)
\end{aligned}
$$

The boundary conditions at $x = 0$, i.e. at the base of the filopodium, state that the attached and diffusing populations are in equilibrium, and that the total density is the typical bulk concentration of G-actin. On the other hand, the boundary condition at $L(t)$ once Eq. (6.20) is inserted states that there is a sink for the diffusing and advected G-actin, due to polymerisation. This sink generalises the purely diffusive one proposed in previous work [Mogilner 05, Lan 08].

Note that we do not include any exclusion interaction between the motors on the filopodium, this could be done by turning the advection equation into a Burgers equation with a reaction term [Proeme 11], by introducing c_a dependence into the advection velocity, for example:

$$\frac{\partial c_a}{\partial t} = v_{\mathrm{adv}}(1-c_a)\frac{\partial c_a}{\partial x} + Nk_{\mathrm{a}}c_d - k_{\mathrm{d}}c_a \tag{6.24}$$

Technical Aside: Lax Prescription

In order to simulate these equations numerically, we must be careful in particular when evaluating Eq. (6.18) as the advection term can render the density, $c_a(x,t)$, unstable. If we use the same Forward Time Centred Space (FTCS) methods as in previous numerical simulations, i.e. we discretise (ignoring k_d, K_a for the moment):

$$\frac{c_j^{n+1} - c_j^n}{\mathrm{d}t} = v_{\mathrm{adv}}\frac{c_{j+1}^n - c_{j-1}^n}{2\mathrm{d}x} \tag{6.25}$$

and attempt a stability analysis from Section 2.4.2 (inserting $u_j^n = \xi^n e^{ikj\mathrm{d}x}$ into Eq. (6.25)), we find:

$$\xi = 1 + \frac{iv_{\mathrm{adv}}\mathrm{d}t}{\mathrm{d}x}\sin(k\mathrm{d}x) \tag{6.26}$$

which is unstable ($|\xi(k)| > 1$) for all values of k, i.e. unconditionally unstable. The solution, given in [Press 92], is to use a different discretisation for the time derivative, specifically to replace the c_j^n term by its average:

$$c_j^n \to \frac{c_{j+1}^n + c_{j-1}^n}{2}. \tag{6.27}$$

The resulting discretisation becomes:

$$c_j^{n+1} = \frac{c_{j+1}^n + c_{j-1}^n}{2} + v_{\text{adv}} \mathrm{d}t \frac{c_{j+1}^n - c_{j-1}^n}{2\mathrm{d}x}. \tag{6.28}$$

Attempting the stability analysis again yields:

$$\xi = \cos(k\mathrm{d}x) + \frac{i v_{\text{adv}} \mathrm{d}t}{\mathrm{d}x} \sin(k\mathrm{d}x). \tag{6.29}$$

This gives the *Courant condition* [Press 92]:

$$\frac{|v|\mathrm{d}t}{\mathrm{d}x} \leq 1. \tag{6.30}$$

6.4.2 Results from Continuum Model

We have considerable freedom in choosing the attachment and detachment rates (k_a and k_d respectively), although this is limited by our choice of $\mathrm{d}t$ and $\mathrm{d}x$. However, we always ensure for simplicity that $Nk_a = k_d$ so that $c_d \sim c_a$ at the filopodial base, which is reasonable given the current knowledge of the biology [Nagy 08]. Our numerics essentially agrees with [Zhuravlev 10] in that advection generally hinders rather than helps filopodial growth. We find that reducing k_a, always keeping $Nk_a = k_d$, eventually creates a regime where diffusion no longer occurs, the length profile, $L(t)$, becomes straight and the system with advection can generate longer filopodia. Note that in [Zhuravlev 10], the authors are able to consider a much larger range of $k_d = 1 - 3000$ s^{-1}, but as we will see below, we require much smaller values of k_d in order to allow motors to aid filopodial growth. We now summarise our salient findings:

Advection *slows down* growth rate for realistic parameters

Considering first the physically unrealistic scenario where there is no retrograde flow, Figure 6.12 compares profiles for the filopodium length with time for the

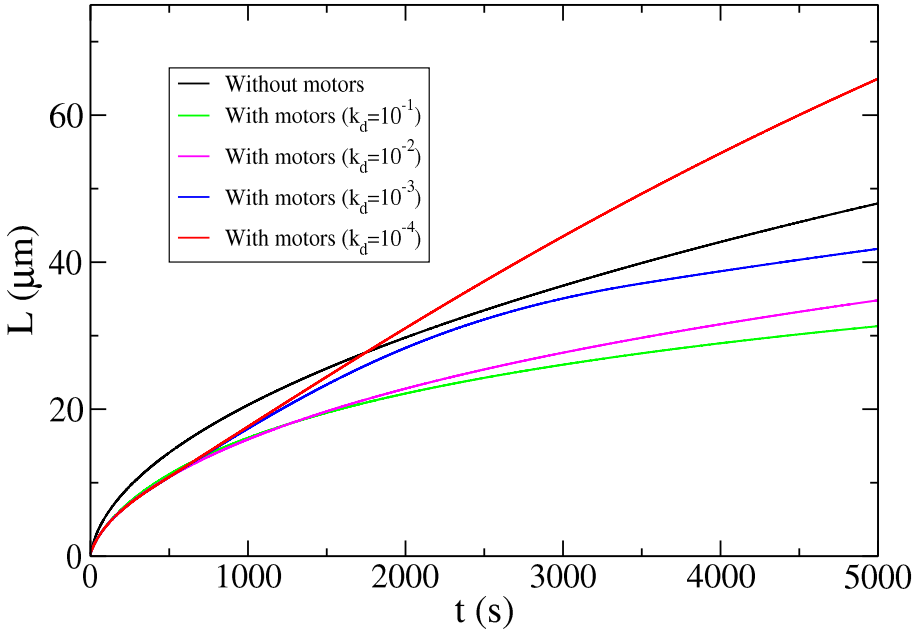

Figure 6.12: Filopodium length as a function of time from numerical integration of Eqs. (6.18) and (6.21). Initially, adding myosin motors slows down filopodial growth and, unless the detachment rate is very slow ($k_d \sim 10^{-4}$ s^{-1}), advection always results in shorter filopodia. Simulation parameters are $N = 10$, $f = 10$ pN, $k_{\text{off}} = 1$ s^{-1}, $a_0 = 10$ μM and $v_a dv = 1.25$ μm s^{-1}

system with and without myosin transport. We see that including advection actually slows down the growth at the start, in agreement with [Zhuravlev 10]. Although at first this may seem surprising, the reason can be appreciated by considering the initial growth rate coming from diffusion alone. This can be estimated as

$$\left[k_{\text{on}} c_0 e^{-\beta f \delta/N} - k_{\text{off}}\right] \delta \sim \left[100 \times e^{-0.66} - 1\right] 2.7 nms^{-1} \sim 135 \text{nms}^{-1} \tag{6.31}$$

and should be compared with the initial growth rate driven by motor advection as well:

$$\begin{aligned} &\left[k_{\text{on}} c_d(0) e^{-\beta f \delta/N} + \frac{v_{\text{adv}} c_a(0) e^{-\beta f \delta/N} \eta}{N} - k_{\text{off}}\right] \delta \\ &\sim \left[50 \times e^{-0.66} \times \frac{1 \times 5 e^{-0.66} \times 18.9}{10} - 1\right] 2.7 \text{nms}^{-1} \sim 30 \text{nms}^{-1}. \end{aligned} \tag{6.32}$$

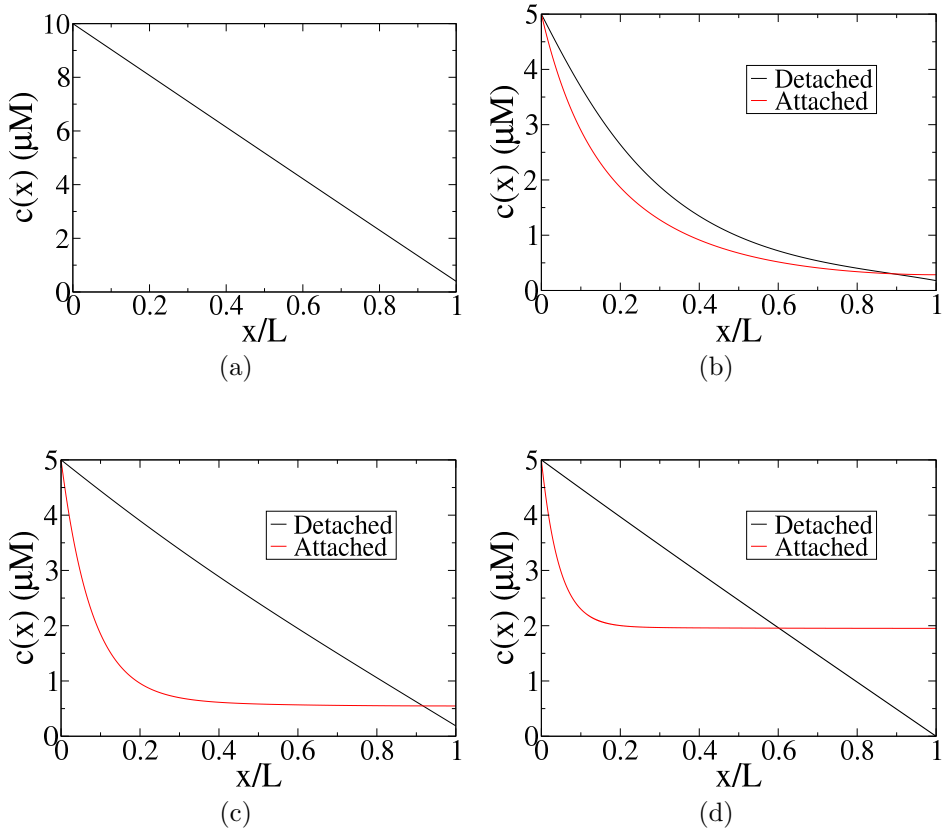

Figure 6.13: Actin density as a function of distance from the base, (a) shows the density profile of a growing filopodium without motors. (b), (c) and (d) give both attached and detached concentrations (red and black lines respectively) in the presence of motor transport when $k_d = 10^{-1}$, 10^{-3}, 10^{-4} s^{-1}.

Furthermore, in the long term, motors generally yield smaller filopodia unless k_a, k_d are very low ($k_d \sim 10^{-4}$ s^{-1}). We might understand this better by looking at the density profiles in Figure 6.13. We see that in the presence of motors, when k_a, k_d are large, the density profile for detached G-actin is no longer linear when k_d is large. We also see that, apart from at the base where the boundary condition ensures that the overall actin concentration is equally distributed among attached and detached G-actin, as k_d is decreased, the concentration of detached actin at the tip is reduced until a regime is reached where all of the actin polymerisation is due to the advecting motors. This is the region where we observe linear growth of the filopodium, which allows the length to become greater than the steady state length observed via diffusion alone (see below).

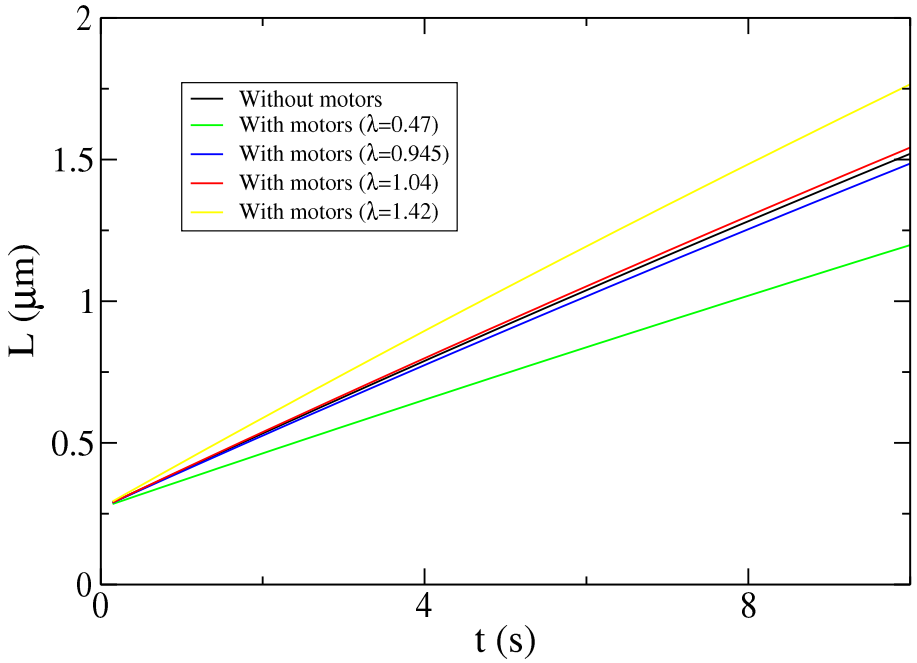

Figure 6.14: Filopodium length as a function of time from numerical integration of Eqs. (6.18) and (6.21). Tuning the dimensionless parameter $\lambda = 0.42, 0.945, 1.04, 1.42$ in order to compare the initial growth rate with the case without motors. Simulation parameters are $N = 2$, $f = 2$ pN, $k_{\text{off}} = 1\ \text{s}^{-1}$, $a_0 = 10\ \mu$M, v_{adv} is varied in the range $0.5 - 1.5\ \mu\text{m s}^{-1}$

It is possible to tune the parameters so that initial growth is faster with advection but simulations with $k_a = 0$ (no motors) will still usually produce longer filopodia eventually. For the system with advection to start growing faster, we require the following condition:

$$k_{\text{on}} c_d(0) + \frac{v_{\text{adv}} c_a(0) \eta}{N} > k_{\text{on}} c_0. \tag{6.33}$$

Using the boundary conditions Eqs. (6.21) and (6.22), and re-arranging a little, we obtain the following dimensionless number:

$$\lambda = \frac{v_{\text{adv}} \eta}{N k_{\text{on}}}. \tag{6.34}$$

If $\lambda > 1$, the initial growth will be greater with motors, as confirmed by Figure 6.14.

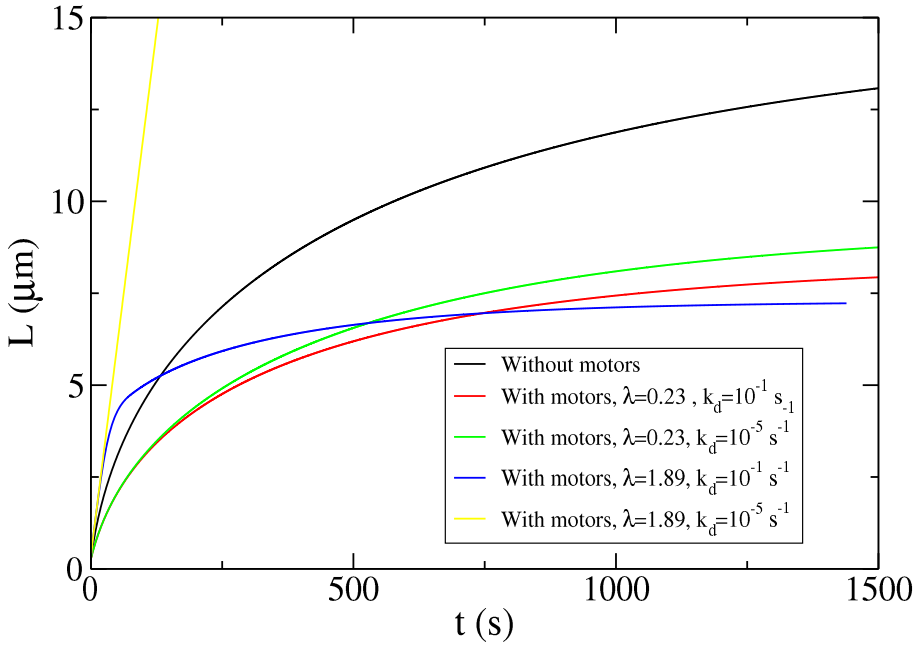

Figure 6.15: Filopodium length as a function of time from numerical integration of Eqs. (6.18) and (6.21). With $v_{\text{retr}} = 15$ nm s^{-1}, the system can reach a steady state. In general, including myosin transport results in a shorter steady-state length. We show two extreme values of $k_d = 10^{-1}, 10^{-5}$ s^{-1} for $\lambda = 0.23, 1.89$ in green, red and yellow, blue respectively. If $\lambda < 1$, k_d has little effect. If however, $\lambda > 1$, the strength of attachment/detachment dictates whether or not steady state is reached at all. Simulation parameters are $N = 10$, $f = 10$ pN, $k_{\text{off}} = 1$ s^{-1}, $a_0 = 10$ μM, $v_{\text{adv}} = 1.25, 10$ μm s^{-1}

With retrograde flow, advection induces *shorter* steady state lengths

As before, when considering filopodial growth without motors, we find that retrograde flow is crucial in allowing the system to reach a steady state length. In Figure 6.15, we find that in the region where including advection slows down the growth ($\lambda < 1$), the steady-state length reached is reduced considerably by the motors. Indeed, we now find that varying the attachment/detachment rates now makes very little difference to the length that is achieved. The case when $\lambda > 1$ is interesting, where we see that if k_d is large, so that the diffusion part makes an impact on the advection, slowing the growth, the steady-state length is similar to when $\lambda < 1$. If, however, k_d is small enough, the diffusion becomes irrelevant. Sequestration of G-actin by the fibres ensures that all of the actin monomers at the tip have reached there by advection. Steady state can now

k_d (s^{-1})	v_r(μm s^{-1})	θ
10^{-1}	0.0165	42.83
10^{-2}	0.0165	13.54
10^{-3}	0.0165	4.28
10^{-4}	0.0165	1.35

Table 6.3: Dimensionless number θ for simulation values in Figure 6.12

k_d (s^{-1})	v_r(μm s^{-1})	θ
10^{-1}	0.0165	468.76
10^{-1}	0.132	6.04
10^{-5}	0.0165	4.69
10^{-5}	0.132	0.06

Table 6.4: Dimensionless number θ for simulation values in Figure6.15

no longer be reached, presumably until the retrograde flow is increased enough that it can compete with the ratchet velocity, v_{r}, (see Eq. (6.36)). We propose the following dimensionless number, effectively the ratio of the average diffusion length $\sqrt{D/Nk_a}$ and average advection path length, v_r/k_d:

$$\theta = \sqrt{\frac{D}{Nk_a}}\left(\frac{k_d}{v_r}\right) \tag{6.35}$$

where v_r is the velocity of the ratchet (the motors will move as the filopodium grows):

$$v_r = \delta\frac{v_{\mathrm{adv}}\eta c_a(0)}{N}e^{-\beta f\delta/N} - v_{\mathrm{retr}}. \tag{6.36}$$

Tables 6.3 and 6.4 show values of θ for the curves in Figures 6.12 and 6.15 respectively. We see that θ is a good indicator of whether motors will help ($\theta < 1$) or hinder ($\theta > 1$) filopodial growth at large times.

Effects of the diffusion rate

Even when the attachment/detachment rates are low enough that the system with motors can eventually 'win', it usually overtakes the system without myosin at a filopodium length $L >> 10$ μm, well after strongly non-linear elastic effects will have invalidated our set of PDEs. It is, however, possible that the diffusion constant $D = 5$ μ^2 s^{-1} has been generally over-estimated in the literature, where in vitro experiments would not account for the level of macromolecular crowding that might be occurring in vivo [Ellis 01]. If this were the case, advection might become more relevant. In Figure 6.16, we see that with $D = 0.5$ μ^2 s^{-1} and a small detachment rate $k_d = 10^{-5}$ s^{-1}, the system with advection takes over around $L \sim 2.5$ μm. This represents a ten-fold decrease in the crossover point from the previous case when $D = 5$ μ^2 s^{-1}, and shows that given the right

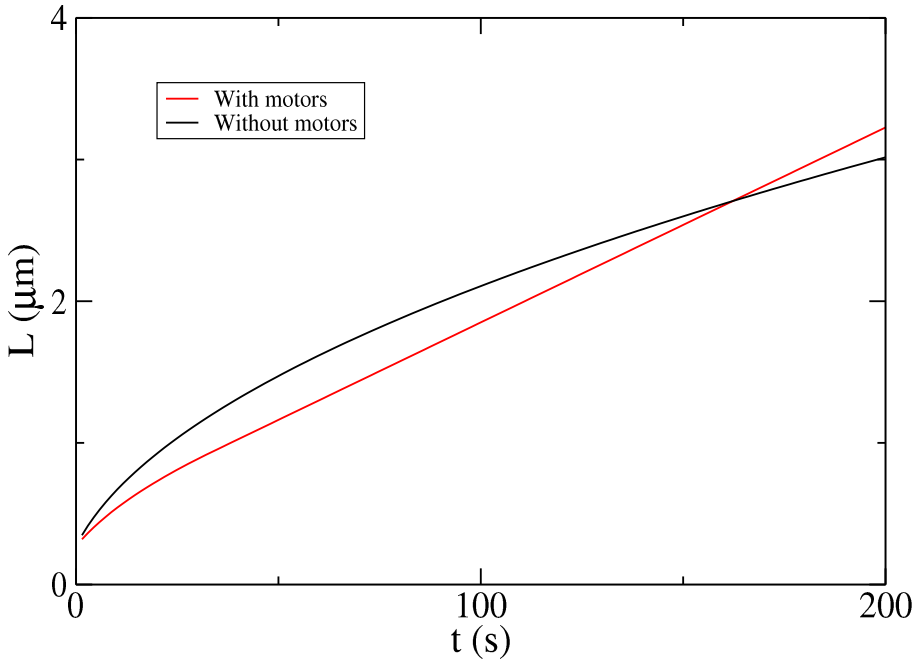

Figure 6.16: Filopodium length as a function of time from numerical integration of Eqs. (6.18) and (6.21). Reducing the diffusion constant to $D = 0.5\ \mu^2\ \mathrm{s}^{-1}$ can make the myosin motors much more relevant as the crossover point is now at $L \sim 2.5\ \mu\mathrm{m}$. Simulation parameters are $N = 10$, $f = 10$ pN, $k_{\mathrm{off}} = 1\ \mathrm{s}^{-1}$, $a_0 = 10\ \mu\mathrm{M}$, $v_{\mathrm{adv}} = 1.25\ \mu\mathrm{m\ s}^{-1}$

parameters, it is possible for the myosin motors to have a positive effect on filopodial growth.

6.5 Conclusions

We began this chapter by considering the existing model for filopodial growth. We developed a fully agent-based simulation in order to test the validity of the PDEs, particularly whether non-mean-field effects, which would be present in the simulation, are important to the dynamics. We found that the agreement was generally very good although the behaviour in the presence of the membrane resistance force showed some quantitative differences. This may be due to the strong mean-field assumptions borne out of extending the Brownian ratchet equation to model a bundle of fibres, but may also be due to the relatively simple algorithm employed to model the diffusion of the membrane. Further work on the agent-based model would almost certainly have to include alternative

implementations of the membrane resistance, perhaps a method involving sampling the probability distribution for the positions directly and therefore not rejecting any moves at all. Rejection of proposed membrane moves can "renormalise" time in Monte Carlo simulations [Sanz 10]. Altering the membrane step length, $\mathrm{d}l_\mathrm{m}$, whilst holding its diffusion rate constant was found to have little to no effect on this problem.

Having reassured ourselves of the validity of the mean-field model, we then attempt to extend it by including the action of directed transport via myosin motors, effectively introducing an advective term into the set of partial differential equations. Our model is simpler to that simulated in [Zhuravlev 10], where the authors allow the motors to diffuse freely and attach/detach to the fibres as well as load/unload actin, and much faster to simulate, consisting simply of numerical integration of a set of PDEs. Our basic result however remains the same: for realistic parameters myosin motors hinder rather than help filopodial growth. This result is sensitive to the various parameters involved, especially to the choice of k_d, k_a, which are not known in real systems, and the system can be tuned so that advection does make a significant impact on the growth. It is unlikely that cells fine-tune their parameters to the extent as to control whether or not the motors help or hinder the growth but it is quite possible that some of the values that are generally used are not entirely correct. For example, we saw that the diffusion constant, when reduced, allows the motors to play a more important role in the growth and overtake the system without transport at relatively small lengths.

We also propose two dimensionless numbers, λ and θ, which help to predict whether the initial growth when including directed transport will be faster than without and whether the length of the filopodium at large times will be greater, respectively. Finally, the various values are usually given within quite a broad range from experiments, with different authors choosing to define their terms quite differently. For example, Mogilner et al. choose to include the advancing lamellipodium in the retrograde flow and set $v_\mathrm{retr} = 70$ nm s^{-1} whereas we use the more conservative value of v_retr from [Gardel 08]. If our constants are essentially correct, then our results point to factors other than actin-transporting myosin motors to explain observed filopodial lengths; perhaps the motors are still important, as experiments in [Wang 96] appear to indicate, but also have a role in carrying other materials to the tip complex, such as uncapping proteins,

which we have not considered here.

6.6 Possible future extensions

Although the agent-based simulation contains the most microscopic details of any filopodial dynamics simulation of which we are aware, it could be further enhanced by the inclusion of other processes. For example, we model the membrane tip as a flat plate whereas in reality, it will deform around the contour of the tip complex having a different distance and more complicated resistance force in the vicinity of each fibre. This is considered in more detail in [Lan 08]. Another way of bringing the simulation closer to reality would be to allow the fibres to move and bend allowing more complicated patterns of growth. Finally, the role of myosin motors in transporting actin to the tip is well-supported experimentally [Wang 96] and future extensions to this work would include adding this effect to the agent-based simulation and comparing with the mean-field results above.

Other processes that could be included in the PDEs and the agent-based simulation are motor attachment/detachment as modelled in [Zhuravlev 10], and an exclusion interaction between the motors on the filopodium track, which could be achieved by turning the advection equation into a Burgers equation with a reaction term [Proeme 11].

Chapter 7

Conclusions

In this thesis we have explored the effect of advection on a number of systems of relevance to the physics of "active matter" and to biological physics, namely the sedimentation of reproducing bacteria (with and without noise in their population dynamics) and the growth of filopodial protrusions in the presence of molecular motors. Advection has the power to change dynamics completely, as can be appreciated by considering the case of transport within a fluid. If diffusion alone is present, this means that the time for a particle to travel a distance L will scale as L^2. If, however, a convective flow is present and advects the particle, this allows a much more efficient transport, taking a time proportional to L instead. We first studied the effect of adding a gradient term to the celebrated Fisher-Kolmogoroff Petrovsky Piscounoff (F-KPP) equation, used to model many systems that incorporate birth/death processes into diffusive motion. We found that in the presence of no-flux boundaries, essentially modelling sedimentation of active particles in a container, the gravitational advection term leads to sedimentation and that this sedimentation competes with the so-called 'Fisher wave' that grows out and seeks to spread the particles throughout the system. There is now a discontinuous non-equilibrium phase transition between the regime where sedimentation 'wins', primarily an exponential profile, and when the Fisher velocity, v_f, is dominant, where the density is virtually constant throughout the system. The transition is controlled by a dimensionless parameter $\lambda = D\alpha/v_2$, with D the diffusion constant, α controls the growth term and v is the advection strength. The critical value $\lambda = \frac{1}{4}$ directly expresses the contest between v and v_f, as the selection principle gives

$v_f = 2\sqrt{D\alpha}$.

It is noteworthy that boundary conditions are crucial for the very existence of this transition. If, for example, we had used periodic boundary conditions (instead of no-flux), then we can show that the advection field is inconsequential: transforming into a reference frame co-moving with v will restore F-KPP albeit with a reduced Fisher velocity [Saarloos 03]. The fixed boundaries that we employed negate the possibility of making this transformation and hence the advection is very important in our system. This is in fact a characteristic of non-equilibrium systems: whereas for most equilibrium systems boundaries are not expected to affect the critical behaviour, in a non-equilibrium system boundaries are known to play a crucial role in determining phase transitions [Mukamel 00].

Our choice of boundaries reflected a real-world model and we also discussed the possibility of observing the transition in experiment. In principle, the typical values of v and D in a suspension of *E. coli* will allow the possibility of 'tuning' the growth constant α to bring the system from the sedimentation to the uniform regime according to our predictions. In reality, these experiments however will require stringent controls, e.g. to make sure that the bacteria are not engaged in any form of chemotaxis, which would render D dependent on concentrations of chemical species (nutrient, oxygen, waste products, . . .). The extra level of complexity introduced could be modelled by adding a "chemotactic" term to Eq. (3.20), and coupling it to a reaction-diffusion equation, e.g. as in the Keller-Segel model [Keller 71]. Furthermore, we have shown that the timescales for reaching steady state can be extremely long in the vicinity of the transition (Figure 3.9), but in a bacterial culture, α itself is only approximately constant during what is known as the exponential growth phase, after which saturation in population density and then death follow. Thus, steady-state experiments at $\theta \approx \theta_c$ would likely be impractical. Even experiments involving sedimentation only can take a long time with real bacteria, but there have been advances in microfluidics [Palacci 10, Enculescu 11] that look promising. Chemically-powered colloids can be used to observe sedimentation of active particles, environmental factors are much easier to control, and the timescales involved are far shorter than when using real bacteria.

When we introduced noise, it needed to be multiplicative in order to respect the absorbing state, i.e. the noise must be zero when the density is zero. The

resulting equation was very close to Directed Percolation [Henkel 08], which represents arguably the most successful universality class of non-equilibrium phase transitions to date. Furthermore, this universality class describes absorbing-state phase transitions which are inherently far from equilibrium as they violate detailed balance (the absorbing state is a sink for the dynamics). We found that, whereas DP-like phase transitions are usually quite robust to changes in the dynamics, adding an advection term, no matter how weak, changes the character of the transition from a continuous to a discontinuous one, thus lifting the system out of the DP class. The resulting Langevin equation was found to have two interesting limits: DP is restored by taking the advection strength to zero, and F-KPP with advection is found by taking the noise strength to zero. In Figure 5.1, we mapped out a phase diagram describing their location in the $v - \Gamma_0$ parameter plane. There were also several other regions of interest in the phase diagram. The 'bands' observed in F-KPP with advection, a finite-size effect occurring in the vicinity of the transition, were now found to become mobile, to diffuse, and perform a random walk throughout the system when the noise strength, Γ_0, was small. Furthermore, there were now two low-density phases, the exponential profile, now metastable, and the absorbing state, although both will become absorbed in the infinite-time limit. We also analysed the dynamical phase transition that separates these two regions.

By considering an alternative form for the multiplicative noise in the DP Langevin equation, we illustrated that the type of noise used to model non-equilibrium phase transitions can *control* the kind of transitions observed. Switching from square root to linear noise produced a true phase transition out of the dynamical transition, effectively stabilising the previously metastable state. In addition to this, it appeared that a large portion of the critical line had changed from discontinuous to continuous, although more extensive simulations would be required to confirm this. This important quantitative and qualitative difference highlighted once again (see [Munoz 98] for another example) that care should be exercised when deriving fluctuating hydrodynamic equations for non-equilibrium models, as the very form of the noise, which is sometimes overlooked, may drive unexpected changes in the physics of the system.

Finally, we considered filopodial protrusion, an intriguing system involving self-assembled actin fibres pushing forth from eukaryotic cell bodies. This time the 'activity' came from fibre polymerisation and depolymerisation at their ends

and furthermore actin polymerisation is at the heart of cell motility. After developing a detailed agent-based simulation, which could be extended in future to incorporate further processes involved in filopodial growth, we confirmed the validity of the diffusion-limited model put forward in [Mogilner 05]. Unfortunately, this set of PDEs does not reflect the length scales observed in real filopodia and attempts to extend the existing model to account for this discrepancy is ongoing. We proposed that a missing ingredient to make contact with the observed data may be provided by the directed transport of actin to the tip by myosin motors. This may indeed have allowed for longer filopodia as actin could now be carried directly to the tip, which could have provided a faster route to growth than diffusion. We extended the set of PDEs to account for this new advection term and explore the behaviour of this new system using numerical simulations of the PDEs. We found, in agreement with [Zhuravlev 10] where the authors use Monte Carlo methods to investigate the same principle, that advection in general *does not* help with filopodial growth. In fact, for most choices of the various parameters, directed transport actually *hinders* the growth. We tried to shed light on this potentially counter-intuitive result by considering the initial growth rates and found a dimensionless parameter in Section 6.4.2 that controls whether a given system will start growing faster with or without motors. This is the ratio between two typical velocities, one linked with polymerisation only, and the other the advection via motors as well.

As in the case without myosin motors, the system can never reach a steady state in the absence of a retrograde flow velocity, v_{retr}, which arises as a reaction to the fibres pushing on the membrane, and yields a force that moves the filaments back towards the cell body [Lin 95]. We found that in the presence of this retrograde flow, the filopodia typically grew to shorter steady-state lengths when motors are included. This result is sensitive to the actin detachment/attachment rates to the motors, as well as the motor speed along the filaments. Finally, we give another dimensionless number in section 6.4.2: a ratio between the length actin will diffuse while detached and the length travelled when carried by the motors. This number can give a rough guide as to whether the steady-state length will be improved by the addition of motors or not. The dependence of this number on the diffusion constant, D, highlighted the possibility that motors could still be advantageous to growth in real systems, as it is possible that this parameter has been over-estimated in the literature, due

to macromolecular crowding. More experiments are necessary to provide better estimates of all the parameters involved before a conclusion can be drawn. If, however, the parameters are correct, we have then shown that there must be more factors that help with filopodial growth. For instance, motors, which are known to be involved experimentally [Wang 96], might be carrying other molecules to the tip, such as uncapping proteins, which we do not consider in our treatment.

This thesis contains several avenues for further exploration. First, bacterial sedimentation could be extended in several ways. We already mentioned above the possibility of including a chemotactic term, which would almost certainly yield interesting behaviour; the model could also be extended to higher dimensions, and fronts could also then be considered. More work could be carried out on the phase portrait of the Langevin equation with linear noise Eq. (4.7), analysing the apparently continuous transition in more detail and characterising the tri-critical point. The agent-based simulation of filopodial dynamics could also be extended; there are many more effects to be considered, such as fibre bending [Daniels 06], capping/uncapping proteins [Daniels 10], as well as a more detailed description of the membrane at the tip, such as is done in [Lan 08]. Of course, it would also be interesting to add the effect of myosin motors to the simulation, and therefore test our system of PDEs in more detail, as we have done with the system from [Mogilner 05]. Both the agent-based and continuum models could then be improved by considering motor detachment/attachment as well as loading/unloading introducing another degree of freedom into the system, although this might be challenging within the serial simulation framework used in this thesis. Finally, there is of course a plethora of existing models that could be introduced to an advection term, the three models we have considered have yielded rich behaviour under this addition, and it would be interesting to study other systems in the same way.

To summarise, we have seen that in the case of non-equilibrium models, such as active and biological systems, flow and advection have a major impact on the observed behaviour. In addition to this, the form of noise used, which can sometimes be overlooked, will also drive important changes in the physics. We looked at two models that are of theoretical interest in statistical physics as well as one biological system which is currently being studied by researchers in a number of different fields. We hoped that molecular motors may hold the

key to explaining the diverse range of filopodial lengths seen in nature, and although this appears not to be the case, we have made an improvement on the existing diffusion-limited model for filopodial protrusion.

Appendix A

Equivalence of Langevin and Microscopic Descriptions for DP

Consider a diffusion process coupled with the following reaction rules:

$$\begin{aligned} A &\xrightarrow{\alpha} A + A, \\ A + A &\xrightarrow{\beta} \emptyset. \end{aligned} \tag{A.1}$$

This system will exhibit a DP-like phase transition (Chapter 4) and its fluctuating hydrodynamic equation can be written in the following Langevin form:

$$\dot{\rho} = D\Delta\rho + \alpha\rho - \beta\rho^2 + \sqrt{2\Gamma\rho}\eta \tag{A.2}$$

where η is a spatio-temporal Gaussian white noise whose variance:

$$< \eta(x,t)\eta(x',t') >= \delta(x-x')\delta(t-t'). \tag{A.3}$$

Without any further explanation, this equation is usually attributed to Janssen [Janssen 81] and I therefore wish to address this gap in the literature by offering a sketch of the justification here. The strategy is to derive an associated field theory for both the Langevin process and the microscopic dynamics in Eq. (A.1) and show their equivalence. As we will show below, the probability to observe the time-dependent evolution of the density $\rho(x,t)$ of the large scale behaviour

of Eq. (A.1) and of Eq. (A.2) can be put in the following form:

$$\mathcal{P}[\rho(x,t)] = \int \mathcal{D}[\hat{\rho}] \exp[-\mathcal{S}] \tag{A.4}$$

and two theories are deemed equivalent if their actions, S, can be shown to be the same. We begin with the Langevin form.

A.1 Field Theory for Langevin DP

Defining the probability of a trajectory $\rho(x,t)$ as $\mathcal{P}[\rho]$, we evaluate $\mathcal{P}$ as the path integral over all realisations of $\eta(x,t)$ such that $\rho(x,t)$ is constrained to obey Eq. (A.2):

$$\mathcal{P}[\rho(x,t)] \propto \int \mathcal{D}[\eta(x,t)]\delta(\dot{\rho} - D\delta\rho - \alpha\rho + \beta\rho^2 - \sqrt{2\Gamma\rho}\eta)\mathcal{P}[\eta(x,t)] \tag{A.5}$$

where the δ-function is in the space of trajectories $\rho(x,t)$ and should be understood as comprising of a δ at every point in time and space. It can be defined by:

$$\int \mathcal{D}[\rho(x,t)]\delta[\rho(x,t) - \rho_0(x,t)]\mathcal{F}[\rho(x,t)] = \mathcal{F}[\rho_0(x,t)]. \tag{A.6}$$

As usual, it is easier to work with the complex integral representation of the δ-function and doing so introduces the imaginary field, $\hat{\rho}$:

$$\begin{aligned}\mathcal{P}[\rho(x,t)] = &\int \mathcal{D}[\eta(x,t), \hat{\rho}(x,t)] \\ &\times \exp\left(-\int \mathrm{d}t\mathrm{d}x\hat{\rho}(\dot{\rho} - D\Delta\rho - \alpha\rho + \beta\rho^2 - \sqrt{2\Gamma}\eta)\right) \\ &\times \exp\left(-\int \mathrm{d}x\mathrm{d}t\frac{\eta^2}{2}\right)\end{aligned} \tag{A.7}$$

where we have also written the Gaussian weight explicitly. We now use Hubbard-Stratonovich for functional integrals:

$$\int \mathcal{D}[\eta(x,t)] \exp\left(-\int \mathrm{d}t\mathrm{d}x\frac{a(x,t)\eta^2(x,t)}{2} - b(x,t)\eta(x,t)\right) \propto \exp\left(\int \mathrm{d}t\mathrm{d}x\frac{b^2(x,t)}{2a(x,t)}\right). \tag{A.8}$$

In our case, $a(x,t) = 1$ and $b(x,t) = -\hat{\rho}(x,t)\sqrt{2\Gamma\rho(x,t)}$ so we write:

$$\mathcal{P}[\rho(x,t)] = \int \mathcal{D}[\hat{\rho}(x,t)] \exp\left(-\int \mathrm{d}t\mathrm{d}x \left[\hat{\rho}\dot{\rho} - D\hat{\rho}\Delta\rho - \alpha\rho\hat{\rho} + \beta\hat{\rho}\rho^2 - \hat{\rho}^2\Gamma\rho\right]\right) \tag{A.9}$$

i.e. we have cast the probability in the form $\mathcal{P} = \int \mathcal{D}[\hat{\rho}] \exp[-\mathcal{S}]$, and the action $\mathcal{S}$ is given by

$$\mathcal{S} = \int \mathrm{d}t\mathrm{d}x \left[\hat{\rho}\dot{\rho} - D\hat{\rho}\Delta\rho - \alpha\rho\hat{\rho} + \beta\hat{\rho}\rho^2 - \hat{\rho}^2\Gamma\rho\right]. \tag{A.10}$$

The reader should note that it is more traditional to use Doi-Peliti fields ϕ and $\hat{\phi}$, which can be related to ours above via a Cole-Hopf transformation [Tailleur 08], $\rho = \phi\hat{\phi}$ and $\hat{\rho} = -\ln\hat{\phi}$. ϕ and $\hat{\phi}$ are more suitable for problems that contain no interactions, which is not the case here.

A.2 Field Theory for the Microscopic Model

To derive the action functional of the microscopic system described by Eq. (A.1), we follow [Thompson 11]. We write an array of occupation numbers $\underline{n}(t)$, its probability distribution can be written:

$$P(\underline{n}(t)) \propto \prod_t \langle \delta(\underline{n}(t+\mathrm{d}t) - \underline{n}(t) - \underline{J})\rangle_{\underline{J}} \tag{A.11}$$

where $J_i = n_i(t+\mathrm{d}t) - n_i(t)$ is a random variable; introducing the indices explicitly:

$$P(\underline{n}(t)) = \prod_t \langle \prod_i \delta(n_i(t+\mathrm{d}t) - n_i(t) - J_i)\rangle_{J_j}. \tag{A.12}$$

We now use the same trick as above, and introduce $\underline{\hat{n}}(t)$:

$$\begin{aligned} P(\underline{n}(t)) &= \int \prod_t \left(\prod_i \mathrm{d}\hat{n}_i(t)\right) \langle \prod_i \mathrm{e}^{-\hat{n}_i(n_i(t+\mathrm{d}t)-n_i(t)) + \hat{n}_i J_i}\rangle_{J_j} && \text{(A.13)} \\ &= \int \prod_t \left(\prod_i \mathrm{d}\hat{n}_i(t)\right) \mathrm{e}^{-\sum_i \hat{n}_i(n_i(t+\mathrm{d}t)-n_i(t))} \langle \mathrm{e}^{\sum_i \hat{n}_i J_i}\rangle_{J_j} && \text{(A.14)} \\ &= \int \mathcal{D}\left[\hat{n}(t)\right] \mathrm{e}^{-\sum_i \int \mathrm{d}t \hat{n}_i \dot{n}_i} \prod_t \langle \mathrm{e}^{\sum_i \hat{n}_i J_i}\rangle_{J_j} && \text{(A.15)} \end{aligned}$$

where in the first step, we pull the $\exp(\hat{n}_i(n_i(t+\mathrm{d}t)-n_i(t)))$ out of the average as it does not depend on J, and we have moved into continuous time in the second step. In order to compute the average $\langle \mathrm{e}^{\sum_i \hat{n}_i J_i}\rangle_{J_j}$ in the above, we consider each possible outcome in turn:

- Particle diffuses from $i \xrightarrow{D} i+1$:

$$\left.\begin{array}{ll} n_i(t+\mathrm{d}t)-n_i(t)=-1 & \to J_i=-1 \\ n_{i+1}(t+\mathrm{d}t)-n_{i+1}(t)=1 & \to J_{i+1}=1 \end{array}\right\} \text{probability } Dn_i\mathrm{d}t \tag{A.16}$$

  and similarly, diffusion $i+1 \xrightarrow{D} i$ gives $J_i=1$, $J_{i+1}=-1$ with probability $Dn_{i+1}\mathrm{d}t$. Note that $J_j=0$ for all $j\neq i, i+1$ as we are considering probabilities up to order $\mathrm{d}t$ only.

- Particle multiplies: $J_i=1$ with probability $\alpha n_i \mathrm{d}t$.

- Particles annihilate: $J_i=-2$ with probability $\frac{\beta n_i^2}{2}\mathrm{d}t$ (The rate at which annihilation occurs is $\beta\mathrm{d}t$ and this occurs $n_i(n_i-1)/2$ times at site i, finally we assume n_i large).

- Nothing happens: $J_i=0$ with probability $1-D(n_i+n_{i+1})\mathrm{d}t-\alpha n_i\mathrm{d}t-\frac{\beta n_i^2}{2}\mathrm{d}t$.

Putting it together:

$$\begin{aligned} \langle \mathrm{e}^{\sum_i \hat{n}_i J_i}\rangle_{J_j} &= \left(\mathrm{e}^{\hat{n}_{i+1}-\hat{n}_i}-1\right) Dn_i\mathrm{d}t + \left(\mathrm{e}^{\hat{n}_i-\hat{n}_{i+1}}-1\right) Dn_{i+1}\mathrm{d}t \\ &+ \left(\mathrm{e}^{\hat{n}_i}-1\right)\alpha n_i\mathrm{d}t + \left(\mathrm{e}^{-2\hat{n}_i}-1\right)\frac{\beta}{2}n_i^2\mathrm{d}t + 1 \qquad \text{(A.17)} \\ &= \exp\Big[\left(\mathrm{e}^{\hat{n}_{i+1}-\hat{n}_i}-1\right) Dn_i\mathrm{d}t + \left(\mathrm{e}^{\hat{n}_i-\hat{n}_{i+1}}-1\right) Dn_{i+1}\mathrm{d}t \\ &+ \left(\mathrm{e}^{\hat{n}_i}-1\right)\alpha n_i\mathrm{d}t + \left(\mathrm{e}^{-2\hat{n}_i}-1\right)\frac{\beta}{2}n_i^2\mathrm{d}t\Big] \qquad \text{(A.18)} \end{aligned}$$

where in the second step we used the approximation $\exp(k\mathrm{d}t)\approx 1+k\mathrm{d}t$.

Inserting now Eq. (A.18) into Eq. (A.15), we find the probability in the form $P[\underline{n}(t)]=\int[\mathcal{D}\hat{n}(t)]\exp\left[-S(n_i,\hat{n}_i)\right]$, with the action:

$$\begin{aligned} S(n_i,\hat{n}_i) &= \int \mathrm{d}t \sum_i \Big[\hat{n}_i\dot{n}_i - \left(\mathrm{e}^{\hat{n}_{i+1}-\hat{n}_i}-1\right) Dn_i - \left(\mathrm{e}^{\hat{n}_i-\hat{n}_{i+1}}-1\right) Dn_{i+1} \\ &- \left(\mathrm{e}^{\hat{n}_i}-1\right)\alpha n_i - \left(\mathrm{e}^{-2\hat{n}_i}-1\right)\frac{\beta}{2}n_i^2\Big]. \qquad \text{(A.19)} \end{aligned}$$

Now, we take the continuum limit, i.e. we set $O_{i+1} - O_i = \frac{1}{L}\nabla O + \frac{1}{2}\frac{1}{L^2}\nabla^2 O$, where O is any observable, and $\sum_i \to L\int_0^1 \mathrm{d}x$. We also rescale the fields:

$$\begin{aligned} n_i &= \rho L^\gamma, \\ \hat{n}_i &= \hat{\rho} L^\delta, \\ t &= tL^z. \end{aligned} \tag{A.20}$$

This gives:

$$\begin{aligned} S = \int \mathrm{d}t L^z . L \int \mathrm{d}x \Big\{ & L^\delta \hat{\rho} L^{\gamma - z} \dot{\rho} - L^\gamma \rho D \left(e^{L^{\delta-1}\nabla\hat{\rho} + \frac{1}{2}L^{\delta-2}\nabla^2\hat{\rho}} - 1 \right) \\ & - DL^\gamma \left(\rho + \frac{1}{L}\nabla\rho + \frac{1}{2L^2}\nabla^2\rho \right) \left(e^{-L^{\delta-1}\nabla\hat{\rho} - \frac{1}{2}L^{\delta-2}\nabla^2\hat{\rho}} - 1 \right) \\ & - \alpha L^\gamma \rho \left(e^{L^\delta \hat{\rho}} - 1 \right) - \frac{\beta}{2} L^{2\gamma} \rho^2 \left(e^{2L^\delta \hat{\rho}} - 1 \right) \Big\}. \end{aligned} \tag{A.21}$$

We expand the exponentials, anticipating that we will only retain gradients up to second order:

$$\begin{aligned} S = \int \mathrm{d}t \mathrm{d}x \Big\{ & L^{\delta+\gamma+1} \hat{\rho}\dot{\rho} - L^{\gamma+z+1} D\rho \left(L^{\delta-1}\nabla\hat{\rho} + \frac{1}{2}L^{\delta-2}\nabla^2\hat{\rho} + \frac{1}{2}L^{2\delta-2}(\nabla\hat{\rho})^2 \right) \\ & - L^{\gamma+z+1} D \left(\rho + \frac{1}{L}\nabla\rho + \frac{1}{2L^2}\nabla^2\rho \right) \left(-L^{\delta-1}\nabla\hat{\rho} - \frac{1}{2}L^{\delta-2}\nabla^2\hat{\rho} + \frac{1}{2}L^{2\delta-2}(\nabla\hat{\rho})^2 \right) \\ & - L^{\gamma+z+1}\alpha\rho \left(L^\delta\hat{\rho} + \frac{1}{2}L^{2\delta}\hat{\rho}^2 \right) - L^{2\gamma+z+1}\frac{\beta}{2}\rho^2 \left(-2L^\delta\hat{\rho} + \frac{1}{2}L^{2\delta}\hat{\rho}^2 \right) \Big\} \end{aligned} \tag{A.22}$$

and re-arranging, some of the terms cancel, leaving:

$$\begin{aligned} S = \int \mathrm{d}t \mathrm{d}x \Big\{ & L^{\delta+\gamma+1}\hat{\rho}\dot{\rho} + L^{\gamma+\delta+z-1} D \nabla\rho\nabla\hat{\rho} \\ & - \left(L^{\gamma+\delta+z+1}\alpha\rho - L^{2\gamma+z+\delta+1}\beta\rho^2 \right)\hat{\rho} - L^{\gamma+z+2\delta-1} D(\nabla\hat{\rho})^2\rho \\ & - \left(L^{\gamma+z+1+2\delta}\alpha\rho + L^{2\gamma+z+1+2\delta}\beta\rho^2 \right)\hat{\rho}^2 \Big\}. \end{aligned} \tag{A.23}$$

We seek a scale-invariant action, i.e. under the transformation $L \to \zeta L$, the action S scales as $S \to L^\eta S$. We therefore choose $\gamma = 0$, $\delta = -1$ and $z = 2$:

$$\begin{aligned} S = \int \mathrm{d}t\mathrm{d}x \Big\{ & \hat{\rho}\dot{\rho} - D\nabla\rho\nabla\hat{\rho} - \left(L^2\alpha\rho - L^2\beta\rho^2\right)\hat{\rho} \\ & - \left(L\alpha\rho + L\beta\rho^2\right)\hat{\rho}^2 - \frac{1}{L}(\nabla\hat{\rho})^2 \Big\}. \end{aligned} \tag{A.24}$$

We cross out the last term (as we seek the large L behaviour), and integrate the diffusion term by parts:

$$\begin{aligned} S = \int \mathrm{d}t\mathrm{d}x \Big\{ & \hat{\rho}\dot{\rho} + D\hat{\rho}\Delta\rho - \left(L^2\alpha\rho - L^2\beta\rho^2\right)\hat{\rho} \\ & - \left(L\alpha\rho + L\beta\rho^2\right)\hat{\rho}^2 \Big\}, \end{aligned} \tag{A.25}$$

and this action corresponds to the following Langevin equation:

$$\dot{\rho} = D\Delta\rho + L^2\alpha\rho - L^2\beta\rho^2 + \sqrt{2\alpha L\rho + 2\beta L\rho^2}\eta. \tag{A.26}$$

For small ρ, the $\sqrt{2\beta L\rho^2}$ term is irrelevant while $-\beta L^2\rho^2$ in the deterministic part is important because it damps the linear instability of $\rho = 0$ due to the growth term ($\alpha L^2\rho$). Presumably, the term we remove can be shown to be unimportant by doing a dynamical Renormalisation Group (RG) analysis [Tauber 05]. Finally, we obtain:

$$S = \int \mathrm{d}t\mathrm{d}x \left[\hat{\rho}\dot{\rho} - D\hat{\rho}\Delta\rho - \alpha L^2\rho\hat{\rho} + \beta L^2\hat{\rho}\rho^2 - \hat{\rho}^2\alpha L\rho\right] \tag{A.27}$$

which is exactly the action Eq. (A.10) corresponding the Langevin equation, derived in the previous section, if we make the following identifications for the parameters:

$$\{D, \alpha L^2, \beta L^2, \alpha L\}_{\text{microscopic}} \leftrightarrow \{D, \alpha, \beta, \Gamma\}_{\text{ hydrodynamic}} \tag{A.28}$$

which also describes how the different terms will behave under rescaling, for example, diffusion will be slower in a larger system but growth and death will remain the same.

Bibliography

[Andrews 04] S. S. Andrews, D. Bray, *Phys. Biol*, **1**, 137-151 (2004)

[Arecchi 82] F. T. Arecchi, A. Politi, L. Ulivi, *Il Nuovo Cimento*, **71B**, 119 (1982).

[Bailey 86] J. E. Bailey, D. F. Ollis, *Biochemical Engineering Fundamentals*, 2nd edition, McGraw Hill (1986).

[Barrett-Freeman 07] C. Barrett-Freeman, *Master's thesis*, University of Edinburgh (2007)

[Barton 89] N. H. Barton, G. M. Hewitt, *Nature*, **341**, 497 (1989).

[Bazant 05] M. Bazant, Course Notes on *Random Walks and Diffusion*, MIT, http://ocw.mit.edu/courses/mathematics/18-366-random-walks-and-diffusion-fall-2006 (2005)

[Berg 83] H.C. Berg, **Random Walks in Biology**, Princeton University Press (1983).

[Berg 90] H. C. Berg, L. Turner, *Biophys. J.* **58** 919 (1990).

[Berg 03] H. C. Berg, ***E. coli* in Motion**, Springer (2003).

[Berg 01] J. S. Berg, B. C. Powell, R. E. Cheney, *Mol. Biol. Cell* **12**, 780 (2001)

[Berg 02] J. S. Berg, R. E. Cheney, *Nature Cell Biol.* **4** (2002)

[Bray 01] D. Bray, **Cell Movements: From Molecules to Motility**, 2nd Edition, Garland Publishing New York (2001)

[Bremer 96] H. Bremer, P. P. Dennis, **Modulation of chemical composition and other parameters of the cell by growth rate**. In *Escherichia coli and Salmonella typhimurium: Cellular and Molecular Biology*, 2nd Edition, F. C. Neidhardt, R. Curtiss, E. C. C. Lin, K. Brooks Low, B. Magasanik, W. S. Reznikoff, M. Riley, M. Schaechter, and H. E. Umbarger, editors. ASM Press, Washington, DC. 15531569

[Broadbent 57] S. R. Broadbent, J. M. Hammersley, *Proc. Camb. Phil. Soc.* **53**, 629 (1957)

[Burroughs 06] N. J. Burroughs, D. Marenduzzo, *J. Phys: Cond. Mat.* **18**, 357-374 (2006)

[Carlsson 01] A. E. Carlsson *Biophys. J.* **81**, 1907-1923 (2001)

[Dahmen 00] K. A. Dahmen, D. R. Nelson, N. M. Shnerb, *J. Math. Biol.* **41**, 1 (2000).

[Daniels 04] D. R. Daniels, M. S. Turner, *J. Chem. Phys.* **121**, 7401 (2004)

[Daniels 06] D. R. Daniels, D. Marenduzzo, M. S. Turner *Phys. Rev. Lett.* **97**, 098101 (2006)

[Daniels 10] D. R. Daniels *Biophys. j.* **98**, 1139 (2010)

[Derrida 92] B. Derrida, E. Domany, D. Mukamel, *J. Stat. Phys.* **69**, 667 (1992)

[Derrida 93] B. Derrida, M. Evans, V. Hakim, V. Pasquier, *J. Phys. A: Math. Gen.* **26**, 1493 (1993)

[Derrida 97] B. Derrida, K. Mallick, *J. Phys. A* **30**, 1031 (1997)

[Derrida 07] B. Derrida, D. Simon, *Europhys. Lett*, **78** 60006 (2007)

[Derrida 07b] B. Derrida, *J. Stat. Mech* P07023 (2007)

[Dickman 94] R. Dickman, *Phys. Rev. E*, **50**, 6, (1994)

[Dornic 05] I Dornic, H Chate, M A Munoz, *Phys. Rev. Lett.* **94**, 100601 (2005).

[Edwards 82] S. F. Edwards, D. R. Wilkinson, *Proc. R. Soc. A* **381**, 17 (1982)

[Ellis 01] R. J. Ellis, *Trends Biochem. Sci.* **26**, 597 (2001)

[Enculescu 11] M. Enculescu, H. Stark *Phys. Rev. Lett* **107**, 058301 (2011)

[Evans 00] M. R. Evans, *Braz. J. Phys.* **30**, 42 (2000)

[Feller 51] W. Feller, *Ann. Math*, **54**, 173 (1951)

[Frojdh 01] P. Frojdh, M. Howard, K. B. Lauritsen, *Int. J. Mod. Phys. B* **15**, 1761 (2001)

[Gardel 08] M. L. Gardel, B. Sabass, L. Ji, G. Danuser, U. S. Schwarz , C. M. Waterman *J. Cell. Biol.* **6**, 999 (2008)

[Gardiner 83] C. W. Gardiner, **Handbook of Stochastic Methods**, Springer-Verlag (1983)

[Grassberger 82] P. Grassberger, *Z. Phys.* **B 47**, 365 (1982)

[Grassberger 00] P. Grassberger, W. Nadler, *arXiv:cond-mat*/0010265 (2000)

[Grassberger 02] P. Grassberger, *Comput. Phys. Commun.* **147**, 64 (2002).

[Grinstein 96] G. Grinstein, M. A. Munoz, Y, Tu, *Phys. Rev. Lett.* **76**, 4376 (1996).

[Henkel 08] M. Henkel, H. Hinrichsen, S. Lubeck, **Non-Equilibrium Phase Transitions Volume I: Absorbing Phase Transitions**, Springer, (2008).

[Hinrichsen 00] H. Hinrichsen, *Adv. Phys.* **49**, 815 (2000)

[Janssen 81] H.K. Janssen, *Z. Phys.* **B 42**, 151-154 (1981)

[Jones 02] R. A. L. Jones, **Soft Condensed Matter**, Oxford University Press (2002)

[Kardar 86] M. Kardar, G. Parisi, Y. Zhang, *Phys. Rev. Lett.* **56**, 889 (1986)

[Keller 71] E. F. Keller, L. A. Segel, *J. Theor. biol.* **30**, 225 (1971)

[Klaus 97] D. Klaus et al., *Microbiol.* **143** 449 (1997).

[Lan 08] Y. Lan, G. A. Papoian, *Biophys. J.* **94**, 3839 (2008)

[Lin 95] C. Lin, P. Forscher, *Neuron* **14**, 763-771 (1995)

[Lu 00] C. Y. D. Lu, P. D. Olmsted, R. C. Ball *Phys. Rev. Lett.* **84**, 642 (2000)

[Lubeck 05] S. Lubeck *arXiv:cond-mat*/0501259 (2005)

[McGrath 98] J. L. McGrath, Y. Tardy, C.F. Dewey, J. J. Meister, J. H. Hartwig *Biophys J.* **75**, 2070 (1998)

[Mogilner 05] A. Mogilner, B. Rubinstein, *Biophys. J.* **89**, 782 (2005)

[Mukamel 00] D. Mukamel in **Soft and Fragile Matter**, IOP Publishing Bristol (2000)

[Munoz 98] M. A. Munoz *Phys. Rev. E* **57**, 1377, (1998)

[Munoz 03] M. A. Munoz *arXiv:cond-mat*/0303650 (2003)

[Murray 02] J. D. Murray, **Mathematical Biology 1: An Introduction**, Springer, (2002).

[Nagy 08] S. Nagy, B. L. Ricca, M. F. Norstrom, D. S. Courson, C. M. Brawley, P. A. Smithback, R. S. Rock, *Proc. Nat. Acad. Sci. USA G* **105**, 9616 (2008)

[Oksendal 98] B. Oksendal, **Stochastic Differential Equations**, Springer Berlin, (1998)

[Palacci 10] J. Palacci, C. Cottin-Bizonne, C. Ybert, and L. Bocquet, *Phys Rev. lett.* **105**, 088304 (2010)

[Pearl 20] R. Pearl, L.J. Reed, *Proc. Nat. Acad. Sci. USA G* 275 (1920)

[Pelissetto 02] A. Pelissetto, E. Vicari *Phys. Rept.* **368**, 549 (2002)

[Peskin 93] C. S. Peskin, G. M. Odell, G. F. Oster, *Biophys. J.* **65**, 316 (1993)

[Pollard 03] T. D. Pollard, G. G. Borisy, *Cell*, **112**, 453-465 (2003)

[Pollard 86] T. D. Pollard, *J. Cell Biol.*, **103**, 2747 (1986)

[Press 92] W. H. Press, S. A. Teukolsky, W.T. Vetterling, B.P. Flannery, **Numerical Recipes in C: The Art of Scientific Computing, Second Edition**, Cambridge University Press (1992)

[Proeme 11] A. Proeme, R. A. Blythe, M. R. Evans, *J. Phys. A: Math. Theor.* **44**, 035003 (2011)

[Redner 01] S. Redner, **A Guide to First-Passage Processes**, Cambridge University Press, (2001)

[Risken 96] H. Risken, **The Fokker-Planck Equation: Methods of Solution and Applications**, 2nd edition, Springer, (1996)

[Saarloos 03] W. van Saarloos, *Phys. Rep.* **386**, 29 (2003)

[Sanz 10] E. Sanz, D. Marenduzzo, *J. Chem. Phys.* **132**, 194102 (2010)

[Schafer 04] D. A. Schafer *Nature* **430**, 734 (2004)

[Schutz 93] G. Schutz, E. Domany *J. Stat. Phys.* **72**, 277 (1993)

[Sheetz 92] M. P. Sheetz, D. B. Wayne, A. L. Pearlman *Cell Motil. Cytoskeleton* **22**, 160-169 (1992)

[Speirs 01] D. C. Speirs, W. S. C. Gurney, *Ecology*, **82(5)**, 1219 (2001)

[Svitkina 03] T. M. Svitkina, O. Y. Chaga, D. M. Vignjevic, S. Kojima, J. M. Vasiliev, G. G. Borisy, *J. Cell Biol.* **160**, 409 (2003)

[Tailleur 08] J. Tailleur, J. Kurchan, V. Lecomte, *J. Phys. A: Math. Theor.* **41**, 505001 (2008)

[Takeuchi 07] K. A. Takeuchi, M. Kuroda, H. Chate, M. Sano *Phys. Rev. Lett.* **99**, 234503 (2007)

[Takeuchi 09] , K. A. Takeuchi, M. Karuda, H. Chate, M. Sano, *Phys. Rev E* **80**, 051116 (2009)

[Tauber 05] U. C. Tauber, M. Howard, B. P. Vollmayr-Lee, *arXiv:cond-mat*/0501678 (2005)

[Thompson 11] A. G. Thompson, J. Tailleur, M. E. Cates, R. A. Blythe, *J. Stat. Mech.*, P02029 (2011)

[Tu 97] Y. Tu, G. Grinstein, M. A. Munoz, *Phys. Rev. Lett.* **78**, 274 (1997).

[Verhulst 1838] P.F. Verhulst, *Curr. Math. Phys.* **10**, 113 (1838)

[Wang 96] Wang F. S., J. S. Wolenski, R. E. Cheney, M. S. Mooseker, D. G. Jay, *Science* **273**, 660-663 (1996)

[Weisstein a] Weisstein, E. W. "Modified Bessel Function of the First Kind." From MathWorld–A Wolfram Web Resource. http://mathworld.wolfram.com/ModifiedBesselFunctionoftheFirstKind.html

[Weisstein b] Weisstein, E. W. "Buckingham's Pi Theorem." From Scienceworld–A Wolfram Web Resource. http://scienceworld.wolfram.com/physics/BuckinghamsPiTheorem.html

[Weisstein c] Weisstein, Eric W. "Baker-Campbell-Hausdorff Series." From MathWorld–A Wolfram Web Resource. http://mathworld.wolfram.com/Baker-Campbell-HausdorffSeries.html

[Zhuravlev 10] P. I. Zhuravlev, B. S. Der, G. A. Papoian, *Biophys. J.* **98**, 1439-1448 (2010)

List of Publications

[1] C. Barrett-Freeman, M. R. Evans, D. Marenduzzo, W. C. K. Poon, *Phys. Rev. Lett* **101**, 100602 (2008)

[2] C. Barrett-Freeman, M. R. Evans, D. Marenduzzo, J. Tailleur *Europhys. Lett.* **90**, 16003 (2010)